Thesis for the degree
Doctor of Philosophy

Submitted to the Scientific Council of the
Weizmann Institute of Science
Rehovot, Israel

עבודת גמר (תזה) לתואר
דוקטור לפילוסופיה

מוגשת למועצה המדעית של
מכון ויצמן למדע
רחובות, ישראל

By
Iakov Aizenberg

מאת
יעקב אייזנברג

חיפוש חתימות פיזיקליות בהתנגשויות של יונים כבדים במערכות קלות בעזרת גלאי ATLAS בLHC

Search for the Heavy Ion Physics Signatures in Small Collision Systems with the ATLAS Detector at the LHC

Advisor:
Prof. Alexander Milov

מנחה:
פרופ אלכסנדר מילוב

December 2022

דצמבר 2022

Acknowledgments

I acknowledge the essential help from my advisor Prof. Alexander Milov during all the years of my graduate program. I am grateful for all the transferred knowledge and many opportunities to be a part of the scientific work at the front of what is currently studied by the heavy-ion physics community. I acknowledge all the work and help from Prof. Zvi Citron (Ben-Gurion University of the Negev, Israel), who worked with me from my early years at the Weizmann Institute. I am very grateful to all of my other colleagues in the WIS HI group - Dr. Mirta Dumančić (McGill University, Canada) and Dr. Evgeny Shulga (Stony Brook University, NY, United States). I thank Dr. Pierre Choukroun for his help and availability in solving computing problems. I want to thank Prof. Oleg Zenin (Institute of High Energy Physics, Russian Federation), Prof. Deepak Kar (University of Witwatersrand, South Africa), and Prof. Vakhtang Kartvelishvili (Lancaster University, United Kingdom) for their patience, interest, and mentorship as members of the ATLAS editorial board for the analysis which is a core of this thesis. I want to thank Revital Ackler, Hemda Atsits, Natalia Leibovich, Hila Shtudiner, Merav Basson, and Amir Bar On from the administrative staff of the Department of Particle Physics & Astrophysics for their help. I thank my family and friends who supported me during my years here at the Weizmann Institute. Especially, I'm thankful to my "second" family - Natasha, Igor, Sofia, and Anton. Once again, thank you all for the fruitful and hard years of work and research that brought forth this final result.

Declaration

I hereby declare that except where specific reference is made to the work of others, the contents of this thesis are original and have not been submitted in whole or in part for consideration for any other degree or qualification in this or any other university. This thesis is my work and contains nothing which is the outcome of work done in collaboration with others except as specified in the text and Acknowledgements.

Iakov Aizenberg

Contents

Acronyms

2PC Two-particle correlations. 18–20, 96

ALICE A Large Ion Collider Experiment. 27, 82, 96

ATLAS A Toroidal LHC Apparatus. 8, 11, 26–28, 34–38, 40, 44, 45, 47, 51, 59, 79, 82, 94

CERN The European Organization for Nuclear Research. 8, 13, 27, 28

CIM Comover Interaction Model. 95, 96

CMS Compact Muon Solenoid. 27, 34, 82, 94, 95

CSC Cathode-Strip Chamber. 37

EM Electromagnetic. 29–31, 33

EW Electroweak Theory. 12

FCal Forward Calorimeters. 30, 31

GRL Good Run List. 37

HEC Hadronic End-cap Calorimeter. 30

HF Heavy-flavor. 9

HI Heavy Ions. 8, 15–18, 27

HLT High-level trigger. 33, 37, 38

ID Inner-detector system. 37, 38, 72

LAr Liquid-argon. 29, 30

LHC Large Hadron Collider. 6, 8–11, 14, 17–20, 23, 27, 35, 43, 45, 52, 82, 87, 88, 90, 94

LHCb A Large Hadron Collider beauty. 27, 82, 94

MC Monte-Carlo. 36, 68, 72, 76, 90

MDT Monitored Drift Tube. 37

MS Muon spectrometer. 31–33, 37

NBD Negative Binomial Distribution. 52, 53, 73

NRQCD Non-Relativistic QCD. 94

pQCD Perturbative quantum chromodynamics. 13, 93

PU Pileup. 10, 34, 35, 38–40, 42–47, 52, 53, 55, 58, 60, 67–75, 79

QCD Quantum Chromodynamics. 7, 9, 13–15, 23–25, 94

QED Quantum Electrodynamics. 12

QGP Quark-Gluon Plasma. 8–10, 14, 17–22

RHIC Relativistic Heavy Ion Collider. 11, 18

SM Standard Model. 12, 13, 27

SPS The Super Proton Synchrotron. 11

TileCal Tile Hadronic Calorimeter. 29, 31

TnP Tag-and-Probe. 48, 49

UE Underlying Event. 9, 10, 22, 34, 35, 60, 76, 78, 79, 81, 90–93

ZDC Zero-Degree Calorimeters. 31

Abstract

The Quark-Gluon Plasma is the state of matter in which the quarks and gluons are not bound into hadrons. This form of matter is observed in large systems of particles that can be produced in collisions of relativistic Heavy Ions, for example, at the LHC at CERN. Recent measurements reveal the effects which are considered the signatures of the QGP also in much smaller proton-proton collisions, where they have no clear explanation. The thesis includes two independent analyses that may shed light on this novel phenomenon.

The analysis of the multiplicity and kinematic distributions of charged particles produced in association with an Υ meson measured in proton-proton collisions uses the data collected by the ATLAS experiment at the LHC. The analysis uses a full Run 2 data set obtained at $\sqrt{s} = 13$ TeV, corresponding to the integrated luminosity of 139 fb^{-1}. At zero Υ transverse momentum, the associated charged-particle multiplicity drastically differs for different Υ states. It is by $17\pm4\%$ fewer for $\Upsilon\,(3S)$ and by $12\pm1\%$ fewer for $\Upsilon\,(2S)$ than for $\Upsilon\,(1S)$. These differences are associated with the underlying event of collisions and decrease with increasing transverse momentum of the Υ states. This measurement is a direct suggestion of bottomonia suppression in pp collisions at the LHC.

A global study of the momentum distributions of the mesons at LHC energies uses an empirical transverse mass scaling approach. This study demonstrates patterns in the spectral properties of mesons related to their quark content and is instrumental in working out the differences in the spectral shapes of particles with identical quark content and close masses. Based on the transverse mass scaling assumption, the excited bottomonia states are found to be suppressed with respect to the ground state by a factor of 1.6 and 2.4 for $\Upsilon\,(3S)$ and $\Upsilon\,(2S)$ respectively. The two measurements must be related to the same physics mechanism and have to be understood together.

1 Introduction

Correlations between processes characterized by different momentum scales and correlations between "hard" and "soft" particle production are interesting but relatively unexplored aspects of high-energy collisions. This topic lies at the intersection of several research directions pursued in the high-energy and heavy-ion research programs at the LHC. The underlying event (UE) is an important feature of proton-proton (pp) collisions and is essential to determine the role that multiparton interactions play in the formation of the final state. Color fields connect all the strongly interacting partons, and so an unambiguous assignment of particles to the hard scattering partons or UE is not possible. Despite this ambiguity, observables such as the multiplicity, transverse momentum, and angular distributions of charged particles are sensitive to the UE [1–3]. In the context of heavy-ion physics, the UE may reflect the conditions for Quark-Gluon Plasma (QGP) formation and may also be used as a metric of event activity.

Heavy-flavor (HF) production in high-energy collisions is a sensitive test of our understanding of Quantum Chromodynamics (QCD). Several measurements of $\Upsilon(n\mathrm{S})$ mesons in pp collisions at the LHC [4–11] have been performed, and these have spurred the development of refined models based of perturbative QCD (see a recent review in [12] and references therein). In addition, the Υ meson is a probe expected to undergo energy loss in the hot dense medium formed in A+A collisions. Based on lattice-QCD calculations, it is expected that in a QGP medium, heavy quarkonium states will be "sequentially suppressed" as the deconfined color charges within the QGP will screen the heavy quark-antiquark ($q\bar{q}$) pair. See a review in Ref. [13] and references therein. Analyzing the correlation between the UE and HF meson formation can provide information about the density and screening of color charges in the produced matter as a function of the size of the produced system.

Recently the CMS collaboration measured the event activity dependence of the relative production of $\Upsilon(n\mathrm{S})$ states in pp collisions [14, 15]. Event activity was represented by charged-particle multiplicity. In these studies, it was observed that the ratios of $\Upsilon(2\mathrm{S})$ to $\Upsilon(1\mathrm{S})$ and $\Upsilon(3\mathrm{S})$ to $\Upsilon(1\mathrm{S})$ production cross-sections decrease as a function of the charged particle multiplicity, i.e., more charged particles are present in events with an observed $\Upsilon(1\mathrm{S})$ than in events with observed $\Upsilon(2\mathrm{S})$ or $\Upsilon(3\mathrm{S})$. Furthermore, the relative $\Upsilon(n\mathrm{S})$

production in different event topologies, as quantified by the transverse sphericity dependence, suggested that the differences between $\Upsilon(n\mathrm{S})$ states are not simply a function of their mass differences and are not due to effects of jets that balance the $\Upsilon(n\mathrm{S})$ momentum. Reference [15] hypothesized that this might be consistent with a suppression of the excited Υ states at high charged-particle multiplicity.

The goal of my Ph.D. is to understand the physics nature of the modification of the $\Upsilon(n\mathrm{S})$ production yields observed in *pp* collisions and its possible relation to the formation of the QGP in small systems. The $\Upsilon(n\mathrm{S})$ mesons are excellent candidates for such studies due to their high sensitivity to the presence of the medium in A+A collisions [16] where it resides. The presence of the three states of the $b\bar{b}$ quarkonium with close masses and different binding energies allows conclusive relative comparison of the effects for which the $b\bar{b}$ states can be used as a set analog, yet different probes, that are crucial for *pp* collisions in which comparison to other (smaller) systems isn't feasible. In this study, the UE is inferred through the number of charged particles (n_{ch}) which are differentiated into those that are directly involved in the formation of the Υ state produced and the particles that belong to the UE of the collision. i.e., are produced in different multiparton scatterings.

This work studies the UE in *pp* collisions where $\Upsilon(n\mathrm{S})$ states are present, using the full statistics of LHC Run-2 at $\sqrt{s} = 13$ TeV. This approach differs from the CMS [15] that measured $\Upsilon(n\mathrm{S})$ rates as a function of the UE multiplicity in several ways. First of all, measuring charged-particle distributions in collisions with different $\Upsilon(n\mathrm{S})$ states rather than the $\Upsilon(n\mathrm{S})$ rates as a function of multiplicity allowed better signal extraction and, as a result, smaller systematic uncertainties. This became possible due to the Pileup (PU) subtraction method used in this work. Furthermore, it allows handling data collected at much higher instantaneous luminosities, which in turn opens the possibility of using much larger $\sqrt{s} = 13$ TeV data. To isolate the effects possibly related to the new physics, one needs to understand the effects coming from the difference in jet containing the meson or from the feed-down of upper Υ states into lower states which is assessed using Pythia8 Monte-Carlo physics generator [17].

If the suppression of excited Υ states is indeed the mechanism that is present in *pp* collisions, it should be possible to directly measure it in some other unrelated analysis. The presence of the three Υ states with identical quark content and very close masses allows doing it based on the first-principle physics assumptions. Particles with identical

quark content and identical masses shall possess the same kinematic distributions. An effect caused by a small, less than 10% difference in masses between the states can be estimated, implying a so-called transverse mass scaling (m_{T}-scaling). The scaling is not based on any solid physics principles, nevertheless, it has been observed to work with remarkable precision in many collision systems and in a broad range of incident energies from the SPS to RHIC, and LHC [18–20]. The observed scaling is different for baryons and mesons, and this part of the project presents a comprehensive study of the m_{T} scaling of mesons at LHC energies with a focus on heavier mesons. The analysis uses published results from pp collisions obtained at $\sqrt{s} = 7$, 8, and 13 TeV by ALICE, ATLAS, CMS, and LHCb experiments. Global analysis of meson spectra allows us to obtain expectations for momentum distributions of the excited Υ states that are found to be drastically different from those that have been measured in the experiment. This is the only known example of such spectacular 'failure' of the m_{T} scaling, which cannot be explained by known other effects, for example, by the feed-downs coming from heavier particle decays, that have also been studied.

The thesis is organized as follows. Chapter 2 introduces the theoretical background for the research project and presents an overview of the current results on observations of 'heavy-ion' effects in small collision systems. Chapter 3 discusses experimental characteristics of the ATLAS detector at the LHC. Chapters 4 and 5 present a detailed measurement procedure for extracting final results. Finally, Chapter 6 discusses the results of this work in the context of the current status of the field and possible underlying physics that emerges from these measurements.

2 Theoretical background and current results

2.1 The Standard Model of particle physics

The Standard Model (SM) [21, 22] is a theory based on the gauge symmetry group. It describes the properties of fermions and their strong and electroweak interactions. These interactions are mediated by bosons. The strong force is carried by the massless gluon (g), the weak force is mediated by the massive vector gauge bosons ($W^{\pm}$,Z), and the electromagnetic force is mediated by the photon (γ). The SM does not describe the gravitational interaction.

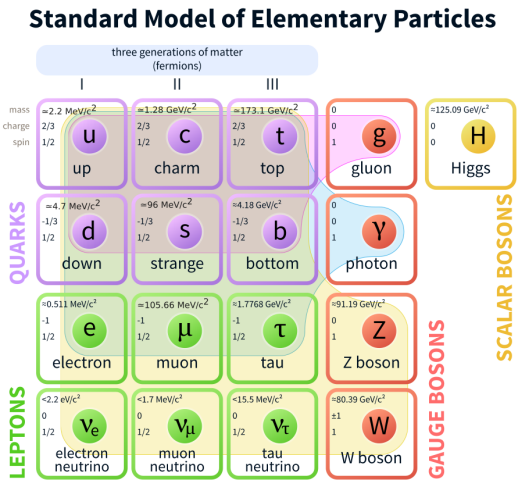

Figure 1: Elementary particles of Standard Model [23].

The SM is composed of three generations of matter called fermions. Fermions can be classified into quarks and leptons (see Figure 1). Leptons carry either only electric charge (± 1 or 0), and quarks carry both color charge and fraction of the electric charge. The fermions are classified into three generations of particles, where each particle has a corresponding anti-particle. There are six flavors of quarks and anti-quarks.

The interaction between particles is described by electromagnetic, weak, and strong interactions. The electromagnetic force governs the interaction among two elementary particles with an electric charge. The electromagnetic interaction is effective in an infinite range. The electromagnetic interaction theory is called Quantum Electrodynamics (QED). The weak interaction has a finite range (around 10^{-18} m). The weak interaction is unified with the electromagnetic interaction in the electroweak (EW) theory [22, 24].

Another piece of SM is the Higgs Mechanism. The mechanism that breaks electroweak symmetry [25] implies the existence of a scalar particle - the Higgs boson H. The discovery of Higgs boson at CERN was reported in 2012 [26, 27]. The strong interaction [28, 29] acts between particles carrying color charges. The interaction is mediated by gluons which carry color charge and anti-color charge. Gluons can also interact among themselves. The theory describing the strong interaction is QCD.

All the leptons in SM can be observed in nature as free particles, as they do not experience a strong force. On the other hand, quarks and gluons are not seen as individual particles. This phenomenon is called color confinement. The strong interaction between color-charged particles forces the quarks and gluons to be confined in hadrons. Hadrons are colorless. In addition to the valence quarks determining the quantum number of the hadron, they contain a sea of virtual quarks and gluons, which contribute to the total energy and momentum. There are two kinds of hadrons - mesons and baryons. Mesons are composed of a quark-antiquark pair, and baryons are composed of three valence quarks. Quarks forming particles have different colors and are bound by gluons. In the formalism of the parton model [30], the constituents of hadrons, quarks, and gluons are referred to as partons. The scale of strong interaction is the four-momentum transferred between the partons participating in the hard scattering, Q^2. An interaction involving a large transfer of momentum is called hard, and an interaction involving a small transfer of momentum is called soft. At the leading order, the strength of the strong coupling is given by the dependence of the strong coupling constant α_s on Q^2 [31] that can be written as

$$\alpha_s(Q^2) = \frac{4\pi}{\left(11 - \frac{2}{3}n_f\right) \ln \frac{Q^2}{\Lambda^2_{QCD}}} \tag{1}$$

where n_f is the number of quark flavors and $\Lambda_{QCD} \approx 200$ MeV is a constant which corresponds to the limit where the perturbative QCD (pQCD) calculations are not applicable anymore.

The strong coupling constant $\alpha_s(Q^2)$ gets asymptotically reduced as Q is increased. pQCD can then be fully applied to the asymptotic free regime since the strong coupling constant is small. This phenomenon is known as asymptotic freedom [32, 33]. As seen in Figure 2, the intensity of the strong force increases when the energy scale is reduced or the distance is increased. At low Q^2, the coupling constant becomes large, such that soft processes cannot be calculated using a perturbative expansion. The large distance behavior of the coupling constant leads to the confinement properties of the strong interaction.

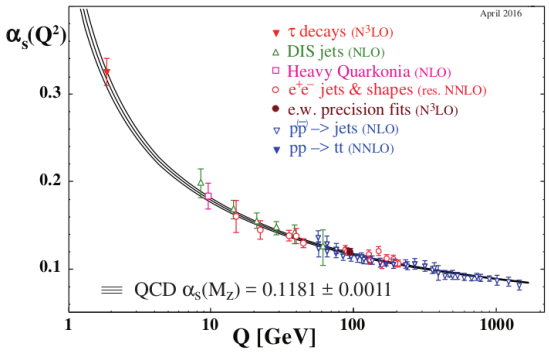

Figure 2: Summary of measurements of α_s as a function of the energy scale Q [23].

2.2 Quark-gluon plasma

At high enough temperatures, exceeding the Hagedorn temperature [34], it is anticipated that the energy density in the system is high enough that the hadronic matter undergoes a phase transition to a state where the constituents are not hadrons but quarks and gluons. Asymptotic freedom implies that the constituents of the matter effectively experience a weak interaction, and form a liquid of color charges, historically called the QGP [35].

The phase transition is illustrated in the QCD phase diagram shown in Figure 3, where different phases of nuclear matter are illustrated as a function of the baryon chemical potential μ_B (essentially the difference in the number of quarks and antiquarks) and the system temperature. The phase transition can be triggered by either compressing the hadronic matter to a large density or heating it to a high temperature. A first-order transition from partonic matter to hadronic matter is expected at the critical end point [37]. The temperature at the critical point is known as critical temperature T_c. At LHC energies, the energy is sufficiently high so that the produced amount of particles overrides the initial excess in baryon number coming from the colliding nuclei. Therefore, a balanced amount of produced quark and antiquark pairs yields essentially $\mu_B \approx 0$, while the produced system has high energy density and temperature, around 300 MeV [38]. This is almost twice the T_c predicted by lattice QCD calculations [39] and previously motivated by simple fermion gas models [40].

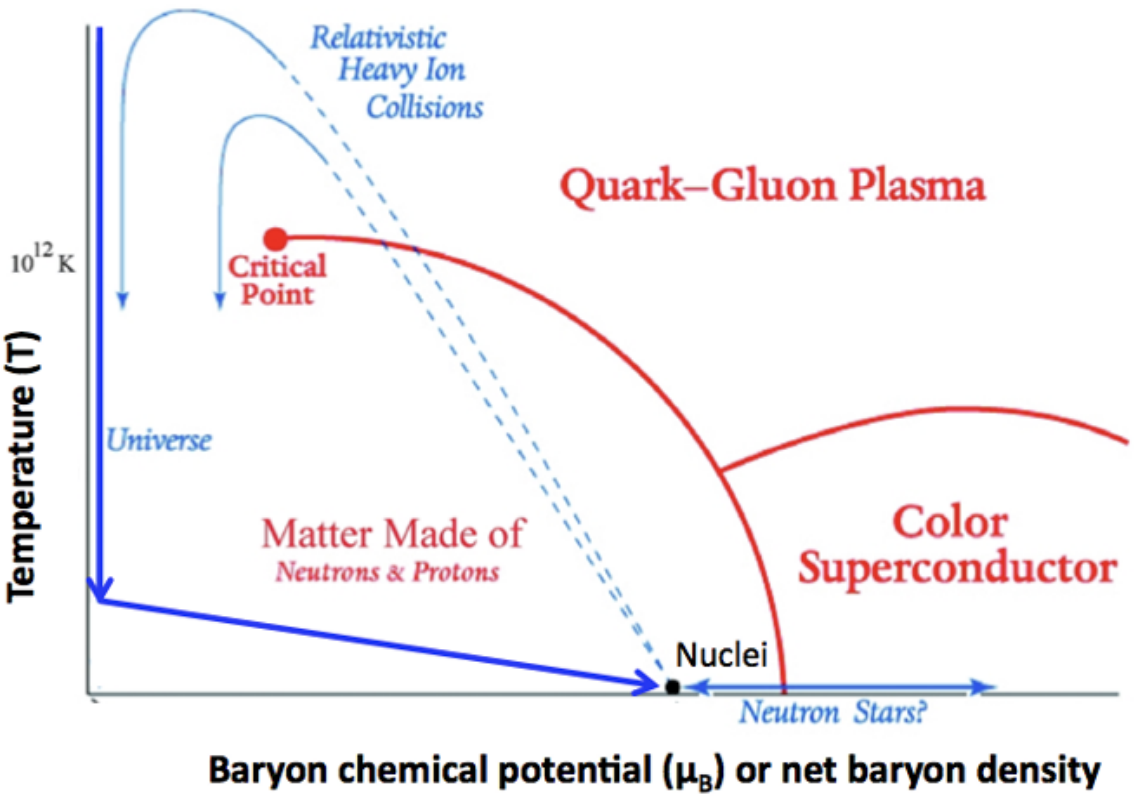

Figure 3: The phase diagram of nuclear matter as a function of the baryon chemical potential and temperature of the system [36].

2.3 Heavy ion collisions

Collisions of Heavy Ions (HI) at high energies is a tool to create a QCD matter at extreme values of energy densities which gives an excellent opportunity to study and test our knowledge about the theory of strong interaction.

Since nuclei are objects of finite size and area, the collision can have different geometries. A schematic view of a typical collision of two nuclei is shown in Figure 4. The geometry of the HI collision largely defines the outcome of the interaction. The axes of the two nuclei are separated by a distance b called the impact parameter. The collision is central when the impact parameter is small. In this case, the interaction area is large, and the number of participating nucleons is high. The collision is called peripheral if the nuclei are colliding with a large impact parameter or ultra-peripheral when nuclei are just grazing each other. The impact parameter of the interaction is not a measurable quantity in any real experiment. To categorize HI interaction by initial geometry, an empirical quantity called "centrality" is widely used in HI experiments. Centrality is expressed

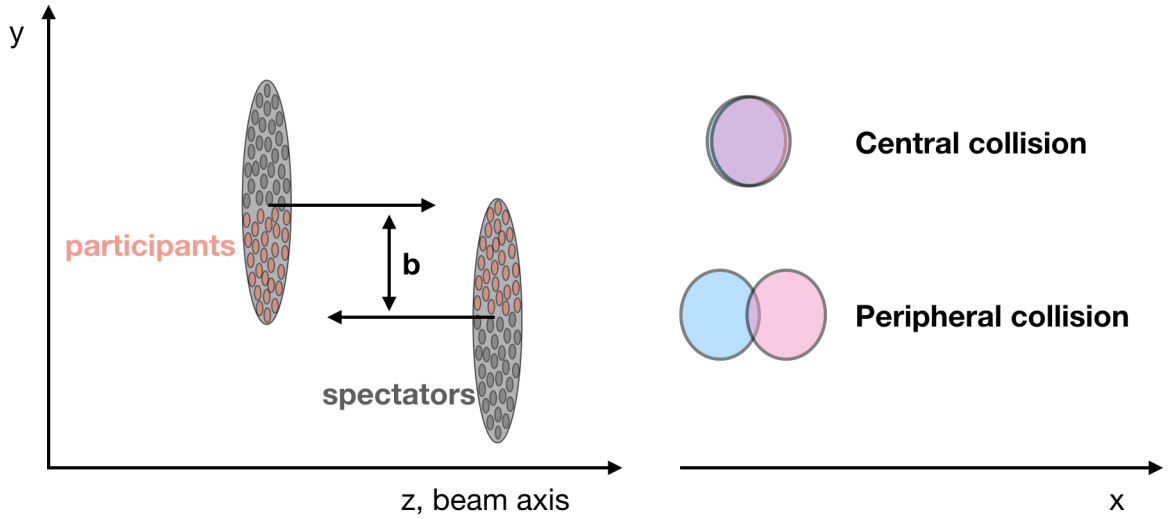

Figure 4: Schematic view of HI collision.

in percentiles, where low values indicate more central collisions and the most peripheral percentiles close to 100%.

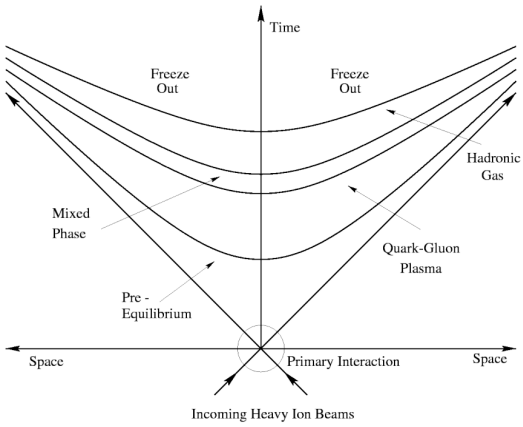

Figure 5: The space-time evolution of a HI collision [41].

Figure 5 illustrates the evolution of the matter created in HI collisions. A thermalized system of quarks and gluons is formed over a period of time comparable to the duration of the ion-ion interaction, i.e., a fraction of a fm/c. The matter remains in this state for approximately 5-10 fm/c, and then, as it expands and cools down, the system passes through several different stages. First, it hadronizes, and the mesons and baryons formed in that process actively interact with each other. With further expansion, hadrons cease interacting inelastically, leading to the "chemical freeze-out" of the system. At later stages, elastic scattering also ceases, at which time the kinetic properties of the system

are formed. This is called the "kinetic freeze-out".

The QGP cannot be measured directly since it exists only for a very short time. It can be studied indirectly by measuring how the properties of particles and the system produced in the collision are modified by the presence of the QGP. The production mechanism of each experimental probe depends on the momentum scale of the process. The hard probes are the signatures produced in the process involving large momentum transfer and are created in the initial stages of the collisions. Most of the particles produced in HI collisions are soft and constitute the bulk of the system. Soft probes are used to study the thermal and hydrodynamical evolution of the medium.

An empirical quantity widely used in HI studies is the Nuclear Modification Factor which is a ratio of the yield in the system of study to the yield measured in pp at the same energy:

$$R_{\mathrm{AB}}\left(y, p_{\mathrm{T}}\right) = \frac{1}{\langle T_{\mathrm{AB}} \rangle} \frac{\left(1/N_{\mathrm{evt}}\right) \mathrm{d}^2 N_{\mathrm{AB}}/\mathrm{d}y\mathrm{d}p_{\mathrm{T}}}{\mathrm{d}^2\sigma_{pp}/\mathrm{d}y\mathrm{d}p_{\mathrm{T}}} \tag{2}$$

where $\left(1/N_{\mathrm{evt}}\right) \mathrm{d}^2 N_{\mathrm{AB}}/\mathrm{d}y\mathrm{d}p_{\mathrm{T}}$ is a per-event yield of an observable in the collisions measured differentially in p_{T} and rapidity y; $\mathrm{d}^2\sigma_{pp}/\mathrm{d}y\mathrm{d}p_{\mathrm{T}}$ is the cross-section measured in pp collision, and T_{AB} is the geometric quantity called the nuclear thickness function that accounts for that fact that the per nucleon luminosity in the A+B collision system is larger than in pp. T_{AB} can be calculated from the nuclei shapes given by the Woods-Saxon distribution [42]. The R_{AB} consistent with unity means that a HI collision can be interpreted as a direct superposition of pp collisions implying no nuclear effects. This behavior is expected in collisions with the large impact parameter, which are pp-like. As the impact parameter becomes smaller other effects may show up that are reflected in the R_{AB}.

2.4 Hints of HI physics in small systems

Small collision systems play an essential role in HI studies. Measurements done in pp are the baseline for understanding larger collision systems, and $p + \mathrm{A}$ collisions are typically considered a control system to understand the so-called "cold nuclear matter effects", i.e., effects that are present in nuclei prior to interaction. Understanding these effects is critical to untangle final state effects, such as modification caused by the formation of a hot medium in A+A interactions from the initial state effects. Extensive studies of pp and $p + \mathrm{Pb}$ collision systems have been performed at the LHC to accomplish these goals.

In turn, the RHIC program included $d + \mathrm{Au}$ and later $p + \mathrm{Au}$ collisions that constituted a significant fraction of the collider operation time.

Accumulated knowledge about large collision systems and techniques developed in their analysis led to a question that gradually became one of the most discussed topics in the field: What are the minimal conditions at which a QGP may be formed? This question is a direct consequence of a series of observations that small systems exhibit the same signatures that are, or at least were previously, attributed to the formation of QGP in large systems.

One of the first experimental observations of 'conventional' HI effects in a small system was done by the CMS experiment, which measured the two-particle correlations (2PC) in high multiplicity pp collisions at $\sqrt{s} = 7$ TeV [43]. In HI collisions, this effect was understood as a result of the hydrodynamic expansion of the QGP, but the phenomenon found in high multiplicity pp collisions was completely unexpected, and it is still not fully understood. Followed by extensive studies in many experiments, the 2PC are clearly seen in the hadronic collision systems of any size, and recently also in photonuclear collisions as well [44]. Figure 6 shows 2PC measured in three different systems. An elevation at

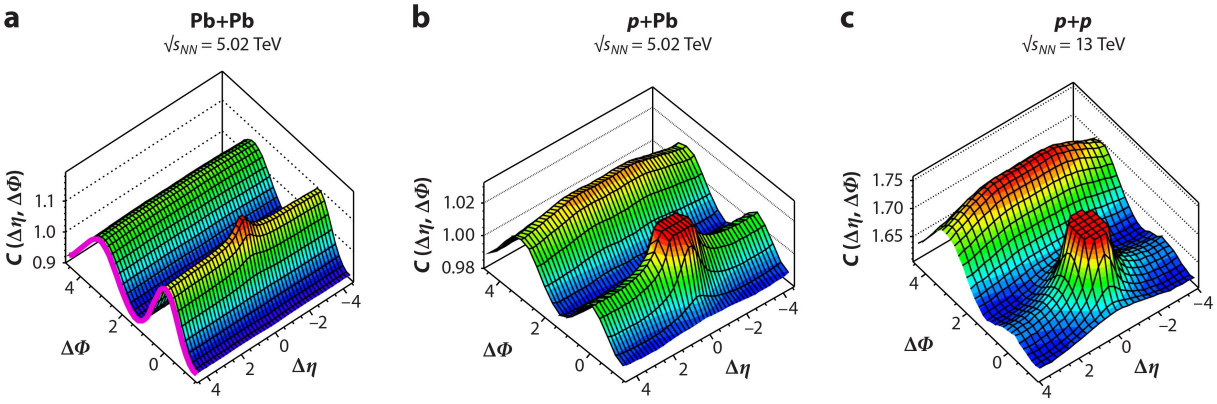

Figure 6: Two-particle correlation results in Pb + Pb, $p + \mathrm{Pb}$, and pp collisions at the LHC. A large $\cos(2\Delta\phi)$ correlation with peaks at $\Delta\phi = 0, \pi$, that extend long-range in pseudorapidity $\Delta\eta$ (magenta curve). A similar feature is observed in $p + \mathrm{Pb}$ and pp collisions. From Ref. [45].

$\Delta\phi = 0$ spans over the entire measured $\Delta\eta$ range is seen in all three systems, demonstrating the correlation between particle directions even for the particles separated by significant rapidity gaps. Further measurements of n-particle cumulants demonstrated that correlations exist between many particles in the event. Refs. [45, 46] and references

therein review these measurements. It was shown that the initial geometry plays an important role in the final magnitude of 2PC in small systems [47] and that the mass ordering observed in A+A systems is also present in small systems (see e.g. Ref [48]), in agreement with a flowing liquid description of the system (hydrodynamical models become more and more instrumental in describing collective effects in small systems [49], even though the applicability of these models is sometimes marginal). Nevertheless, apparent similarities in the description of 2PC in large and small systems are the first in a line of shreds of evidence that the QGP scenario can be considered for small systems.

Another consideration that the QGP can possibly be present in small systems is the measurement of multi-strange particle production by the ALICE experiment [50]. A comprehensive study of particle abundances containing strange quarks is published in Ref. [51]. Figure 7 demonstrates it as ratios of particles contacting strange quarks to particles built out of light quarks only. The strangeness production at the LHC steadily

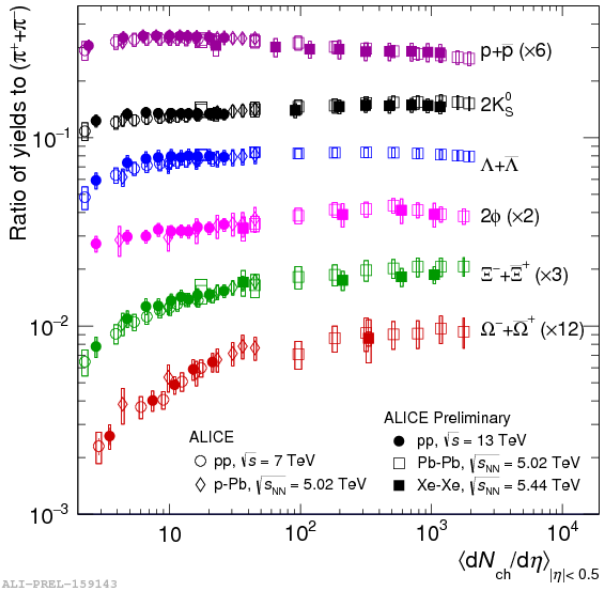

Figure 7: Ratio of integrated yields of particles containing strange quark to pions at mid-rapidity as a function of charged particle multiplicity, reported for several collision systems and energies. Error bars show the statistical uncertainty, boxes show total systematic uncertainty. From Ref. [51], see references therein.

increases as a function of multiplicity. *pp* collisions covering up to approximately 30 tracks is the system where the strangeness contact increases in the most dramatic way. In p+Pb interactions that reach higher multiplicities up to 50 tracks, the strangeness keeps rising before reaching the values observed in A+A collisions. Above a hundred charged particles,

all curves are essentially flat, showing consistency between Pb + Pb and Xe + Xe collision systems. Thus, the most dynamical region falls in the interval covered by *pp* collisions, with about five charged particles per unit of rapidity at these energies, although much higher multiplicities can also be registered in *pp*. The remarkable similarity of strange particle production in *pp*, p + Pb, Xe + Xe, and Pb + Pb is a demonstration that also small collision systems exhibit characteristic features known from high-energy heavy-ion collisions and understood to be connected to the formation of a deconfined QGP phase at high temperature and energy density.

These measurements bring convincing evidence that small and large systems may have more in common than once thought. However, up until recently, there existed no evidence that hard probes are modified in small systems. Measurements of nuclear modification for charged particles [52] or jets [53] reveal no evidence of the onset of the QGP in small systems. A plausible explanation for that might be that the medium created in such collisions is small, so an average path of energetic partons that loses energy in such a system is also short; therefore, the hard scattering processes are only modestly affected by scattering on other partons in the medium. A discussion of the absence of jet quenching in small systems given in Ref. [45] lists theoretical works that successfully reproduce nuclear modification measured in large and small systems. One can still speculate that although the QGP can possibly be formed in small systems and affect partons produced in hard scattering during the final stage of the system evolution, its impact is insufficient to be measured with the current precision of detectors using available data samples. On the other hand, the question about the formation of the QGP in small systems demands some convincing (positive or negative) confirmation from the hard probe sector observables.

Direct measurement of jet quenching in small systems is challenging, and even if observed, the effect may have an alternative explanation [54]. This motivates us to explore hard probe observables that would be more sensitive to droplets of QGP possibly formed in small systems. Among signatures of QGP measured in A+A systems, different observables have different magnitudes. Since 2PC and strangeness enhancement both show significant effects in *pp*, this system seems more interesting than p + Pb, especially because *pp* has orders of magnitude larger statistical samples than p + Pb at the LHC.

Perhaps, the cleanest demonstration of jet quenching in A+A collisions is the modification of the energy balance between the leading jet and a photon that is reduced by

approximately 15–20% in the most central Pb+Pb collision [55], see left panel of Figure 8. Measurements of di-jets lead to approximately the same magnitudes of misbalance [57] in

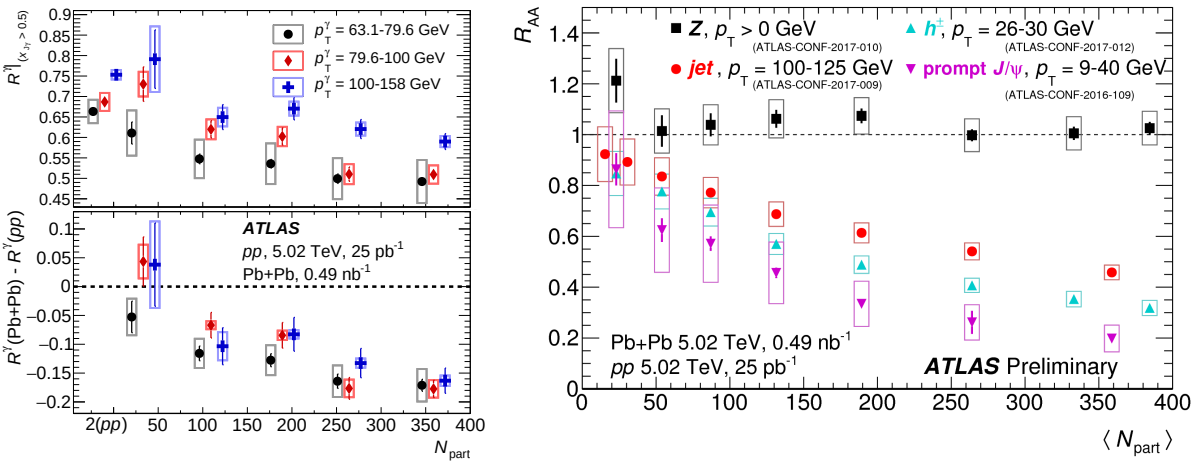

Figure 8: Left: Summary of the total per-photon jet yield R^γ, calculated in the region $x_{J\gamma} > 0.5$, as a function of the mean number of participating nucleons $N_{\rm part}$ in different $p_{\rm T}^\gamma$ intervals. The bottom panel shows the difference between Pb+Pb centrality selection and pp collisions [55]. Right: Compilation of results for the nuclear modification factor $R_{\rm AA}$ vs number of participating nucleons $N_{\rm part}$ in different channels from the Run 2 Pb + Pb and pp data [56].

the most central A+A collisions. These results come with systematic uncertainties equal to 15–30% for the difference between the most central and peripheral collisions. Taking anticipated magnitudes of the effect in pp of an order of 1% based on calculations published in Ref. [54], it is clear that finding any modification of this observable due to QGP in pp data would be very difficult.

The right panel of Figure 8 presents various observables [58] measured in Pb + Pb by the ATLAS experiment that shows the signatures of the QGP formed in the most central collisions. Production of charged hadrons in $26 < p_{\rm T} < 30$ GeV is reduced by a factor of 4. Also, charged hadron modification can be measured with significantly higher accuracy. The high sensitivity of this observable is due to a combined impact of several factors: parton energy loss as discussed above, modification of the jet fragmentation that can also be measured independently, and steepness of the charged particle spectra at a given energy.

Since the present study is focused on small systems, the modification of hard probe observables is also expected to be small. Furthermore, hard probes, where such mea-

surements have not yielded a definitive statement, are rare and require high statistics. Therefore, it is advantageous to explore the most sensitive probes of the QGP, characterized by the widest dynamic range in large systems, although comparing the sensitivity of different observables to the onset of the QGP is not at all straightforward. Nevertheless, the suppression of $\Upsilon(n\mathrm{S})$ can be considered as one of the sensitive observables. Figure 9 shows the nuclear modification of different meson states in Pb+Pb collisions as a function of event centrality, where the level of $\Upsilon(1\mathrm{S})$ suppression reaches the same magnitudes as

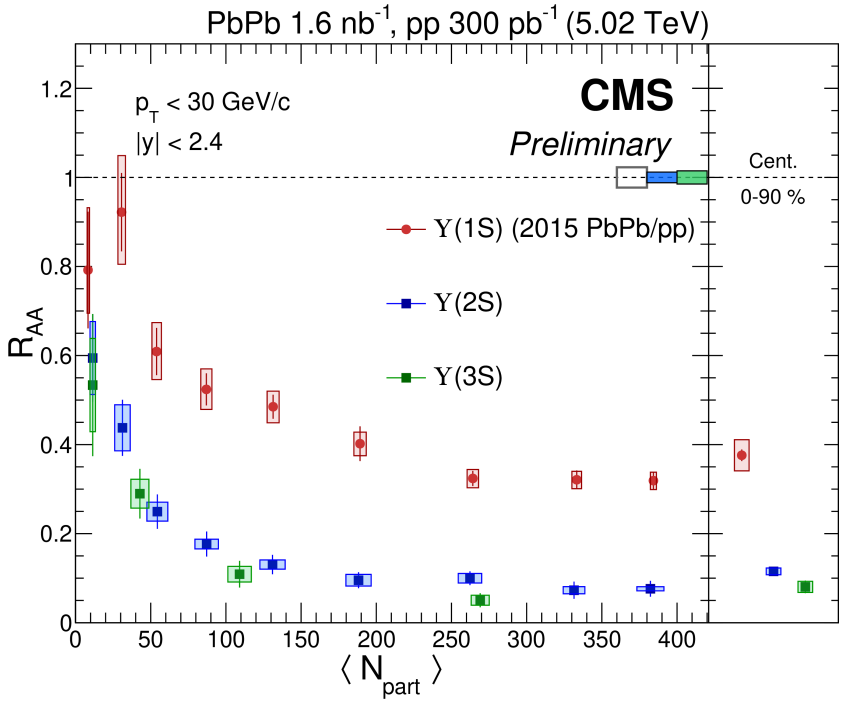

Figure 9: Nuclear modification factors for different Υ states as a function of $\langle N_{\mathrm{part}} \rangle$ [16].

for other hadrons, shown in Fig. 8, but $\Upsilon(3\mathrm{S})$ disappears already at $N_{\mathrm{part}} = 50$, which suggests that measuring it in small systems would be sensitive to the onset of the QGP.

Such a measurement (although not presented as such) was recently published by the CMS experiment [15]. Figure 10 shows the $\Upsilon(2\mathrm{S})/\Upsilon(1\mathrm{S})$ and $\Upsilon(3\mathrm{S})/\Upsilon(1\mathrm{S})$ yield ratios in different intervals of p_{T} as a function of charged particle multiplicity. This measurement shows that in pp collisions, the yields of excited $\Upsilon(n\mathrm{S})$ states are suppressed with respect to lighter states as the event multiplicity grows. The effect is stronger at lower p_{T} of $\Upsilon(n\mathrm{S})$. By analyzing event sphericity, the CMS related the observed effect to the relative importance of jet-like particle production vs. underlying event (UE) particle production, and the statement that is made about their measurement in the Discussion section of

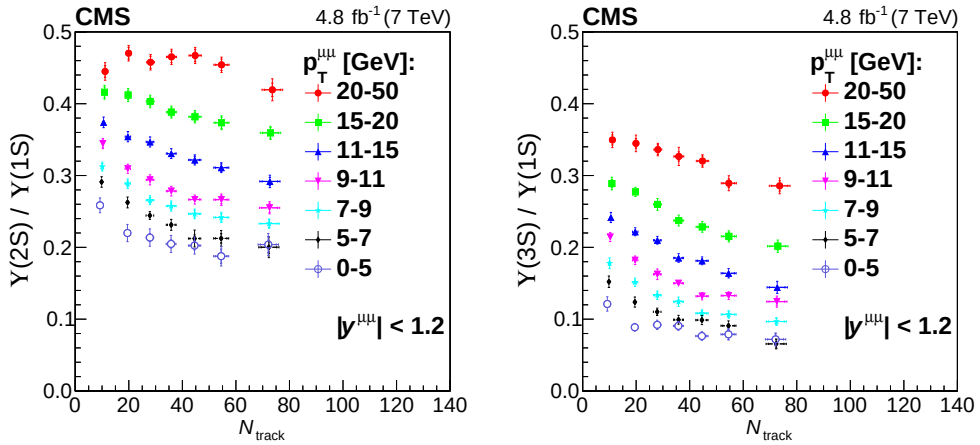

Figure 10: Ratios of $\Upsilon(2S)/\Upsilon(1S)$ (left) and $\Upsilon(3S)/\Upsilon(1S)$ as a function of multiplicity of charged particles measured by the CMS experiment. From Ref. [15]

the paper is the following: "*It was concluded that the feed-down contributions cannot solely account for this feature. This is also seen in the present analysis, where the* $\Upsilon(1S)$ *meson is accompanied by about one more track on average* ($n_{trk} = 33.9 \pm 0.1$) *than the* $\Upsilon(2S)$ ($n_{trk} = 33.0 \pm 0.1$)*, and about two more than the* $\Upsilon(3S)$ ($n_{trk} = 32.0 \pm 0.1$)*. [...] One could argue that, given the same energy of a parton collision, the lower mass of the upsilon ground state compared to the excited states would leave more energy available for the production of accompanying particles. On the other hand, it is also true that, if we expect suppression of the excited states at high multiplicity, it would also appear as a shift in the mean number of particles for that state (because events at higher multiplicities would be missing).*"

2.5 Quarkonium production

Quarkonia are bound states of quark and antiquark. Bound states of $c\bar{c}$ are called charmonia, and $b\bar{b}$ states are known as bottomonia. The hadron-hadron interaction can produce a pair of quark and antiquark via QCD-annihilation or via gluon fusion and splitting. At the LHC, the large distribution of gluons inside each proton makes the gluon fusion the dominant channel for large-Q^2 and small-x processes. The pre-quarkonium state formed has to emit gluons to equilibrate its degrees of freedom of angular momentum and/or color. There are various ways to recover the proper quantum numbers for each quarkonium wave function, shown in Figure 11, and some models have been proposed to describe the production process (for example, Color Evaporation Model [59], Color

Singlet Model [60], Non-Relativistic QCD model [61]).

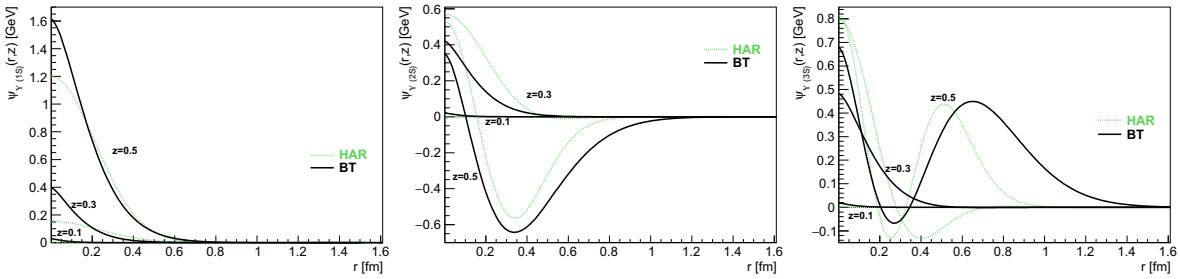

Figure 11: Wave functions for Υ mesons for different quark momentum fractions z [62]. The distribution function is generated by two models for the $b\bar{b}$ interaction potential: harmonic oscillator model denoted as HAR(green dotted lines) and Buchmuller-Tye parameterization, or BT(black solid lines).

Associating a quark and an antiquark of the same flavor in a bound state will result in constrained spectroscopy. One can model an effective quarkonium potential of the form

$$V(r) = \kappa r - \frac{\alpha_{\text{Coul.}}}{r} \tag{3}$$

that considering a non-relativistic interaction potential for two quarks Q and $\bar{Q}$ [63], where the string tension κ depends on the temperature T, and solves the Schrodinger equation to extract spectroscopy, i.e., energy levels that can be compared to experimental data by simply measuring the mass of each discovered resonance.

A variety of bound states corresponding to different radial (quantum number n_r) and orbital momentum (quantum number L) excitations and to different configurations of the quark spins (total spin S) are expected. The mass of each quarkonia state depends primarily on n and L [64]. Relativistic effects generate fine splittings as a result of spin-orbit and tensor interactions and hyperfine splittings arising from spin-spin interactions. The spin-parity of a given mass level is determined by its intrinsic quantum numbers: $|L-S| \leq J \leq |L+S|$, $P = (-1)^{L+1}$, $C = (-1)^{L+S}$. To denote different $b\bar{b}$, as well as $c\bar{c}$, levels, the spectroscopic symbol $n^{2S+1}L_{JPC}$ is used.

For both charm and beauty, the spectroscopy begins with a ground state with quantum numbers $n_r = 0$, $L = 0$, $S = 0$, and $J = 0$, which is usually identified as an η_c or an η_b mesons. One finds higher energy bound states of various quantum numbers up to the $D^0\bar{D}^0$ threshold or the $B^0\bar{B}^0$ threshold for charm and beauty, respectively. Above the threshold, the initial $Q\bar{Q}$ system contains enough rest energy to decay dominantly in D

or B mesons. The bottomonium spectroscopy is depicted in Figure 12. Table 1 represents

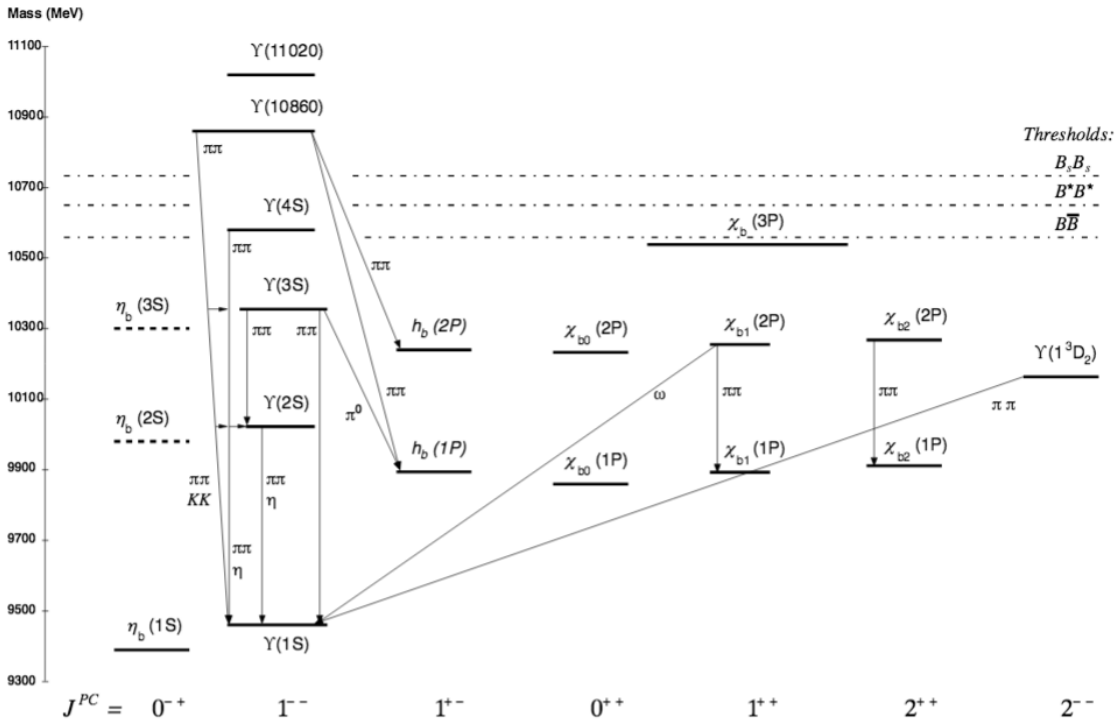

Figure 12: Bottomonium decay modes with spectroscopy notation [65].

the latest and the most accurate measurements of mass, full width, binding energy, and the most important decay modes for the three Υ states [23]. It is important to note the feed-down contribution. The Υ(2S) has around 18% probability of decaying into the Υ(1S) state plus two pions. The χ_b mesons can decay into Υ state and a photon. The Υ(3S) can also decay into Υ(2S) plus two pions or $\gamma\gamma$, or into Υ(1S) $\pi\pi$.

The theoretical study of the quarkonium production mechanism involves both perturbative and non-perturbative aspects of QCD. First, the creation of a $Q\bar{Q}$ pair occurs at a short distance scale and can be calculated in a perturbative approach. The $Q\bar{Q}$ pair creation involves a momentum transfer of the order of heavy quark mass m_Q, higher than the QCD scale parameter Λ_{QCD}. Then, the evolution of the $Q\bar{Q}$ pair into the physical quarkonium is non-perturbative. The typical momentum scale in such a case is the momentum of the heavy quarks, $m_Q v$, in the bound state rest frame, where v is the velocity of the heavy quark or antiquark in the quarkonium rest frame. An overview of models describing quarkonia production can be found in [13].

State	Υ(1S)	Υ(2S)	Υ(3S)
m (MeV/c^2)	9460.30 ± 0.26	10023.26 ± 0.31	10355.2 ± 0.5
Γ (keV/c^2)	54.02 ± 1.25	31.98 ± 2.63	20.32 ± 1.85
E_b (MeV)	1099	536	204
Main hadronic decays	ggg (81.7%)	ggg (58.8%)	ggg (35.7%)
	γgg (2.2%)	γgg (8.8%)	Υ(2S)$\pi^+\pi^-$ (2.8%)
	η' anything (2.9%)	Υ(1S)$\pi^+\pi^-$ (17.9%)	Υ(2S)$\pi^o\pi^o$ (1.9%)
	$D^{*(\pm)}$ anything (2.5%)	Υ(1S)$\pi^o\pi^o$ (8.6%)	Υ(2S)$\gamma\gamma$ (5.0%)
			Υ(1S)$\pi^+\pi^-$ (4.4%)
			Υ(1S)$\pi^o\pi^o$ (2.2%)
Main leptonic decays	e^+e^- (2.4%)	e^+e^- (1.9%)	seen
	$\mu^+\mu^-$ (2.5%)	$\mu^+\mu^-$ (1.9%)	$\mu^+\mu^-$ (2.2%)
	$\tau^+\tau^-$ (2.6%)	$\tau^+\tau^-$ (2.0%)	$\tau^+\tau^-$ (2.3%)

Table 1: Summary of the most important characteristics of Υ states. The percentages near the decay modes are the branching ratios [23].

3 Experimental methods

This chapter presents an overview of the kinematic variables, the Large Hadron Collider, and A Toroidal LHC Apparatus (ATLAS). We will also present a detailed description of different ATLAS sub-detectors.

3.1 Kinematic variables

In high-energy physics, particle kinematics is expressed in terms of azimuthal angle ϕ and polar angle θ, which at high energies is naturally replaced by its Lorenz-boost translator quantity called rapidity y (or pseudo-rapidity η). The z-axis is chosen colinear with the beam direction. Particle momentum, denoted p, has a longitudinal component p_z along the beam direction, whereas the other two components p_x, p_y are typically combined into the transverse momentum p_{T}, defined as

$$p_{\mathrm{T}} = \sqrt{p_x^2 + p_y^2}. \tag{4}$$

The rapidity y is defined in terms of particle kinematics and can be written as

$$y = \frac{1}{2} \ln \frac{E + p_z}{E - p_z}, \tag{5}$$

where E is the energy of a particle, $E = \sqrt{p^2 + m^2}$, where m is the particle rest mass.

The pseudo-rapidity η, mentioned earlier, is the limit $\eta = \lim_{p \gg m} y$. Measuring pseudo-rapidity does not require knowledge of particle mass and therefore is directly related to the polar angle θ:

$$\eta = -\ln \left(\tan \frac{\theta}{2} \right). \tag{6}$$

3.2 The Large Hadron Collider

The Large Hadron Collider (LHC) is the largest and the most complex particle accelerator. The facility has a circumference of 26.7 km and is built at European Organization for Nuclear Research (CERN) about 100 meters underground across the French-Swiss border [66]. It consists of a two-ring-superconducting hadron accelerator. Two high-energy particle beams travel in opposite directions in the ultrahigh vacuum beam pipes. These beams collide at four locations around the accelerator ring, where four main experiments are located: ATLAS, CMS, ALICE and LHCb. Figure 13 represents the CERN accelerator complex.

A Toroidal LHC Apparatus (ATLAS) [68] and the Compact Muon Solenoid (CMS) [69] are general purpose physics experiments, designed to measure established SM processes, detect the Higgs boson and potential physics beyond the SM. Apart from proton-proton collisions, these two experiments study HI collisions as well.

A Large Hadron Collider beauty (LHCb) [70] experiment is mainly focused on heavy-flavor physics. It was designed primarily to measure the parameters of CP violation in the interactions of b-hadrons. LHCb can also be operated in a fixed-target mode and investigate cosmic ray physics.

A Large Ion Collider Experiment (ALICE) [71] was designed to study the hot and dense medium created in HI collisions. ALICE uses pp and $p + \mathrm{Pb}$ primarily as a reference for $\mathrm{Pb} + \mathrm{Pb}$ measurements but also as a standalone physics program.

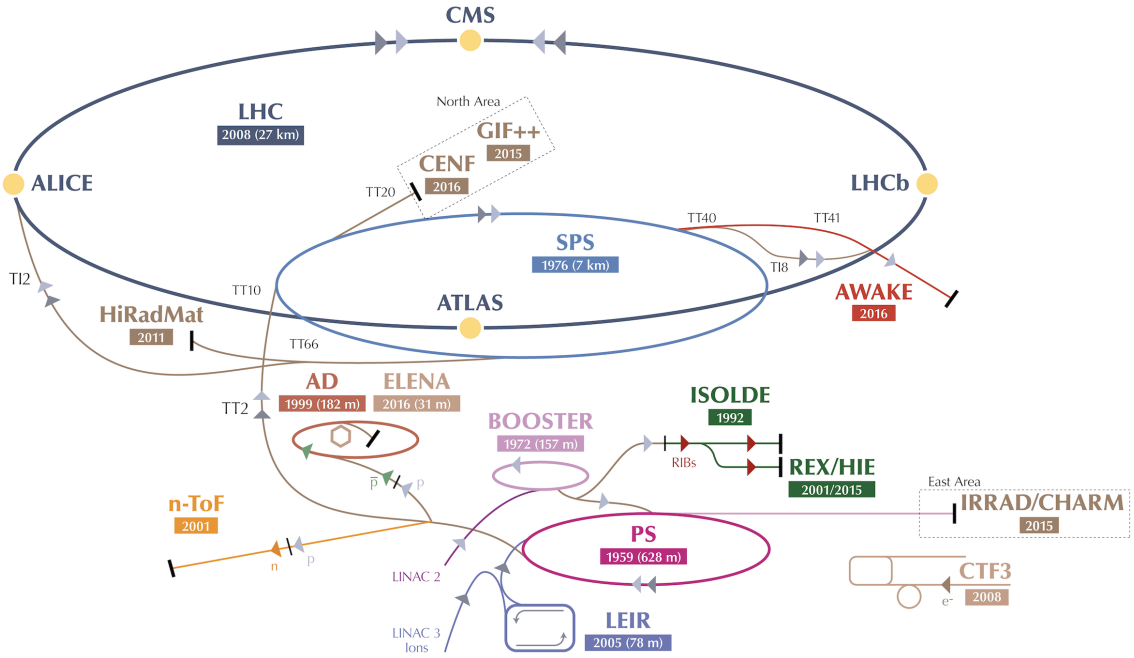

Figure 13: Schematic view of the CERN experimental complex and its four largest experiments [67]

3.3 ATLAS experiment

The ATLAS detector [72] at the LHC covers nearly the entire solid angle around the collision point.The collision point is surrounded by inner tracking devices followed by a superconducting solenoid providing a 2 T magnetic field, a calorimeter system, and a muon spectrometer. Below we discuss the main detector subsystems and their properties.

3.3.1 Inner detector.

The inner-detector (ID) system is immersed in the magnetic field and provides charged-particle tracking in the range $|\eta| < 2.5$. To satisfy the physics requirements of physics analyses for the vertex and momentum resolution, the tracking system is designed as a multi-layer silicon detector. This enables the hit reconstruction through robust pattern recognition and high precision in both R-ϕ and z coordinates.

The first hit is usually detected in the insertable B-layer [73–75] and followed by three more layers of the silicon pixel detector and four double layers of silicon microstrip trackers (SCT). These silicon detectors are complemented by the transition-radiation tracker (TRT), which enables radially extended track reconstruction up to $|\eta| = 2.0$. In

HI collisions, the TRT is not used in the track reconstruction due to very high occupancy in its channels. The ATLAS ID system cross-section summary is shown in Figure 14.

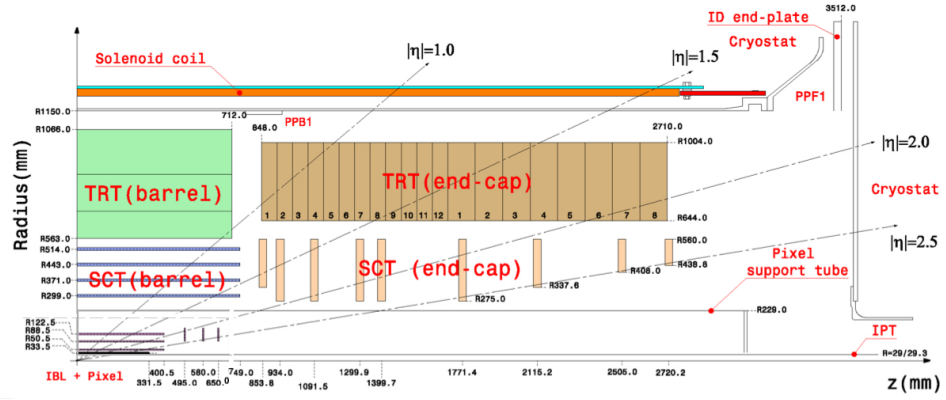

Figure 14: The layout of the ATLAS inner tracking detector: IBL, Pixel, SCT and TRT detector layers [75].

The primary vertex resolution improves with more activity in collisions, so in pp collisions, it ranges from 30 μm for events with 70 tracks to about 80 μm for events with 20 tracks, while in HI collisions, it exceeds 10 μm. The momentum resolution of the tracking system depends linearly on the track momentum both in pp and A+A systems, and it grows in the forward η region. Typically, for $|\eta| < 1.9$, it ranges from 3% up to 10 GeV and rises to approximately 10% at 100 GeV. For more forward tracks, the momentum resolution worsens from 8% to 15% in the same momentum range.

3.3.2 Calorimeters.

The two main components of the ATLAS calorimetry system are the Liquid Argon (LAr) Calorimeter and the Tile Hadronic Calorimeter (TileCal). They cover a wide range of $|\eta| < 4.9$ and are designed to stop and measure the energy loss of electrons, photons, and charged hadrons (jets). The total thickness of the electromagnetic (EM) calorimeter is larger than 22 radiation lengths (X_0) in the barrel and larger than 24 (X_0) in the end-caps. The approximate 9.7 interaction lengths (λ) of the active calorimeter in the barrel (10λ in the end-caps) are adequate to provide a good resolution for high-energy jets. The cross-section view of the ATLAS calorimeter system is shown in the left panel of Figure 15 with all the subsystems.

LAr calorimeters are divided into EM barrel ($|\eta| < 1.475$) and end-cap ($1.375 < |\eta| < 3.2$), LAr hadronic end-cap calorimeter ($1.5 < |\eta| < 3.2$) and LAr forward calorimeter

$(3.1 < |\eta| < 4.9)$. They are placed inside three aluminum cryostats and supplied by liquid Argon at -183 °C. The operation technology is based on the noble-liquid sampling calorimetry where alternating layers of absorbers (lead or copper) and active gas components with high-voltage Kapton electrodes are used to degrade the energy of an incident particle and measure the ionization signal coming from the EM or hadronic shower. Electrodes are arranged in the accordion geometry that provides complete ϕ symmetry without azimuthal cracks. The energy resolution for the EM barrel and end-cap is about $10\%/\sqrt{E}$. A schematic representation of the EM calorimeter basic structure is shown in the right panel of Figure 15. The barrel calorimeter consists of two identical half-barrels, separated by a small gap (4 mm) at $z = 0$. Each end-cap calorimeter is mechanically divided into two coaxial wheels: an outer wheel covering the region $1.375 < |\eta| < 2.5$, and an inner wheel covering the region $2.5 < |\eta| < 3.2$.

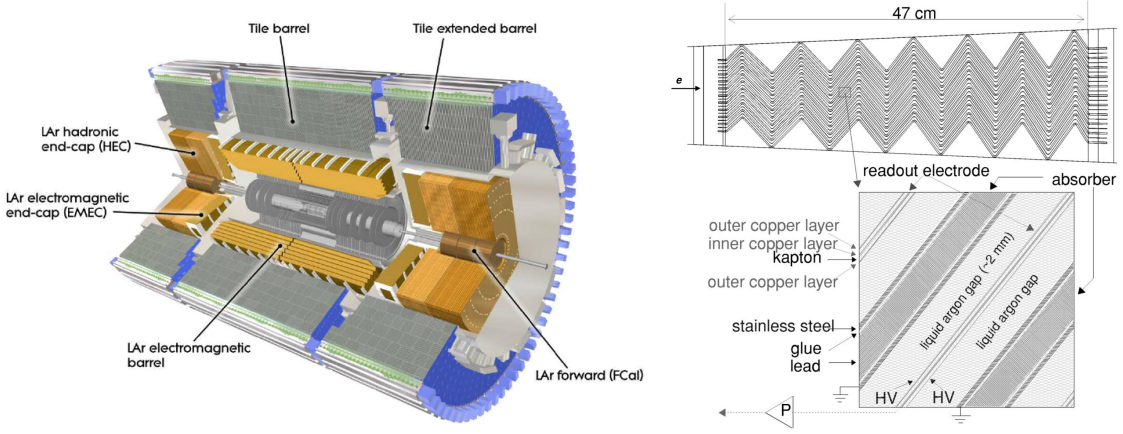

Figure 15: (*Left*) Side-view of the ATLAS calorimeter system [76]. (*Right*) Schematic view of the structure of the ATLAS EM calorimeter [77].

The forward calorimeters (FCals) are located in the same cryostat as the end-cap calorimeter, and they consist of three modules in each end-cap: the first, made of copper, are optimized for electromagnetic measurements, while the other two, made of tungsten, measure predominantly the energy of hadronic interactions. Due to a very high incoming particle flux, the design of the FCal modules is based on the electrode structure of small-diameter rods centered in tubes that are oriented parallel to the beam direction. The LAr gaps, which are the sensitive element, are smaller than 2mm. The energy resolution of FCal is about $100\%/\sqrt{E}$.

LAr hadronic end-cap calorimeter (HEC) provides hadronic coverage and provides an

energy resolution of about $60\%/\sqrt{E}$. It has parallel copper plate absorbers orthogonal to the beam axis assembled into two consecutive wheels. The FCal consists of three modules in each end-cap: the first, made of copper, is optimized for electromagnetic measurements, while the other two, made of tungsten, measure predominantly the energy of hadronic interactions. The energy resolution of the EM layer is about $30\%/\sqrt{E}$ and of the hadronic modules around $80\%/\sqrt{E}$ [78].

TileCal is a sampling calorimeter using iron as absorber material and scintillating tiles as an active material. It is placed directly outside the EM calorimeter. Both sides of the tiles are read by wavelength-shifting fibers into two separate photomultipliers. The calorimeter is split into a barrel and two extended barrel parts. It provides an energy resolution of approximately $40\%/\sqrt{E}$ for pions.

In addition to the calorimeters described above, the ATLAS system also uses Zero-Degree Calorimeters (ZDC) for detecting forward neutrons with $|\eta| > 8.3$ in HI collisions. The ZDC are divided into two arms and resides inside the TAN (Target Absorber Neutral) absorber ± 140 m from the interaction point. Their design is based on scintillating sampling calorimeter technology using quartz rods as an active material readout by photomultipliers and tungsten and steel as absorption material. The single neutron energy resolution for the spectator neutron energy of 2.51 TeV is about 17%. By requiring a tight coincidence from the two arms of the ZDC, background processes from beam-gas, and beam-halo effects can be significantly reduced. The ZDC coincidence is also a basis of the minimum-bias (MB) trigger algorithm in HI collisions. Such triggers are designed to collect a large fraction of the total inelastic Pb+Pb cross-section while introducing as little selection bias as possible. By requiring a single-sided ZDC signal or no signal in the ZDC (below the energy of a single neutron), one can tag photon-nuclear and ultra-peripheral EM processes that leave one or both of the incident nuclei intact.

3.3.3 Muon spectrometer

The Muon Spectrometer (MS) was designed to detect muons in the pseudorapidity region up to $|\eta| = 2.7$ and to provide better momentum resolution measurement in the central part of the detector after combining the information with the ID. The measurement technology is based on the magnetic deflection of muon tracks in the large superconducting air-core toroid magnets, instrumented with separate triggers and high-precision tracking

chambers. The layout of the MS is shown in Figure 16. The magnetic system consists of a barrel toroid magnet that covers the regions of $|\eta| < 1.4$ and two smaller end-cap toroids that deflect muons in the region $1.6 < |\eta| < 2.7$; the magnetic field in the transition region is provided by a combination of both barrel and end-cap magnets. The bending power of the magnets, quantified as $\int B\mathrm{d}l$ where integral is evaluated between the first and the last chamber, is in the range from 1 to 7.5 Tm.

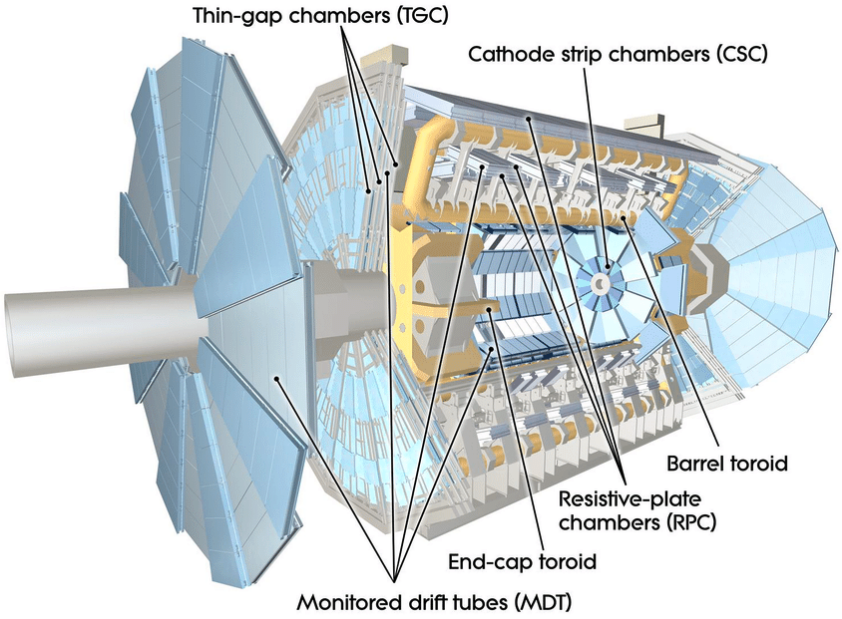

Figure 16: The layout of the ATLAS muon spectrometer with all types of muon chambers indicated [76].

Precision tracking of muons is done by Monitored Drift Tubes (MDTs) in the coverage of $|\eta| < 2.7$. A basic measuring element is a gas-filled tube, 1–6m long, with an anode that is at +3300 V so that it creates an avalanche of ionization electrons created by an incident muon. The gas mixture used is Ar-CO_2 (93–7%) at 3 bar, where Ar ensures a large primary ionization yield and CO_2 is a quencher gas that absorbs the UV photons from excited Ar atoms. The tubes are assembled into multilayers inside chambers that finally provide 50μm position resolution (single drift tube resolution is about 80 μm). Muon momentum resolution measured with MDTs is from 2–4% for muons from 10–200 GeV and rises to 12% for 1 TeV muons.

In the region $|\eta| > 2$, the counting rate exceeds the MDT requirements for safe operation (above 150 $\mathrm{cm}^2\mathrm{s}^{-1}$). Therefore, MDTs are replaced with cathode-strip chambers

(CSC), which are multiwire proportional chambers with the wires oriented in the radial direction and segmented into strips to provide the position measurements. The position resolution of the CSC plane is 60 μm with a good two-track resolution. CSC can be operated safely up to 10^3 cm^{2}s^{-1} rate.

An additional detector subsystem is installed inside the MS for triggering purposes. In the barrel ($|\eta| \leq 1.05$), Resistive Plate Chambers (RPCs) are used, which are gaseous parallel electrode-plate detectors. They have good spatial ($\sim$1 mm) and time resolution (about 2 ns) as well as adequate rate capability. In the end-cap region, Thin Gap Chambers (TGCs) have been selected, which operate on the same principle as multi-wire proportional chambers, and they provide good time resolution ($\sim$4 ns) and high rate capability.

Trigger system A two-level trigger system is used to select events for this analysis. The first-level trigger is implemented in hardware and uses a subset of the detector information. High-p_{T} muons are identified using RPC and TGC signals as described above. Calorimeter selections are based on reduced-granularity information from all the calorimeters. Results from the L1 muon and calorimeter triggers are processed by the central trigger processor, which implements a trigger "menu" made up of combinations of trigger selections. There is a possibility of implementing additional "event prescales", which further reduce the recorded output rate for each trigger in the menu. The L1 trigger sequence is followed by the software-based High-Level Trigger (HLT) system, which can run offline reconstruction and calibration software, further reducing the event rate. An example of this is quality requirements applied to the EM shower associated with electron and photon HLT objects.

4 Analysis 1: Correlation of Upsilon meson production with the UE

While this analysis was in work, the CMS experiment published the results [15], which investigate the same physics phenomenon as is studied in this work. The outcome of the CMS publication is discussed in Section 1. To make statements that go beyond the admissions of the CMS experiment, this analysis uses a different approach.

Instead of measuring the $\Upsilon(n\mathrm{S})$ yield as a function of the number of charged particles as a proxy for the size of the Underlying Event, the UE properties are measured for different $\Upsilon(n\mathrm{S})$ states in different intervals of meson p_{T}. This technical change allows a more thorough investigation of the nature of the $\Upsilon(n\mathrm{S})$ suppression in pp collisions that may lead to a more conclusive statement about the nature of this phenomenon. The analysis uses $\sqrt{s} = 13$ TeV data with more significant statistics, which is possible due to the pileup (PU) subtraction technique developed by the group of the Weizmann Institute of Science and used in a previous ATLAS measurement [79].

Even the first look at the ATLAS 'raw data' shown in Figure 17 reveals significant

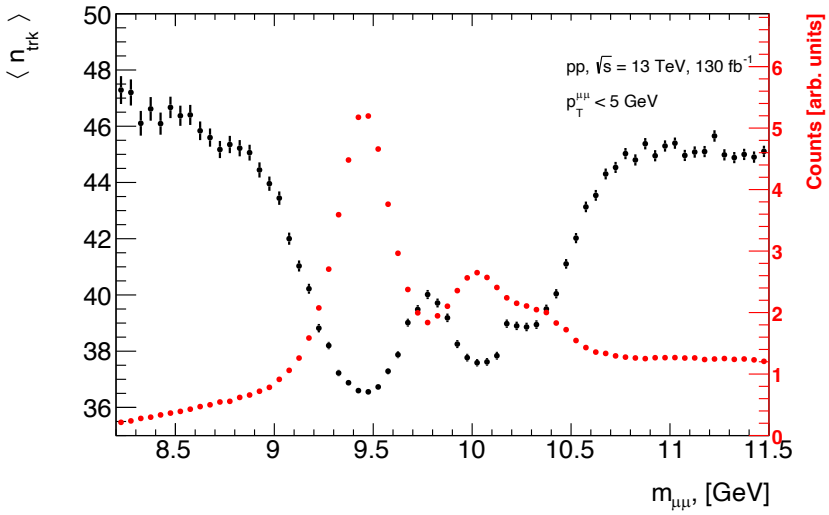

Figure 17: Black: $\langle n_{\mathrm{ch}} \rangle$ vs. the invariant mass of the dimuon. Red: invariant mass distribution. Tracks are matched to the dimuon vertex, dimuons are matched to the trigger.

differences in the number of tracks (n_{trk}) in collisions with different $\Upsilon(n\mathrm{S})$ states. The

figure shows invariant mass distribution ($m_{\mu\mu}$) plotted with red markers superimposed on the graph of $\langle n_{\text{trk}} \rangle$ in a collision plotted with black markers. Combining two different quantities on the same plot follows the purpose of visual comparison. This comparison clearly shows that in the region of $\Upsilon(n\text{S})$ peaks, there are fewer tracks when in the region of the "substrate". The substrate is formed by combinatorial muon pairs coming from di-jets and the Drell-Yan. The average multiplicities, shown in black, are $\langle n_{\text{trk}} \rangle = f\langle n^s_{\text{trk}} \rangle + (1-f)\langle n^b_{\text{trk}} \rangle$, where n^s_{trk} and n^b_{trk} are signal and background multiplicities and $f = f(m_{\mu\mu})$ is the signal fraction. Note that the $\langle n^b_{\text{trk}} \rangle$ has to be approximately the same in the entire mass interval because at the limits of the interval where the contribution from Υ mesons is small, the average values of the substrate $\langle n^b_{\text{trk}} \rangle$ are consistent within $1-2$ tracks. If the $\langle n^s_{\text{trk}} \rangle$ would also be the same for each of the three $\Upsilon(n\text{S})$ states, the black curve would mirror the shape of the Υ-peaks in the red curve $\langle n_{\text{trk}} \rangle \propto 1 - \big(1 - \langle n^s_{\text{trk}} \rangle / \langle n^b_{\text{trk}} \rangle\big) \times f = 1 - \text{Const} \times f(m_{\mu\mu})$. This is clearly not the case because the black curve in the $\Upsilon(3\text{S})$ mass region is just slightly higher than in the $\Upsilon(1\text{S})$ mass region, suggesting that the signal fraction f is comparable, but this clearly contradicts the red curve, which shows very different signal fractions in $\Upsilon(3\text{S})$ and $\Upsilon(1\text{S})$ mass regions. Thus $\langle n^s_{\text{trk}} \rangle$ cannot be the same for all $\Upsilon(n\text{S})$ states.

This analysis utilizes two types of different objects, $\Upsilon(n\text{S})$ produced in hard scattering processes and soft hadrons that build the UE of the collision. In the course of analysis, some steps are intended for correcting Υ yields while others deal with charged particles. The sequence of operations performed in the analysis follows the goal of minimizing final uncertainties. For example, fitting the invariant mass distributions is done for all UE multiplicities and all PU conditions to increase the accuracy of the fitting. Also, since the analysis was performed in a somewhat exploratory manner, i.e., without clear knowledge of what variables would be most important for the final statement, the analysis is performed to keep maximum flexibility. For example, all track-based corrections are implemented as weights on a track-by-track basis so that any kinematic distribution with tracks can be constructed from the data.

4.1 Data samples

The analysis is based on the entire Run-2 statistics acquired by the ATLAS detector in 2015–2018 from *pp* collisions produced by the LHC at $\sqrt{s} = 13$ TeV. Data were recorded

in Main and BPhysLS physics data streams. Events are selected by dimuon Υ triggers[1] listed in the Table 2.

Text Name	Full HLT Trigger Name	2015	2016	2017	2018
2mu4	2mu4_bUpsimumu	3.1			
	2mu4_bUpsimumu_L1BPH-...		6.9		
mu6mu4	mu6_mu4_bUpsimumu	3.9	9.5	[1.7]	
	mu6_mu4_bUpsimumu_L1BPH-...			[30.1]	[42]
2mu6	2mu6_bUpsimumu	3.9	20	[2.6]	
	2mu6_bUpsimumu_L1BPH-...			47.5	62.8
mu10mu6	mu10_mu6_bUpsimumu		25.1	3	
mu11mu6	mu11_mu6_bUpsimumu			[48.9]	[62.9]
	mu11_mu6_bUpsimumu_L1LFV-MU11				[62.7]
2mu10	2mu10_bUpsimumu	3.9	29.6	[48.9]	[62.9]

Table 2: LHC Run-2 statistics in fb^{-1} of the dimuon Υ triggers used in this analysis. The number in square brackets indicates that the trigger was recorded in the BPhysLS stream, whereas without brackets in the Main stream.

There are several official ATLAS Monte Carlo samples of three different states of Upsilon mesons used to estimate tracking performance and fit dimuon mass spectra. In addition, standalone Pythia8 with the A14 tune was run to produce generated-level distributions. The primary purpose of this production was to generate large statistics of prompt and feed-down $\Upsilon(n\text{S})$ production, and this truth-level standalone Pythia8 production is used only for comparison with the fully corrected data and not for calculating corrections or any other data analysis, which is done with the official ATLAS MC samples.

[1]Full trigger names are:

HLT_2mu4_bUpsimumu_L1BPH-1M19-2MU4-BO_BPH-0DR34-2MU4

HLT_mu6_mu4_bUpsimumu_L1BPH-8M15-MU6MU4_BPH-0DR22-MU6MU4-BO

HLT_2mu6_bUpsimumu_L1BPH-8M15-2MU6_BPH-0DR22-2MU6

4.2 Event and track selections

The main goal of event and track selections is to minimize systematic uncertainties by selecting high-quality data for the physics analyses. The $\Upsilon(n\mathrm{S})$ mesons are reconstructed from their decay to oppositely charged muon pairs. All events are selected according to detector quality conditions during the data taking summarized in the "Good Run List" (GRL) to ensure a high quality of events selected for the analysis. Each event is assigned to only one trigger, listed in Table 2, by matching reconstructed muons to HLT objects using standard ATLAS tools [80]. Four muon types are defined depending on which subdetectors are used in reconstruction:

- *Combined muons* - track reconstruction is performed independently in the ID and MS, and a combined track is formed with a global refit that uses the hits from both ID and MS subdetectors.

- *Segment-tagged muons* - a track in the ID is classified as a muon if it is associated with at least one local track segment in the MDT or CSC chambers.

- *Calorimeter-tagged muons* - a track in the ID is identified as a muon if it can be mathced to an energy deposit in the calorimeter compatible with a minimum-ionizing particle.

- *Extrapolated muons* - the muon trajectory is reconstructed based only on the MS track and a loose requirement on compatibility with originating from interaction point.

In the offline analysis, muons are reconstructed as combined tracks spanning both the inner-detector system (ID) and the muon spectrometer (MS). Muons are required to fall within the fiducial acceptance of the ATLAS detector, defined as $p_{\mathrm{T}}^{\mu} > 4$ GeV and $|\eta^{\mu}| < 2.4$. This offline selection is used for the data obtained with the lowest muon p_{T} trigger. For the data samples obtained with higher muon-p_{T} triggers, the offline selection uses higher p_{T} values, matching the nominal momentum of the trigger. Tight quality requirements are imposed on the muon track both in the ID and MS to suppress backgrounds [81]. Muons associated with a common vertex must have a longitudinal impact parameter of less than 0.5 mm, and the significance of the transverse impact parameter is required to be less than 3.

Events with two oppositely charged muons that satisfy these criteria and are matched to HLT objects are selected for analysis. The muons are required to form a pair with invariant mass in the interval $8.2 \leq m^{\mu\mu} \leq 11.8$ GeV, and within the rapidity $|y^{\mu\mu}| < 1.6$. The rapidity condition is used to avoid detector regions where the acceptance is different for different $\Upsilon(n\mathrm{S})$ states. The dimuon vertex is required to be within $|z_{\mathrm{vtx}}| < 140$ mm (see Section 4.5.1). An event is also required to pass the PU cleanup procedure and have instantaneous luminosity, which is the actual number of interactions per bunch crossing, $\mu < 50$ (see Section 4.3).

Only primary charged particles, with p_{T} between 0.5 and 10 GeV, and $|\eta| < 2.5$, are considered in the analysis. These are defined as particles with an average lifetime $\tau > 0.3 \times 10^{-10}$ s and produced directly in the interaction or those from decays of particles with a shorter lifetime. Charged particles are identified as tracks reconstructed in the ID. Tracks are required to pass a set of quality requirements in the ID according to the track reconstruction model [82] and to have p_{T} and η in the same range defined as the charged particle acceptance. Muon tracks coming from Υ decays are used only to reconstruct the Υ state and are not counted as charged particles. Only tracks that fall within 0.5 mm from the averaged vertex position in the transverse direction and within 0.75 mm from the position of the vertex associated with muons in longitudinal directions are considered. The latter conditions significantly reduce the number of PU tracks selected for the analysis but do not eliminate them completely.

4.3 Evaluation of the PU

Pileup, specifically in-time pileup (PU) which is relevant for this analysis, is an increase in the number of tracks caused by independent pp collisions that occur during the crossing of two opposite going bunches at the ATLAS interaction point together with the collision that produces the process of interest. There are two mechanisms by which the PU changes the number of tracks measured in collisions. One is by adding tracks from other interactions unrelated to the trigger and another by increasing the detector occupancy that leads to the production of fake tracks, i.e. spurious associations of hits present in the detector. The two processes can be called "linear" and "non-linear" track production mechanisms, respectively. We note that although it is in some sense a second-order effect the latter one may have a significant magnitude. Turn-on of the second mechanism is visible in the data

in Figure 18 which shows the number of tracks in an event per interaction as a function of the number of interactions per bunch crossing (μ).

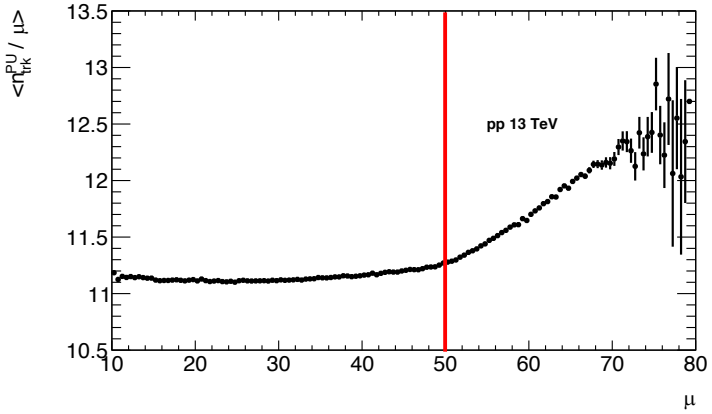

Figure 18: The average value of n_{trk} per interaction in pp collisions as a function of the number of inelastic pp interactions per bunch crossing μ.

Below $\mu = 50$, the mean number of tracks scales with μ, but at larger values, it starts to grow due to increasing occupancy in the detector. Following the recommendation of the Tracking CP working group [83], this analysis is restricted to events with $\mu < 50$. The non-linear PU production mechanism is suppressed by this cut but is not eliminated and is discussed later in Section 4.6. Here the focus is on the linear PU component, dealing with which follows the methodology developed in the analysis of two-particle correlations in Z-boson tagged events [79] and detailed in its supporting note [84]. Only the basic steps of this procedure are reviewed here; other details can be found in the note. Absolute numbers that appear in some plots in this section include corrections that are explained later. They are shown here to explain the procedure.

A bigger part of the PU tracks is rejected by matching tracks to the trigger vertex (the trigger vertex is the vertex associated with the di-muons firing the trigger), and the irreducible part of the PU is subtracted on a statistical basis using 'event mixing' technique. A technical difference between this and the Z-ridge paper analyses is that when the Z produces two energetic muons, the primary event vertex and the trigger vertex are almost always the same. When relatively lighter Υ meson decays into less energetic muons, there exists a non-negligible probability that the primary event vertex (the vertex with the highest $\sum p_{\text{T}}$ of all track) can be different from the vertex from which the Υ originates. The width of the tracks-to-vertex matching peak is similar in both analyses

and is close to about three times the width of the $(z_0 - z_{\text{vtx}})\sin(\theta)$ distribution. This width is denoted ω_0 and is equal to 0.75 mm. Parameter z_0 is the longitudinal coordinate of the point of the closed approach of the track to the beamline, and θ is the track polar angle. Apart from this technicality, the PU subtraction follows the steps described in [79].

Each recorded event contains subevents:

- *Direct* subevent consist of tracks that satisfying criterion $\left|\left(z_0^{\text{trk}} - z_{\text{vtx}}\right)\sin(\theta)\right| < \omega_0 = 0.75$ mm. It contains both *Signal* subevent tracks from the trigger vertex and *Background* subevent tracks from PU interactions.

- A sample of events on average identical to the *Background* subevents can be constructed as explained in [84] by picking tracks from other events. This sample is called the *Mixed* event sample.

The random selection procedure used to construct such a sample implies that tracks building each *Mixed* event shall be picked from an inclusive pp event sample at the point of the same $\mathrm{d}\mu/\mathrm{d}z_{\text{vtx}}$ (longitudinal interaction density) as it is for *Direct* event and using the same ω_0 selection criterion. The latter requirement is trivial, but finding the point of the same interaction density requires precise knowledge of the z_{vtx} distribution and μ. The shape of the z_{vtx} distribution is very well approximated by a Gaussian distribution and can be characterized with its mean value $\langle z_{\text{vtx}}\rangle$ and the RMS. To compare interaction density between different events, the analysis uses reduced coordinates: $z_{\text{vtx}} \to \bar{z}_{\text{vtx}} = \frac{z_{\text{vtx}} - \langle z_{\text{vtx}}\rangle}{\text{RMS}(z_{\text{vtx}})}$ and $\mu \to \bar{\mu} = \frac{\mu}{2\pi \text{RMS}(z_{\text{vtx}})}$. The same interaction density, therefore, corresponds to the same value of $\mathrm{d}\bar{\mu}/\mathrm{d}\bar{z}_{\text{vtx}}$ in two events.

The key variables that are used to construct $\bar{\mu}$ and $\bar{z}_{\text{vtx}}$ are $\langle z_{\text{vtx}}\rangle$, $\text{RMS}(z_{\text{vtx}})$ and μ are studied in each run in each luminosity block (or lumiblock) following the procedure implemented in [84]. In the ATLAS experiment, a lumiblock is a time interval, usually around one minute, of data recording over which the experimental conditions are assumed to be constant [85]. In particular, the instantaneous luminosity is calculated as an average number over the duration of one luminosity block. If the data-recording configuration changes, a new luminosity block is started. Figure 19 on the left shows the lumiblock dependence of μ for one run. Continuous intervals are approximated by a polynomial function, and the lumiblocks where the measured μ deviates by more than four standard deviations are marked for rejection. Some lumiblocks are also rejected by eye inspection. Rejected lumiblocks are marked with red and green markers. For the remaining

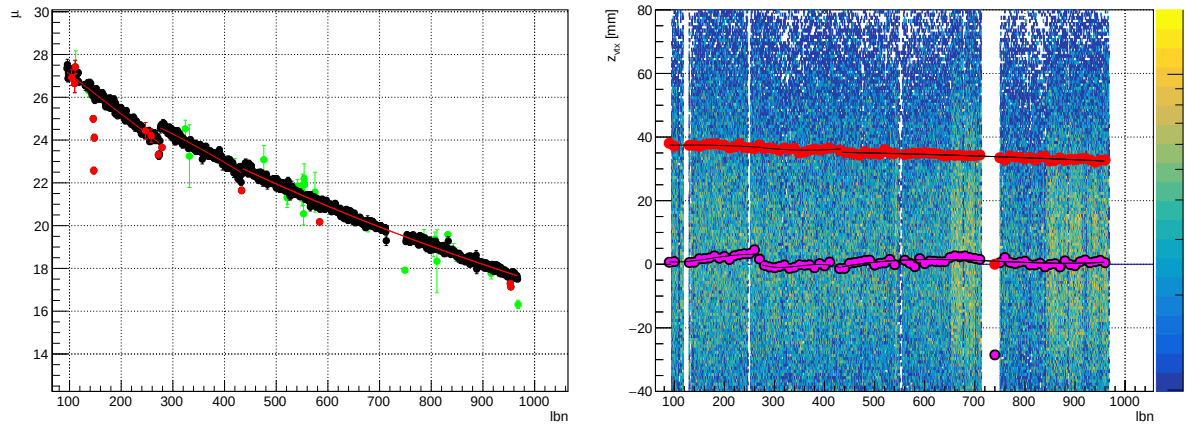

Figure 19: An example of a calibration procedure applied to a single run. Left: Instantaneous luminosity μ as a function of the lumiblock number in a selected run. Rejected points are marked with red and green markers. Right: $\langle z_{\text{vtx}} \rangle$ (magenta) and RMS(z_{vtx}) (red) as a function of the lumiblock number.

lumiblocks, the $\langle z_{\text{vtx}} \rangle$ and RMS(z_{vtx}) are calculated and approximated by polynomials in the regions of continuity. These parameterizations are then used to calculate values of $\langle z_{\text{vtx}} \rangle$ and RMS(z_{vtx}) that are used in the analysis in Equation (8). Other parameters are also inspected for unexpected features as a part of the procedure that, in the end, rejects about 10% of total statistics.

The *Mixed* event sample is most straightforwardly constructed from an inclusive event sample which can be obtained with the random recording of filled bunch crossings. However, this requires handling additional event samples. Instead, this analysis followed the same approach as for the Z-ridge paper, where the trigger event sample is also used to produce *Mixed* events. This requires an additional condition on the location of z_{vtx} in two events i and j to ensure that the tails of the trigger events do not add unwanted tracks: $\left|\left(z^i_{\text{vtx}} - z^j_{\text{vtx}}\right)\right| > 15$ mm. Figure 20 explains the selection procedure, including all requirements. Each x-y frame in the picture denotes an event in the trigger sample. An event with the Υ candidate is filled with blue color. All events highlighted in colors have the same $\bar{\mu}$ and are considered for mixing at this step, while all others are not and therefore are shown in grey. They, however, can be used for other events. A blue band denotes the ω_0 selection criterion. It is applied to tracks in highlighted events at the same $\bar{z}_{\text{vtx}}$ as in the event with Υ. All tracks in each highlighted event falling within the blue band would build one *Mixed* event. The exception is the event drawn in red color, which

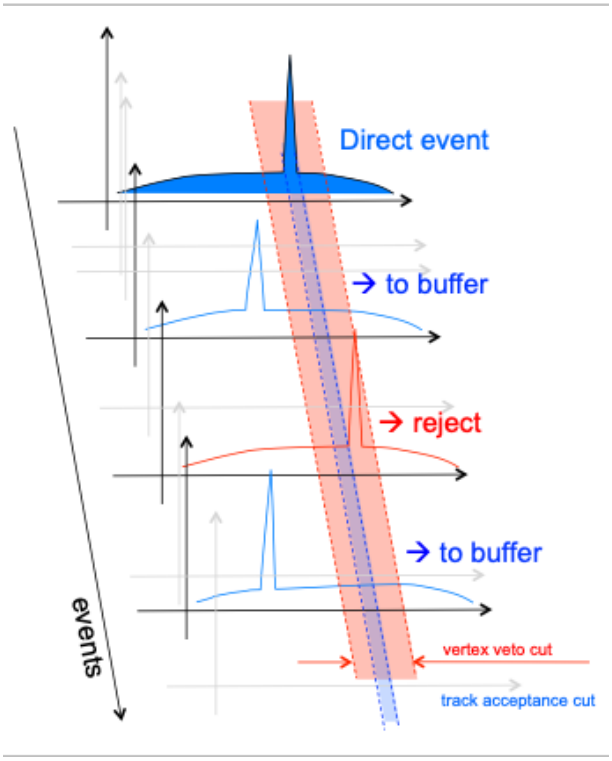

Figure 20: Schematic explanation of the random selection procedure

is rejected because the trigger vertex falls within the red band with the location of the trigger vertex in *Direct* event. The write-up given here is only an approximate explanation of the procedure. It jumps between absolute and reduced coordinates and does not elaborate on the fact that each rejection of an event with close vertices requires that another event is found to replace it to keep a proper balance between the samples. Those are detailed that can be implemented in the analysis in different ways. In this analysis, about 20 *Mixed* events are built for each *Direct* one, all within the same data-taking run to ensure that the detector conditions are the same for the two samples.

The track density distribution $\mathrm{d}n_{\mathrm{trk}}/\mathrm{d}\omega$ along ω coordinate $\omega = \left(z_0^{\mathrm{trk}} - z_{\mathrm{vtx}}\right)\sin\left(\theta\right)$ is shown for *Direct* and *Mixed* events in Figure 21. Full markers show *Direct* events, and open markers show *Mixed* events that follow the PU substrate under the peak in *Direct* events. Elevations seen in *Mixed* events away from the peaks are an artifact due to using the triggered sample rather than an unbiased, inclusive sample for constructing *Mixed* events (as explained above). More details about this effect are given in [84]. Lines fitted to *Mixed* distributions are the parabolic functions

$$\frac{\mathrm{d}n_{\mathrm{trk}}}{\mathrm{d}\omega} = \left.\frac{\mathrm{d}n_{\mathrm{trk}}}{\mathrm{d}\omega}\right|_{\omega=0} \left(1 + S\omega + C\omega^2\right) \tag{7}$$

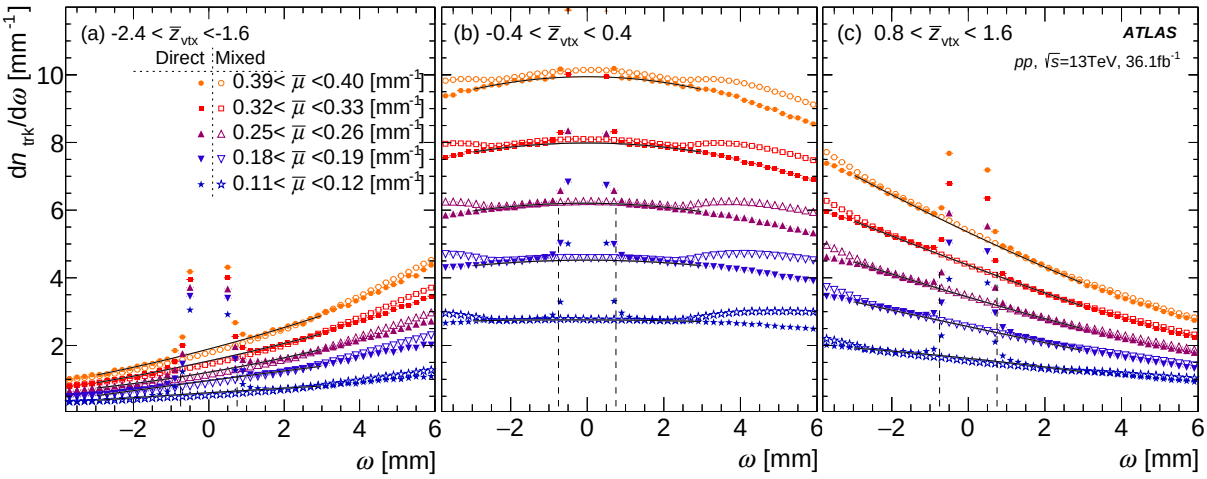

Figure 21: Track pointing to the trigger vertex in *Direct* (full markers) and *Mixed* (open markers) events, at different $\bar{\mu}$ for three location of $\bar{z}_{\rm vtx}$. The plot is from [84].

from which the values of $\mathrm{d}n_{\rm trk}/\mathrm{d}\omega$ at $\omega = 0$ can be extracted. Terms with coefficients (S)lope and (C)urvature play no role in the analysis since the first cancels out in integration over $\pm\omega_0$, and the second produces a negligibly small correction. The left panel of Figure 22 shows $\mathrm{d}n_{\rm trk}/\mathrm{d}\omega$ at $\omega = 0$ as a function of $\bar{\mu}$ plotted for various locations of $\bar{z}_{\rm vtx}$. Curves are for *Mixed* data, and as shown in Ref. [79], fits of the *Direct* events give identical results. All curves are consistent with linear behavior, which reflects the fact that at a fixed vertex location $z_{\rm vtx}$ ($\bar{z}_{\rm vtx}$), the PU track density is proportional to the number of interactions per bunch crossing μ ($\bar{\mu}$). Slopes of the linear fits $\mathrm{d}^2n_{\rm trk}/\mathrm{d}\omega\mathrm{d}\bar{\mu}$ are plotted in the right panel of the figure as a function of $\bar{z}_{\rm vtx}$. The Gaussian fit gives the magnitude of the peak, mean value, and width, with the latter two being consistent with 0 and 1. (Mean and width equal to 0 and 1 are expected due use of the reduced $\bar{z}_{\rm vtx}$ coordinate.)

Equation (8) defines an estimator of the mean value of the number of PU tracks that fall within $\pm\omega_0$ around a given point in an event. This is the PU estimator ν used to characterize PU condition of events

$$\nu = 2\omega_0 \frac{\mathrm{d}^2 n_{\rm trk}}{\mathrm{d}\omega \mathrm{d}\bar{\mu}}\bigg|_{\bar{z}_{\rm vtx}=0} G\left(\bar{z}_{\rm vtx}\right)\bar{\mu} \tag{8}$$

where $G\left(\bar{z}_{\rm vtx}\right)$ is the Gaussian profile of the reduced trigger vertex position. As one can see from Figure 22, the function accurately fits the data, and that is because the longitudinal beam profiles in the LHC are very close to Gaussian. The magnitude of the

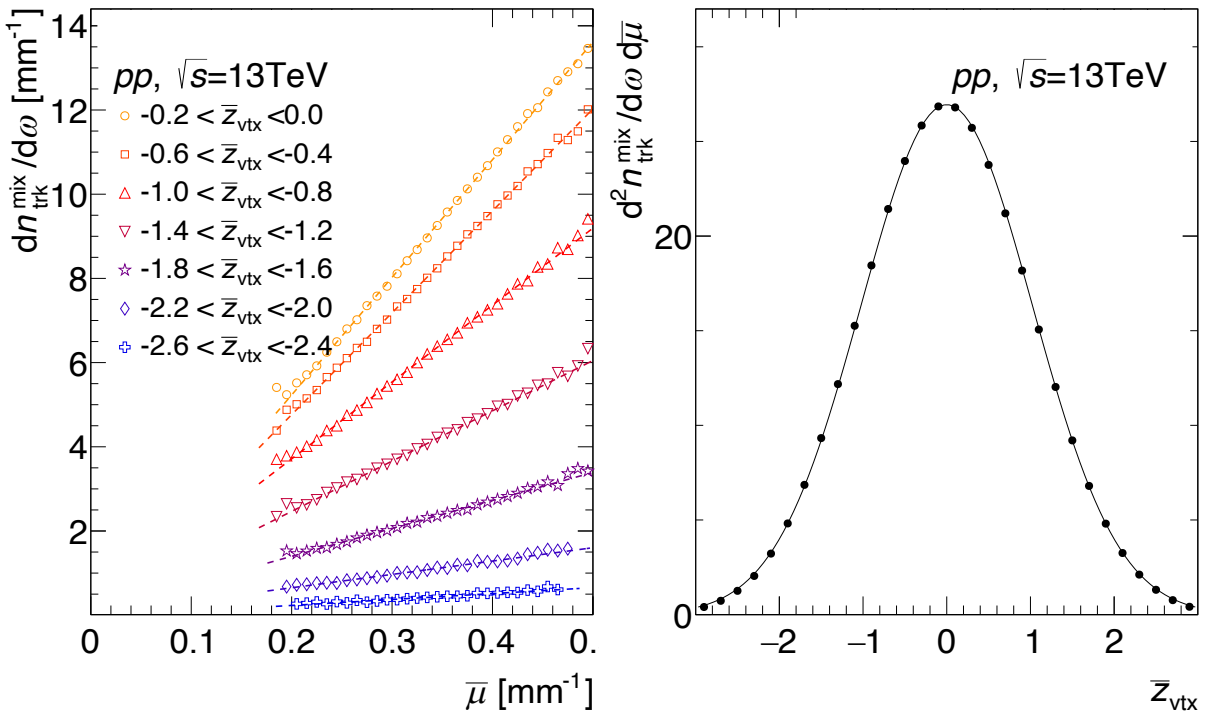

Figure 22: The number of tracks per mm at $\omega = 0$ is shown as a function of $\bar{\mu}$ (left panel). Different marker colors correspond to selected reduced z_{vtx} intervals. Dashed lines are fits assuming scaling of track density with $\bar{\mu}$. Slopes of the fits shown in the left panel are fitted to a Gaussian shape as a function of $\bar{z}_{\text{vtx}}$ (right panel).

peak $\mathrm{d}^2 n_{\text{trk}}/\mathrm{d}\omega\mathrm{d}\bar{\mu}$ at $\bar{z}_{\text{vtx}} = 0$, extracted from the fit, is the parameter that contains the cross-section of the particle production into the fiducial acceptance of the ATLAS detector and is a constant. For practical reasons, this parameter is extracted for groups of runs that correspond to detector stability intervals as defined by the ATLAS QA. Values of $\langle z_{\text{vtx}} \rangle$ and RMS(z_{vtx}) are obtained from fitting the corresponding values like those shown in Figure 19 as a function of lumiblock number in intervals of stability worked out during recalibration procedure explained earlier.

The number of tracks in *Mixed* events is plotted in the left pane of Figure 23 for different values of ν. By construction, the shape of these distributions shall not depend on the value of z_{vtx} where those events occur. The right panel of the figure explicitly shows that the mean values of n_{ch} distributions in *Mixed* event sample are the same in all vertices. Dashed lines indicate the width of the ν intervals of 0.5 track used to obtain these distributions, the same as those used in the analysis.

Performance of the PU reconstruction procedure can be demonstrated with Figure 24

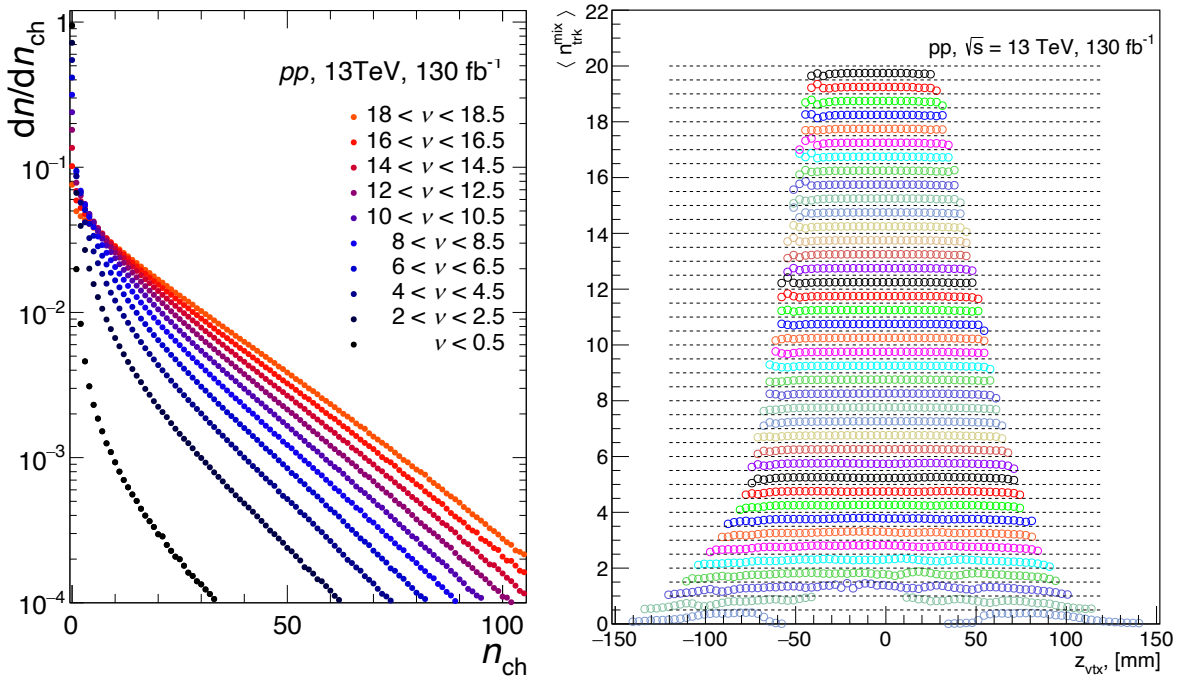

Figure 23: Left: number of tracks in *Mixed* events for different values of ν used in the analysis. Right: Average number of tracks in *Mixed* events, shown with different colors, as a function of event z_{vtx} for different ν. Dashed lines indicate the width of the ν selection for plotted curves.

that spans 589 runs recorded between 2015 and 2018. Although other factors affect the values plotted in the figure, the PU is the dominant contributor. The figure is obtained with an unprescaled single muon trigger in the invariant mass window of the dimuon corresponding to the Z boson. Red squares show the average number of charged particle tracks compatible with the trigger vertex. The largest contribution to this number comes from the event component that fired the trigger, and it remains constant, but the PU-induced contribution changes run-by-run and generally increases from the beginning to the end of the run as the LHC luminosity increases with time since the beginning of the Run-2. The number of tracks that are not compatible with the trigger vertex, i.e., coming from the PU, remains constant when this number is divided by μ. This reflects the fact that the number of tracks per pp interaction is a physical quantity, and as it shown with blue diamonds in the figure, the ATLAS detector measures it as an invariant number.

The average number of PU tracks estimated by Equation (8) is shown with magenta squares. It changes run-by-run and generally grows with time since the beginning of the

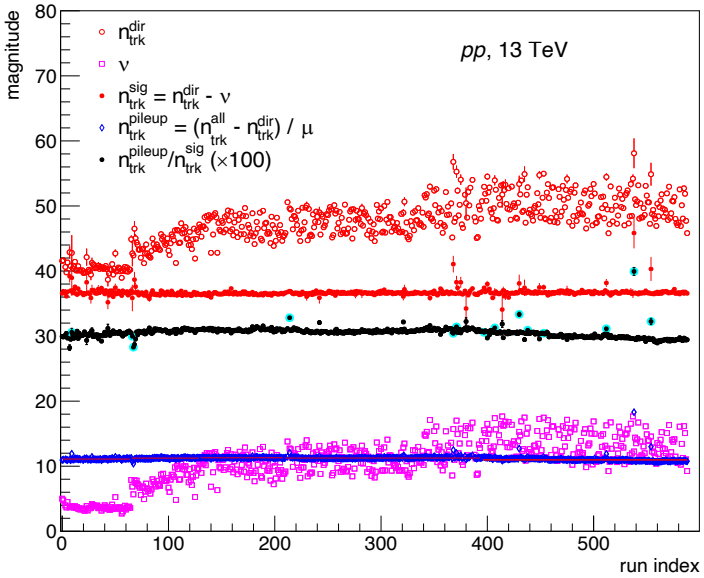

Figure 24: Number of direct (red open circles), mixed (magenta open squares), signal (red circles), pileup (blue diamonds) and ratio of pileup to signal (black circles) tracks as a function of the run index.

run. The difference between the two curves shown with the red and magenta squares is the contribution of the tracks coming from the trigger vertex. Due to the presence of the Z boson in events, it is much larger than in the inclusive sample, and this number remains constant in most data runs. The black curve is an arbitrarily scaled ratio of the number of tracks in events with Z boson and inclusive events. This ratio is not very sensitive to the problems of acceptance but is sensitive to luminosity calibrations. A few outlying runs, highlighted with cyan circles, are also excluded from the analysis. Overall the figure demonstrates the sub-percent level detector stability and quality of the PU estimator throughout the entire run.

4.4 Event corrections

This analysis measures per-event quantities, such as the multiplicity distribution of charged particles in an event and their kinematic distributions. Nevertheless, accurate removal of the combinatorial background from that data sample, events that do not have Υ states but are combinations of muons coming from jets and the Drell-Yan, rely on fitting the invariant mass distribution of muon pairs. In the course of working on the analysis, it was observed that correcting the invariant mass spectra improves the quality and stability of

the fits. Therefore, the invariant mass spectra of dimuons, selected by applying cuts from Section 4.2, were corrected for losses before the fitting.

Several loss mechanisms are considered here.

- fiducial acceptance of the ATLAS detector to different $\Upsilon(n\mathrm{S})$ states.
- muon reconstruction efficiency to each of the muons.
- trigger efficiency.
- trigger prescale factors.
- quality assurance, both as performed by ATLAS and for PU removal.

In this analysis, event losses caused by the first and second mechanisms listed above are fully corrected. Trigger efficiency losses are corrected for low-threshold triggers, for which correction functions are worked out by ATLAS. Data samples obtained by the higher-threshold triggers are used only where triggers become fully efficient. Losses due to the last two mechanisms are not corrected as they do not affect signal extraction.

4.4.1 Fiducial acceptance

The fiducial acceptance for $\Upsilon \to \mu\mu$ decays is defined as the probability that the decay products fall within the fiducial volume, characterized by p_{T}^{μ} and η^{μ} thresholds, for a given transverse momentum and rapidity of an $\Upsilon(n\mathrm{S})$ state. The fiducial acceptance correction is evaluated from a fast MC simulation of $\Upsilon(n\mathrm{S})$ decays and applied as a weight to a dimuon pair with the corresponding reconstructed values of $p_{\mathrm{T}}^{\mu\mu}$ and $y^{\mu\mu}$ in 0.1 GeV-wide slices of $m^{\mu\mu}$. Fiducial acceptance that required $p_{\mathrm{T}}^{\mu} > 4$ GeV implies that above 4 GeV muons are reconstructed. This is not the case for higher triggers used in the analysis, which start measuring muons from much higher values. For them, the fiducial acceptance is redefined, see Figure 25, with the higher momentum of the muon corresponding to its nominal value in the trigger.

4.4.2 Muon reconstruction efficiency

The factors determining whether the ATLAS detector reconstructs the Υ meson are fiducial acceptance, muon reconstruction efficiency, and di-muon trigger efficiency. The muon reconstruction efficiencies and di-muon trigger efficiencies are obtained using simulated

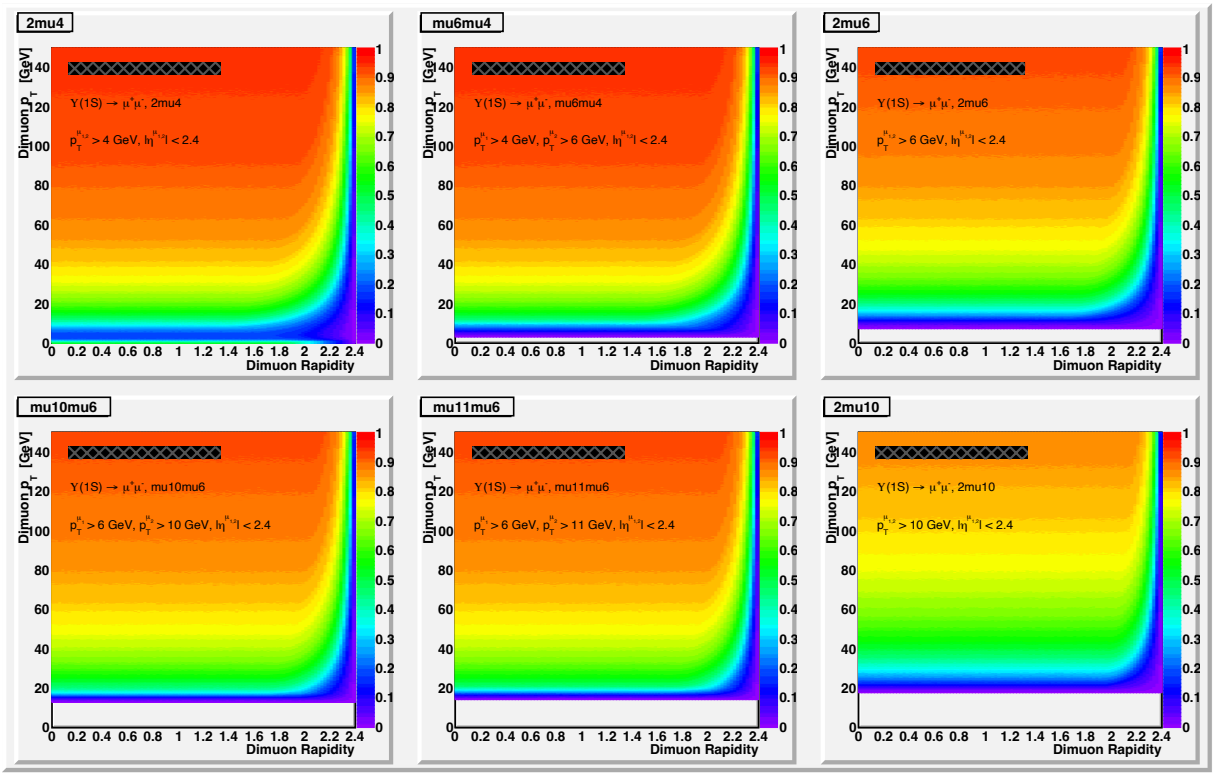

Figure 25: $\Upsilon(1S)$ fiducial acceptance for triggers used in the analysis.

events. The muon reconstruction efficiency is defined as the product of the probability of a muon reconstructed as an ID track also to be reconstructed in the MS and the probability that a muon is reconstructed as an ID track [81]. The latter cannot be measured directly and is replaced by the conditional probability that a muon reconstructed by the MS is also reconstructed by the ID independently

$$\epsilon(\mu) = \epsilon(\mu|ID)\epsilon(ID) \approx \epsilon(\mu|ID)\epsilon(ID|MS) \tag{9}$$

where $\epsilon(\mu|ID)$ is the efficiency of muons reconstructed as ID tracks to be reconstructed in the MS, $\epsilon(ID)$ is the probability that a muon is reconstructed as an ID track, and $\epsilon(ID|MS)$ is the conditional probability that a muon reconstructed by the MS is also reconstructed by the ID independently. To cover possible differences between data and simulation, the efficiency values calculated in the simulation are corrected by scale factors which are the ratios of measured and simulated efficiencies obtained using the tag-and-probe (TnP) method [81, 86] - a well-established data-driven procedure of evaluating detector performance by using the information redundancy of various subsystems. The method selects a sample of high-purity leptons coming from a resonance decay by applying strict selection on one of the decay products (*tag*) and on the invariant mass of the

pair involving this lepton and the second particle (*probe*) traced from only a part of the detector. This ensures that the probe is also a lepton, even without identifying it as such in the detector. This opens the possibility of measuring the properties of the selected probe in all subsystems of the detector by changing the definition of the probe particle. By applying conservative selection criteria on the quality of the tag and the properties of the resonance decay, one can reach a high purity of the probe particle sample. Then, the TnP method is applied independently to data and simulation, making possible the construction of scale factors from the evaluated efficiencies. The 2D reconstruction efficiency map used to correct the *pp* data is shown in Figure 26.

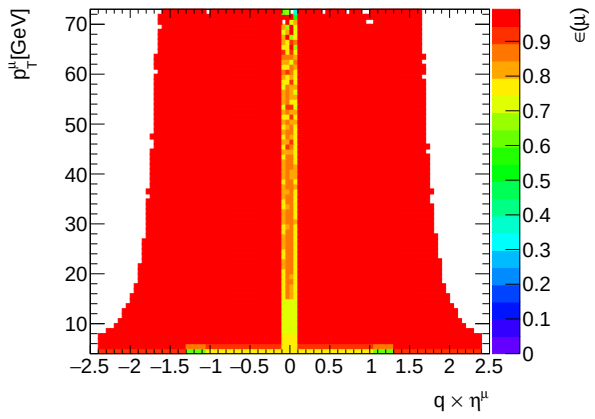

Figure 26: Muon reconstruction efficiency map for tight muons obtained from 2015-2018 *pp* data

4.4.3 Trigger efficiency

The trigger inefficiency for a di-muon pair factorizes as the product of the two single-muon trigger efficiencies, a term which depends on the distance between two muons, and a term that accounts for the loss due to online cuts applied to a pair, such as on the invariant mass, vertex fit quality, etc. [87]. For symmetric triggers HLT_2mu(j)_bUpsimumu... listed in Table 2, for example, HLT_2mu4_bUpsimumu, trigger efficiency can be considered in a factorized form

$$\epsilon_{\text{trig}}^{2\text{mu}(j)}\left(\mu_1,\mu_2\right) = \epsilon\left(\text{mu}(j),\mu_1\right)\epsilon\left(\text{mu}(j),\mu_2\right)C_{\Delta R}\left(\mu_1,\mu_2\right)C_a\left(y^{\mu\mu},\tau\right) \tag{10}$$

where j is the energy threshold, $\epsilon\left(\text{mu}(j),\mu_i\right)$ is the efficiency of HLT_mu(j) single muon trigger with respect to the reconstructed muon, $C_{\Delta R}\left(\mu_1,\mu_2\right)$ is a dimuon correction which

depends on the distance ΔR between two muons, $C_a\left(y^{\mu\mu},\tau\right)$ is the correlation factor aiming to recover the event loss due to online cuts applied to a pair such as cut on the invariant mass, vertex fit quality. The two single muon efficiency terms become strongly correlated in the case when both muons are contained in the same region of interest (ROI) since the efficiency of the dimuon chain should be 0 if only a single ROI has been formed. For asymmetric triggers HLT_mu(j)mu(k)_bUpsimumu... listed in Table 2, for example HLT_mu6mu4_bUpsimumu, an additional complication should be used

$$\epsilon_{\text{trig}}^{\text{mu}(j)\text{mu}(k),j>k}\left(\mu_1,\mu_2\right)=\begin{pmatrix}\epsilon\left(\text{mu}(j),\mu_1\right)\epsilon\left(\text{mu}(k),\mu_2\right)+\\ \epsilon\left(\text{mu}(k),\mu_1\right)\epsilon\left(\text{mu}(j),\mu_2\right)-\\ \epsilon\left(\text{mu}(j),\mu_1\right)\epsilon\left(\text{mu}(j),\mu_2\right)\end{pmatrix}C_{\Delta R}\left(\mu_1,\mu_2\right)C_a\left(y^{\mu\mu},\tau\right). \quad (11)$$

The efficiencies are obtained from MC simulation and are corrected by the corresponding scale factors. Figure 27 shows 2D maps of the trigger efficiencies for the three lowest dimuon triggers 2mu4, mu6mu4, and 2mu6 used in the analysis.

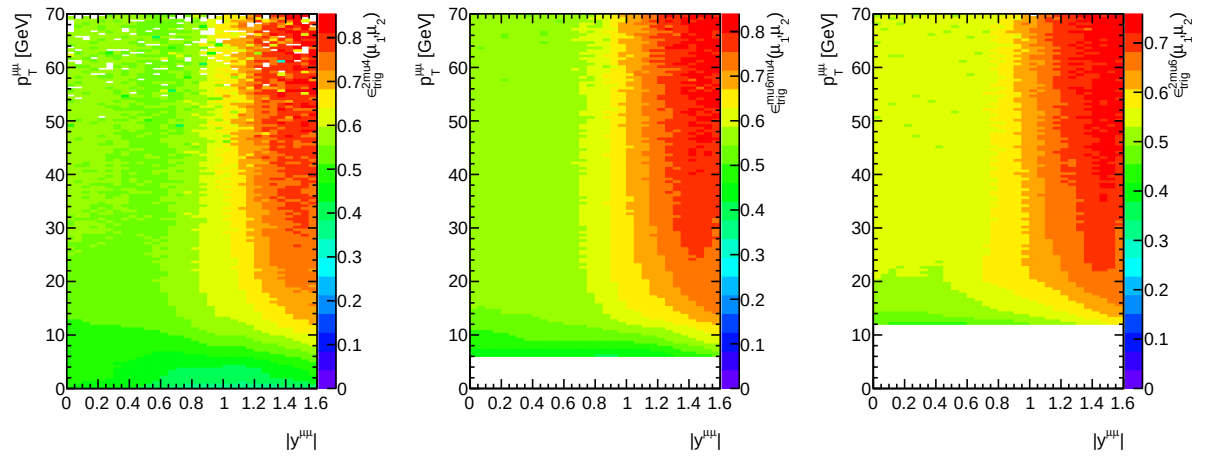

Figure 27: Dimuon trigger efficiency maps for 2mu4 (left), mu6mu4(middle) and 2mu6(right) which are averaged over trigger weights in the data sample

4.4.4 Total correction

The total event-based correction is

$$\omega_{\text{tot}}^{\text{evt}}=\frac{1}{acc\left(p_{\text{T}}^{\mu\mu},y^{\mu\mu}\right)\cdot\epsilon\left(p_{\text{T}}^{\mu_1},\eta^{\mu_1}\right)\cdot\epsilon\left(p_{\text{T}}^{\mu_2},\eta^{\mu_2}\right)\cdot\epsilon_{trig}\left(\mu_1,\mu_2\right)} \quad (12)$$

The analysis measures per-event quantities and uses data from each trigger separately; therefore, trigger prescale values play no role in the results and are not part of the cor-

rection. The effect of applied corrections is shown in Figure 28. Black markers show the dimuon mass spectra corrected by only muon reconstruction efficiencies. When we add correction for trigger efficiencies, we get the spectra shown with red markers. The fully

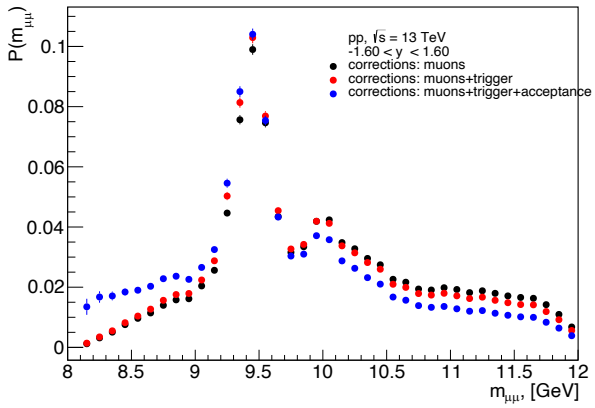

Figure 28: Transformation of the shape of the dimuon invariant mass distribution. Black markers show the distribution after applying muon reconstruction efficiency correction, red also includes corrections for trigger efficiencies, and blue, in addition to the previous two, takes into account fiducial acceptance correction.

corrected distribution is shown in Figure 28 with blue markers. Neither trigger correction, nor the fiducial one, visibly changes the Υ peaks; however, they flatten the combinatorial background, especially in the low mass region in lower p_{T} bins, which makes the fitting procedure more stable.

4.5 Corrections for charged particle tracks

4.5.1 General approach

Correcting tracks reconstructed in the detector to the number of primary charged particles produced in the collisions considers several aspects.

- definition of primary changed particles, secondary particles, and fakes.
- detector efficiency, including the efficiency of the reconstruction algorithm and its variation with the event geometry, kinematics, detector occupancy, and detector stability.

The primary charged particle definition used here is almost the same as is used in earlier ATLAS publication [88]. Primary charged particles are defined as particles with average

lifetime $\tau > 0.3 \times 10^{-10}$s and produced directly in the interaction or those from decays of particles with a shorter lifetime. According to this definition, however, muons coming from Υ decays are also considered primary charged particles, but in this analysis, they are excluded for an obvious reason. All final results are corrected to the numbers of n_{ch} that is the number of primary charged particles in the kinematic range $0.5 < p_{\mathrm{T}} < 10$ GeV and $|\eta| < 2.5$.

For the second item listed above, corrections implemented in the analysis take into account the kinematic properties of the tracks and locations of the event vertices. Issues related to detector occupancy and detector stability are treated differently. Data used in the analysis were accumulated over four years, during which time the instantaneous luminosity of the LHC was steadily increasing. For that reason untangling the effects of occupancy and stability in the detector performance is not always possible. In addition, final results also require subtraction of the PU, which in turn, is a factor directly sensitive to the detector occupancy. Except for the PU correction, which has a non-linear component discussed in Section 4.6.5, all other effects are smaller than the systematic uncertainties and are included in the systematic of the PU subtraction. In this section, we discuss correcting n_{ch} for the losses in the detector.

The general approach to the track-based correction used in this analysis is to calculate the weight for each track. Events in which no track is found are accepted to the analysis with $n_{\mathrm{ch}} = 0$. For each reconstructed track, the weight is defined by two factors that depend on the track kinematics and its point of origin: 1) track reconstruction efficiency $\epsilon^{\mathrm{trk}}(p_{\mathrm{T}}, \eta, z_{\mathrm{vtx}})$ and 2) fraction of secondary tracks $frac(p_{\mathrm{T}}, \eta)$ in the sample. Once the combined efficiency $p^{\mathrm{trk}}(p_{\mathrm{T}}, \eta, z_{\mathrm{vtx}}) = \epsilon^{\mathrm{trk}}(p_{\mathrm{T}}, \eta, z_{\mathrm{vtx}}) / frac(p_{\mathrm{T}}, \eta)$ is determined, the track is accepted to the analysis with the weight, n, which is not equal to $1/p^{\mathrm{trk}}$ but is an integer number randomly picked according to the Negative Binomial Distribution (NBD) which is a discrete probability distribution that models the number of failures in a sequence of independent and identically distributed Bernoulli trials before a specified number of successes occurs:

$$P(n; p, r) = \binom{n-1}{r-1} p^r (1-p)^{n-r} \tag{13}$$

where r is the number of successes, n is the number of trials, and p is the probability of a successful Bernoulli trial.

In our case, the evaluation is done for each reconstructed track so that $r = 1$, then

$$P\left(n; r, p^{\mathrm{trk}}\left(p_{\mathrm{T}}, \eta, z_{\mathrm{vtx}}\right)\right) = p^{\mathrm{trk}}\left(p_{\mathrm{T}}, \eta, z_{\mathrm{vtx}}\right)\left(1 - p^{\mathrm{trk}}\left(p_{\mathrm{T}}, \eta, z_{\mathrm{vtx}}\right)\right)^{n-1} \tag{14}$$

The advantage of using integer weights instead of just dividing each track by its efficiency can be seen with the example of *Mixed* event distributions. *Mixed* events that used for the PU correction are worked out from tracks in *Direct* events after calculating the efficiency. n_{ch} distributions shown in Figure 29.

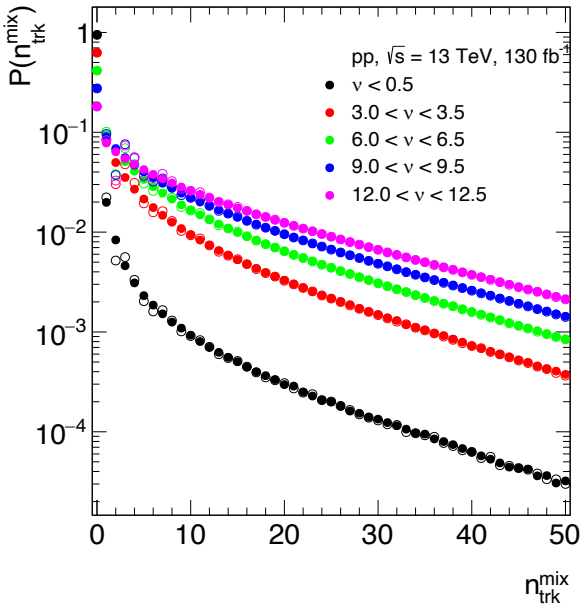

Figure 29: n_{ch} distributions in *Mixed* events in intervals of ν. Open markers use weights equal to $1/p^{\mathrm{trk}}$ and full markers use weights derived from the NBD.

Open markers show n_{ch} distributions obtained by weighting each track with inverse efficiency, and full markers are distributions obtained using weighting based on the NBD. At the high end, the distributions are identical, but at low n_{ch} the NBD produces smoother and more realistic results.

4.5.2 Fraction of non-primary particles

In many analyses, correction for the secondary (non-primary) tracks is combined with the fake track correction. In this analysis, they are treated separately. The fraction of fake tracks present in a *pp* event without PU is very small and generally can be neglected [89]. The situation changes when the PU increases, and fake production may grow due to

increasing occupancy in the detector. This is the non-linear track production mechanism that was discussed at the beginning of Section 4.3, and its correction will be explained later in Section 4.6. Here only correction for secondary tracks is discussed. The main contribution to secondary tracks comes from decays of strange mesons and baryons. A detailed discussion about the contribution of strange baryons can be found in Ref. [88], but it primarily relates to the p_{T} regions higher than are considered in this analysis. Correction for secondary particles is applied differentially in p_{T} and η. The primary fraction is calculated as follows

$$frac\left(p_{\mathrm{T}}, \eta\right) = \frac{N_{\mathrm{rec}}^{\mathrm{prim}}\left(p_{\mathrm{T}}, \eta\right)}{N_{\mathrm{rec}}^{\mathrm{all}}\left(p_{\mathrm{T}}, \eta\right)} \tag{15}$$

where $N_{\mathrm{rec}}^{\mathrm{prim}}$ is the number of reconstructed tracks matched to primary and $N_{\mathrm{rec}}^{\mathrm{all}}$ is the number of all reconstructed tracks.

The fraction of secondary tracks and strange baryons are shown in the left panel of Fig. 30. To apply it, the correction is parametrized by a second-degree polynomial function, as shown in the right panel of Fig. 30.

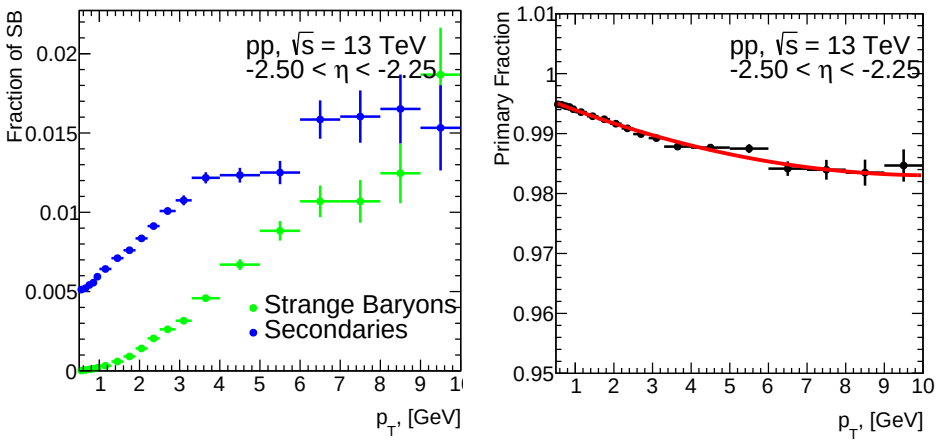

Figure 30: Left: Fractions of secondary tracks (blue) and strange baryons (green). Right: Fraction of primary particles.

4.5.3 Track reconstruction efficiency

Track reconstruction efficiency used in this analysis is defined as the number of reconstructed primary tracks divided by the number of generated primary particles in nominal

acceptance

$$\epsilon^{\mathrm{trk}} = \frac{N_{\mathrm{rec}}^{\mathrm{prim}}}{N_{\mathrm{gen}}} \tag{16}$$

where reconstructed and generated quantities are defined in their variable space $(p_{\mathrm{T}}^{\mathrm{rec}}, \eta^{\mathrm{rec}})$ and $(p_{\mathrm{T}}^{\mathrm{gen}}, \eta^{\mathrm{gen}})$ respectively. Defined this way, the efficiency absorbs into itself the bin-by-bin unfolding correction for the Inner Detector tracking system resolution, which has limited accuracy. However, in the kinematic region explored in the present analysis, the ID tracking system efficiency and resolutions are sufficiently high not to affect the results [90].

The PU removal procedure described in Section 4.3 relies on the uniformity of the detector response to the collision vertex. Therefore, in addition to the dependence on track kinematics, the efficiency has also been studied as a function of event (track) point of origin: $\epsilon^{\mathrm{trk}}(p_{\mathrm{T}}, \eta, z_{\mathrm{vtx}})$. In this analysis, it is assumed that the track reconstruction efficiency factorizes as follows.

$$\epsilon^{\mathrm{trk}}(p_{\mathrm{T}}, \eta, z_{\mathrm{vtx}}) = f(\eta, p_{\mathrm{T}})\, k(\eta, z_{\mathrm{vtx}})\, \epsilon^{\mathrm{trk}}(p_{\mathrm{T}}) \tag{17}$$

where the last term is a generic p_{T}-dependence of reconstruction efficiency, f and k are "tuning" functions for η and z_{vtx} dependencies respectively. The shape of the $\epsilon^{\mathrm{trk}}(p_{\mathrm{T}}) = \langle \epsilon^{\mathrm{trk}}(p_{\mathrm{T}}, \eta, z_{\mathrm{vtx}}) \rangle$ averaged over η and z_{vtx} is shown in the left panel of Fig. 31. It is used

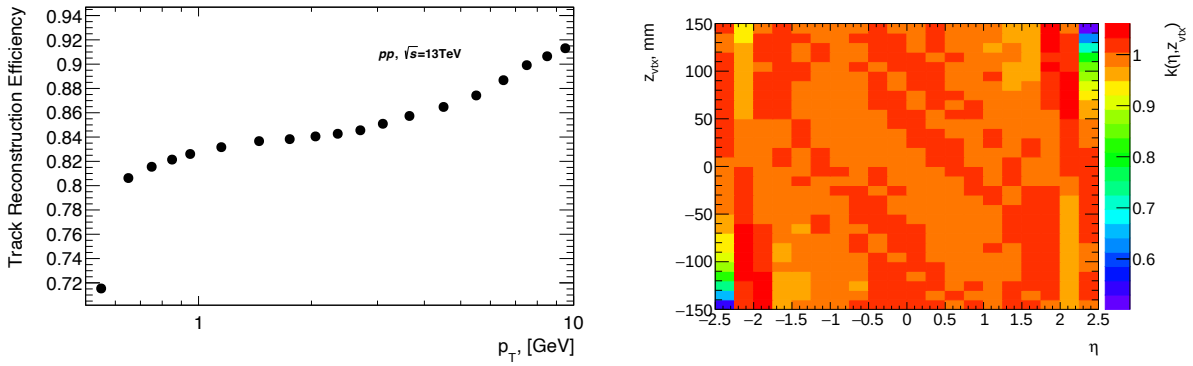

Figure 31: Left: p_{T}-dependence of the track reconstruction efficiency. Right: 2D map of the $k(\eta, z_{\mathrm{vtx}})$.

as the last term in Equation (17).

The z_{vtx} dependence given by the function $k(\eta, z_{\mathrm{vtx}})$ is worked out as the 2D lookup table of the values at a given vertex position and pseudorapidity to a globally averaged value. This map is shown in the right panel of Figure 31. At the edges of the z_{vtx} distribution, the η profile of the track reconstruction efficiency gains about 30% asymmetry.

For the sake of the acceptance uniformity and to keep corrections low, further analysis is restricted to $|z_{\mathrm{vtx}}| < 140$ mm on an event selection level.

Function $f\left(p_{\mathrm{T}}, \eta\right)$ is chosen in the form

$$f\left(p_{\mathrm{T}}, \eta\right) = \alpha\left(\eta\right)\left[1 - \beta\left(\eta\right)\exp\left(-\frac{p_{\mathrm{T}}}{p_{\mathrm{T}_1}\left(\eta\right)}\right)\right]\left[1 + \frac{p_{\mathrm{T}}}{p_{\mathrm{T}_2}\left(\eta\right)}\right] \tag{18}$$

Parameter p_{T_1} is fixed to 0.1 GeV. It affects only the low-p_{T} part of the efficiency curve. Parameter p_{T_2} is of the order of hundreds of GeV and makes only a small change in the 10 GeV range. Other parameters have symmetric behavior, as shown in Fig. 32.

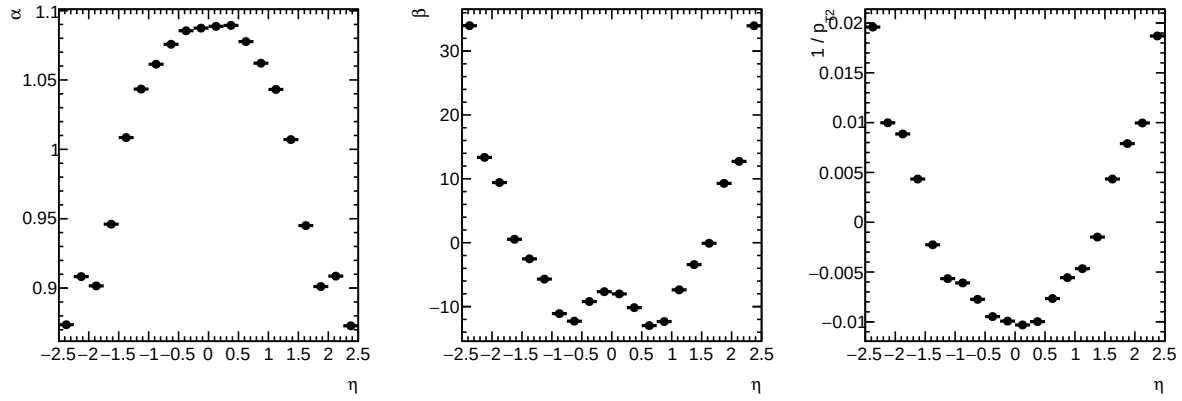

Figure 32: η-dependence of the fit parameters in $f\left(p_{\mathrm{T}}, \eta\right)$.

Some examples of $\epsilon^{\mathrm{trk}}\left(p_{\mathrm{T}}, \eta, z_{\mathrm{vtx}}\right)$ are shown in Figure 33 together with parameterizations given by Equation (17) which are actually used in calculating corrections. On average, the correction applied to a single track in the analysis is about 1.2 and never exceeds 2.5.

The performance of the tracking efficiency parameterization is shown in Figure 34. The plot compares the true level p_{T} distribution shown with red markers to fully corrected distributions after applying the procedure explained above. Each track passes the selection criteria as in Section 4.2 that suppresses the contribution of fakes and secondary particles. Each track is assigned the efficiency value worked out using parameterizations explained in Section 4.5.3. Then this efficiency is used to define weight as explained in Section 4.5.1. The weighted spectrum is plotted with black markers in the upper panel in Figure 34. The lower panel of Figure 34 shows the ratio of the two.

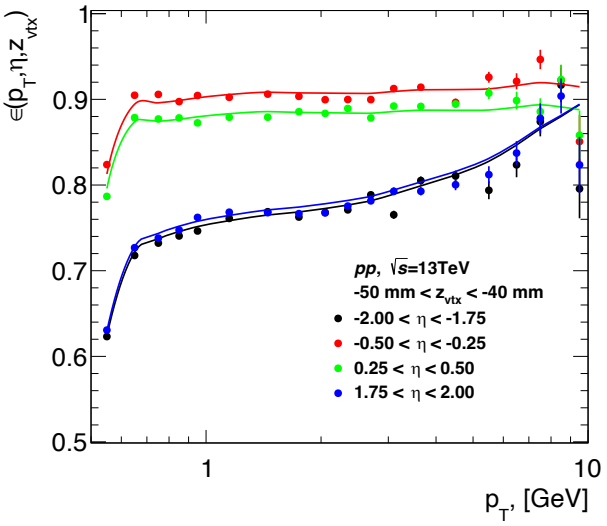

Figure 33: Track reconstruction efficiency $\epsilon^{\mathrm{trk}}(p_{\mathrm{T}}, \eta, z_{\mathrm{vtx}})$ from simulation (markers) and by parameterization (lines).

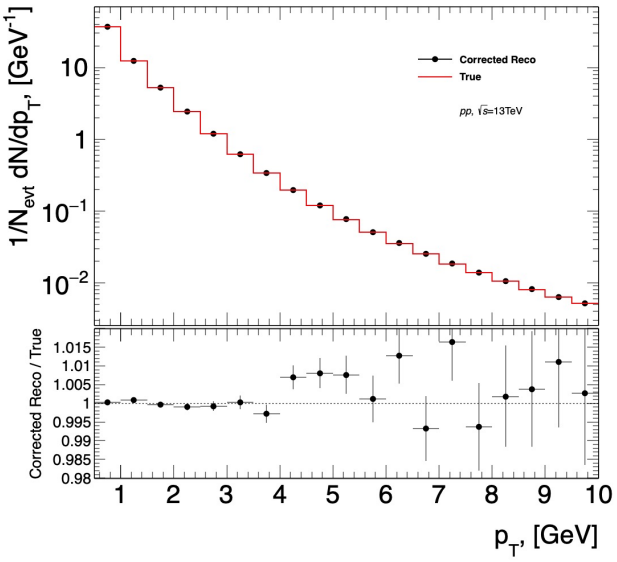

Figure 34: Tracking efficiency closure test.

4.6 Signal extraction

4.6.1 General approach

Multiplicity and kinematic distributions of hadrons coming from the event with Υ mesons can be measured in the data if one knows fractions of events that are coming from the signal (i.e., those that contain a particular $\Upsilon(n\mathrm{S})$ state) and from the background (spurious

association of muons from dijets and Drell-Yan). Such separation is typically done by measuring distributions of interest in several intervals of the muon pair invariant mass and performing linear transformation to separate signal contribution. This approach is often called the "shoulder subtraction method," and its version is used in this analysis. The key element to using this method is to define the partial contribution of events coming from different processes.

These contributions are obtained by fitting the invariant mass distribution $m^{\mu\mu}$ in slices of $p_{\mathrm{T}}^{\mu\mu}$. Steps that are necessary for constructing the invariant mass distributions are explained in Section 4.2 and Section 4.4. Since triggers used in the analysis have different thresholds, fits are performed independently for each trigger.

The resulting distributions would still contain tracks coming from the PU, which can be removed, as explained later. At the same time, the yields of $\Upsilon(n\mathrm{S})$ states only weakly depend on the PU. This fact is known from experience measuring dimuons in other analyses and in A+A collisions, in which efficiencies do not drop by more than a few percent even in the most central collisions [91]. For that reason, fits to $m^{\mu\mu}$ distributions are done for all PU conditions simultaneously, which greatly increases the statistics of the fitted samples.

As was already mentioned, data used in the analysis were accumulated over four years of detector operation, and different triggers were enabled in different data-taking periods in which average μ increased with time. It will not be surprising if some residual deviations are still present in the data with different ν (PU estimator, see Section 4.3) due to a simultaneous change of several different conditions. Nevertheless, fitting larger data samples gives an obvious advantage, and possible differences in signal extraction at different ν are considered as perturbations from common performance together with the systematics of the PU corrections.

The di-muon invariant mass distribution consists of signal peaks produced by the three meson states and a smooth background "substrate" produced by the association of muons in jets and by the Drell-Yan (DY) process. The measured distributions can be

approximated by the form

$$\begin{aligned} \text{fit}\,(m) &= \sum_{n\text{S}} N_{\Upsilon(n\text{S})} F_n(m) + N_{\text{bkg}} F_{\text{bkg}}(m) \\ F_n(m) &= (1-\omega_n) CB_n(m) + \omega_n G_n(m) \\ F_{\text{bkg}}(m) &= \sum_{i=0}^{3} a_i (m-m_0)^i; a_0 = 1 \end{aligned} \tag{19}$$

having signal contributions with the shape $F_n(m)$ and the background contributions $F_{\text{bkg}}(m)$. Coefficients $N_{\Upsilon(n\text{S})}$ are the yields of the $\Upsilon(n\text{S})$ states with n running from 1 to 3, and N_{bkg} is the background normalization coefficient. Following previous ATLAS analysis [92], the signal shape $F_{\text{bkg}}(m)$ is chosen as a sum of two contributions, one is the Crystal Ball p.d.f. (CB), and another is Gaussian p.d.f. (G), the coefficient ω is responsible for the relative contribution of these two p.d.f.'s. This shape is known to reproduce the shape of $\Upsilon(n\text{S})$ peaks with sufficiently high accuracy. The function F_{bkg}, which is responsible for the background, is the 3$^{\text{rd}}$ degree polynomial whose constant coefficient is set to unity. It is centered at $m_0 = 10$ GeV, which approximately corresponds to the center of the fitting region. This formulation gives the advantage of understanding the transformation of the background shape with the pair momentum, but one shall keep in mind that normalization coefficients have somewhat different meanings. $N_{\Upsilon(n\text{S})}$ are the integrated yields of mesons, while N_{bkg} is the background density per unit of $m^{\mu\mu}$.

The CB is a modification of the Gaussian function with the power-law tail at low masses that is intended to accommodate the effects of final-state radiation:

$$\begin{aligned} CB\,(m;\mu_0,\sigma,\alpha,p) &= N \cdot \begin{cases} \exp\left(-\frac{1}{2}\cdot\left[\frac{m-\mu_0}{\sigma}\right]^2\right), & \left[\frac{m-\mu_0}{\sigma}\right] > -\alpha \\ A\left(B - \left|\frac{m-\mu_0}{\sigma}\right|\right)^{-p}, & \left[\frac{m-\mu_0}{\sigma}\right] \le -\alpha \end{cases} \\ A &= \left(\frac{p}{|\alpha|}\right)^p \cdot \exp\left(-\frac{|\alpha|^2}{2}\right) \\ B &= \frac{p}{|\alpha|} - |\alpha| \\ N &= \frac{1}{\sigma\,(C+D)} \\ C &= \frac{p}{|\alpha|}\frac{1}{p-1}\exp\left(-\frac{|\alpha|^2}{2}\right) \\ D &= \sqrt{\frac{\pi}{2}}\left(1+\text{erf}\left(\frac{|\alpha|}{\sqrt{2}}\right)\right) \end{aligned} \tag{20}$$

Coefficients μ_0 and σ are the first and the second moments of the Gaussian part in the CB function, and two additional variables, commonly denoted p and α, are responsible

for the degree of the power-law tail and the point at which the function flips from the Gaussian to a power law. Term N and its components C and D are responsible for the normalization of the CB function.

For the shape of the signal peaks, alternative parameterizations were not tried in this study. However, one shall mention that $F_n(m)$ itself has much flexibility to assume different shapes, and those variations were studied in detail when addressing the systematic uncertainties. For the shape of the background, some analyses use more elaborate hypotheses; however, we found them over-defined. Even the 3$^{\text{rd}}$ degree polynomial, in many cases, does not produce a significant cubic term.

Fitting function to the invariant mass spectra as defined above has 25 parameters, where parameters are correlated with each other. Nevertheless, that much information cannot be extracted from an unconstrained direct fit to the data in each $p_{\text{T}}^{\mu\mu}$ interval. At the same time, parameters responsible for the shape of the signal and background can change from one $p_{\text{T}}^{\mu\mu}$ interval to another only slightly. Therefore, considering information about fitting parameters also from the adjacent intervals improves fitting quality. To take advantage of this fact, the yield extraction strategy performed in this analysis is implemented in the following steps:

- Fit the MC simulated distributions independently for each $\Upsilon(n\text{S})$ and constrain or fix parameters responsible for the shape of the peaks.
- Parametrize the $p_{\text{T}}^{\mu\mu}$ dependence of the fit parameters responsible for the shape
- Use parametrizations to fit the data, keeping peak amplitudes and substrate-free
- Invariant mass samples are fitted separately in intervals of $p_{\text{T}}^{\mu\mu}$ and for different triggers but combined for all UE and PU conditions.
- Relax shape parameters in the data one at a time and adjust $p_{\text{T}}^{\mu\mu}$ dependencies for those parameters that can be reliably extracted from the data
- Parametrize the substrate as a function of $p_{\text{T}}^{\mu\mu}$

4.6.2 Fits to the MC simulated samples

The parameter α is a nuisance parameter that can assume a relatively broad range of values. Here it is set to 1.3 standard deviations of the Gaussian part of the CB function

for each $\Upsilon(n\mathrm{S})$ state. After fixing the parameter α, the p_T-dependence of the widths is studied. Left panel of Figure 35 shows the p_T dependence of $\sigma_G^{1\mathrm{S}}$.

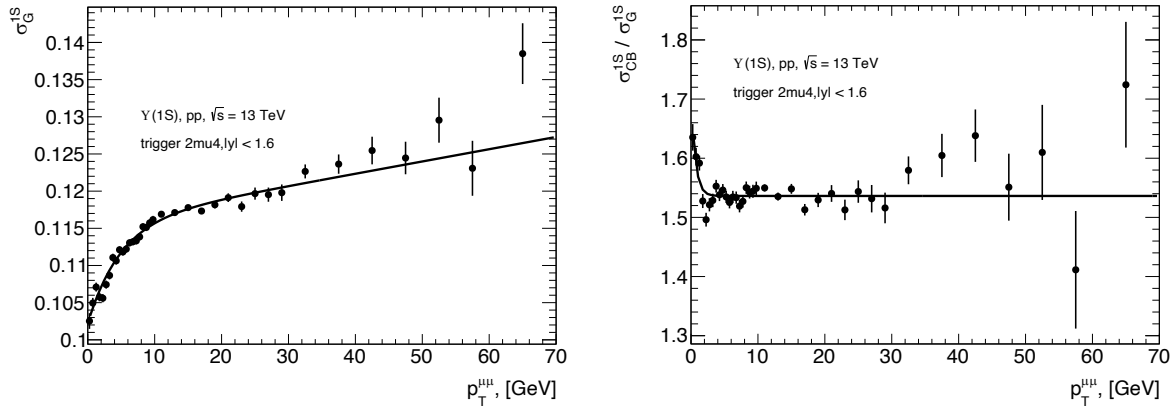

Figure 35: Left: p_T-dependence of the Gaussian width for $\Upsilon(1\mathrm{S})$. Right: p_T-dependence of the ratio of the width of CB function and the width of the Gaussian function.

Points are parametrized with the function

$$\sigma_G^{1\mathrm{S}}\left(p_\mathrm{T}^{\mu\mu}\right) = \left(c_0 + c_1 p_\mathrm{T}^{\mu\mu}\right) \cdot \left(1 - c_2 \exp\left(-\frac{p_\mathrm{T}^{\mu\mu}}{c_3}\right)\right) \tag{21}$$

The Gaussian width for higher $\Upsilon(n\mathrm{S})$ states is obtained by scaling $\sigma_G^{1\mathrm{S}}$ by the ratio of $m^{n\mathrm{S}}/m^{1\mathrm{S}}$ using mass values from the PDG [93].

The next parameter responsible for the shape of the peak is the width of the Gaussian part of the CB function $\sigma_{CB}^{n\mathrm{S}}$, which is closely related to the width of its pure-Gaussian counterpart. Therefore, instead of measuring this width, the measurement was done for the ratio of $\sigma_{CB}^{n\mathrm{S}}$ and $\sigma_G^{n\mathrm{S}}$. Its p_T dependence can be parametrized by

$$\frac{\sigma_{CB}^{nS}\left(p_\mathrm{T}^{\mu\mu}\right)}{\sigma_G^{nS}\left(p_\mathrm{T}^{\mu\mu}\right)} = c_0 + c_1 \exp\left(-\frac{p_\mathrm{T}^{\mu\mu}}{c_2}\right) \tag{22}$$

an example of which is shown in the right panel of Figure 35 for $\Upsilon(1\mathrm{S})$. The same functional form of the parametrization is used for all Υ states.

Parameter n is the degree of the power law tail, and it was found to be somewhat different for different $\Upsilon(n\mathrm{S})$ states. The p_T-parametrization function for this parameter is chosen as

$$n^{n\mathrm{S}}\left(p_\mathrm{T}^{\mu\mu}\right) = c_0 \left(p_\mathrm{T}^{\mu\mu}\right)^{c_3} \exp\left(-c_1 p_\mathrm{T}^{\mu\mu}\right) + c_2 \tag{23}$$

An example of such a parametrization is shown in the left panel in Fig. 36. Finally, the parameter ω, which balances the contributions of CB and G to the signal peaks, can also

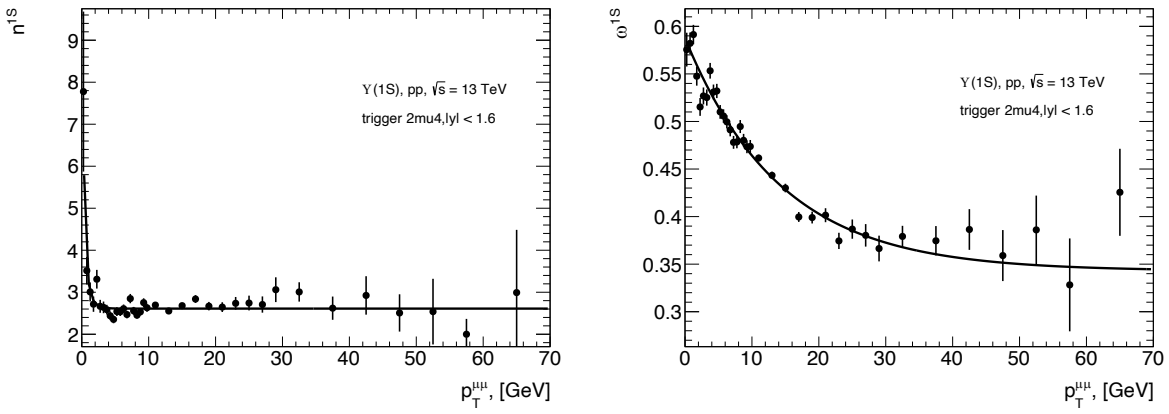

Figure 36: Left: p_{T}-dependence of the $n^{1\mathrm{S}}$ for $\Upsilon(1\mathrm{S})$. Right: p_{T}-dependence of the ratio of the $\omega^{1\mathrm{S}}$.

be slightly different for different $\Upsilon(n\mathrm{S})$ states and is parametrized with a third-degree polynomial function as is shown in the right panel of Figure 36 for 1S state. Parameters of m_0^{nS} are left unconstrained, but they are well-defined by the fits and produce values consistent with the PDG.

Examples of the fits to three $\Upsilon(n\mathrm{S})$ states in the MC simulations using all parameterizations are shown in Figure 37. Red lines are functions F_{nS}, shown together with its G component in green and CB component in blue. No background is present in the simulation; therefore, the polynomial part is absent. Furthermore, it was mentioned that fits are applied to the fully corrected data or simulations, but as explained in Section 4.4.1, each trigger measures $\Upsilon(n\mathrm{S})$ in a slightly different fiducial acceptance. For this reason, the results of the fits can be different for different triggers, as shown in the next section for the data. Small differences in fit parameters are also seen in the MC simulations that imply the triggers.

4.6.3 Fits to the data

Fits to all data in the analysis are done simultaneously for all triggers in all p_{T} bins. This produces hundreds of fits to histograms, some of which can fail or reach the limit of allowed values. The latter can indicate that the parameters are not constrained optimally. It can be seen in some plots shown in this section as points jumping outside statistical limits or as points with unreasonably large statistical error bars. Visual inspection of all fits is done during the optimization steps and for all final fits used in the analysis.

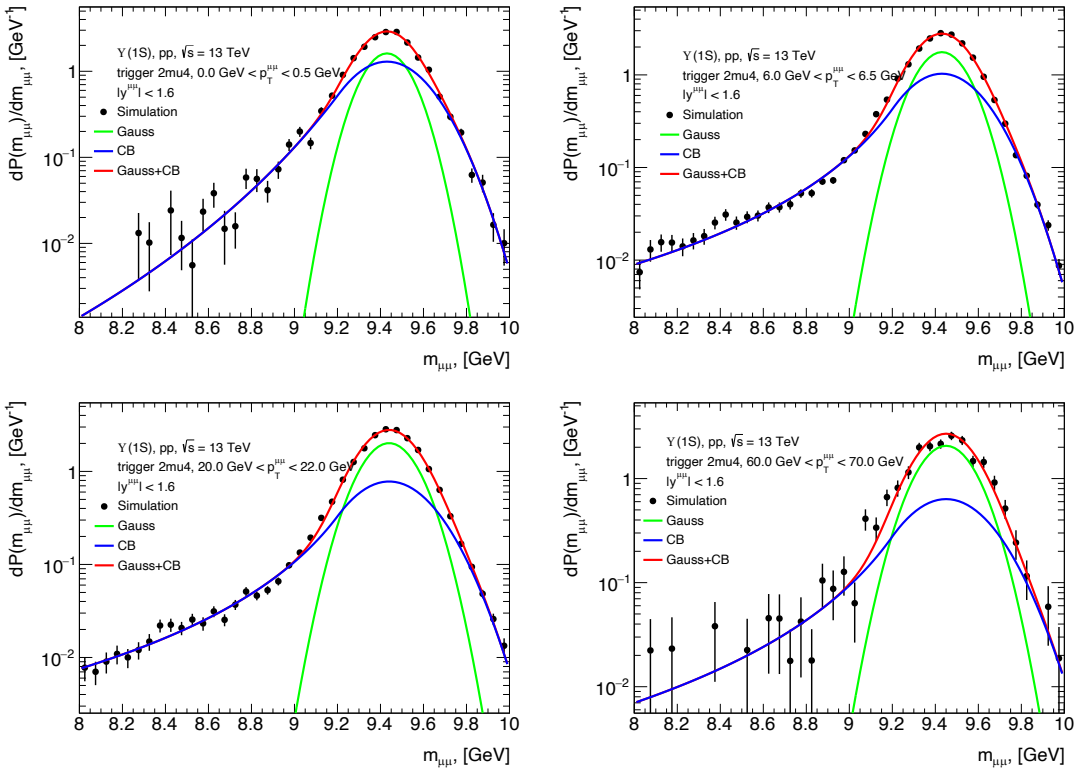

Figure 37: Examples of signal fits for $\Upsilon(1S)$ in different $p_{\mathrm{T}}^{\mu\mu}$ regions.

Some fit parameters can be extracted from the data with a reasonable confidence level, while it is impossible for others. For example, the degree of the power-law tail in CB part of the peaks mixes up with the substrate for $\Upsilon(1S)$, and for higher $\Upsilon(n\mathrm{S})$, the tail interferes with the neighboring peaks. Besides, parameters ω and n are correlated, so getting them directly from the data deems problematic. The MC parametrizations worked out, as explained in the previous section, are directly applied to the data. Some ideas about the behavior of $\omega^{1\mathrm{S}}$ can still be extracted from the data since the $\Upsilon(1S)$ is a relatively isolated, well-defined peak. However, extraction of the same parameters is problematic for $\Upsilon(3S)$ and certainly for $\Upsilon(2S)$ peaks. Where possible, the MC was verified against the data and found to be consistent with it.

Parameterization of $\sigma_G^{1\mathrm{S}}$ shown in Figure 35 is the starting value for the fitting of the data. The fit is constrained to be in the vicinity of the curve shown there but with the parameter unfixed. New parameterizations for $\sigma_G^{1\mathrm{S}}$ are found for each trigger separately, and they are used for further fits. Then the same approach is applied to the ratio $\sigma_{CB}^{1\mathrm{S}}/\sigma_G^{1\mathrm{S}}$, following which other parameters are inspected in a similar way and some refitted again. Final parameterizations are shown in Figure 38 together with unfixed points that are

fitted at the last step. Different markers represent different triggers, and lines show parametrizations. Results for the 2mu4 trigger are consistent with the parameterization obtained from the MC fits. Others also produce good new fits, which are different from MC parametrization due to differences in fiducial acceptance. The parametrizations are third-degree polynomial functions. After fixing σ_G^{1S}, parametrized to the data, the ratio

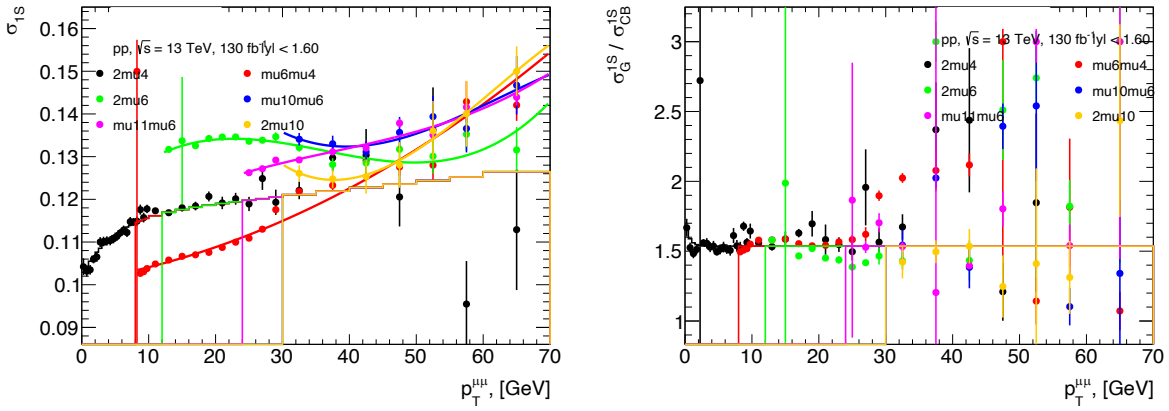

Figure 38: Shape parameters for the data as a function of $p_{\mathrm{T}}^{\mu\mu}$

of $\sigma_{CB}^{1S}/\sigma_G^{1S}$ is studied as a function of $p_{\mathrm{T}}^{\mu\mu}$. Right panel of Figure 38 shows that the data points are consistent with the parametrization, which in this case is the parameterization from the MC simulations.

Once the peak parameters are adjusted to the data or compared to it, the substrate fit values are also parametrized. This further stabilizes the fitting procedure. Substrate parameters a_n ($a_0 = 1$) are seen in Figure 39. Examples of the background parameterization function F_{bkg} for different $p_{\mathrm{T}}^{\mu\mu}$ regions and 2mu4 trigger are shown in the bottom right panel of Figure 39. Dynamics of the a_n coefficients shown in the plot correspond to the evolution of F_{bkg} shape shown in the lower-right panel of the Figure. The behavior of the lowest $p_{\mathrm{T}}^{\mu\mu}$ bin is explained by the lower acceptance in this region. Then, with increasing $p_{\mathrm{T}}^{\mu\mu}$ the F_{bkg} becomes monotonous and exhibits decreasing behavior with $m_{\mu\mu}$.

Yields of $\Upsilon(n\mathrm{S})$ and the background are shown in Figure 40. In the analysis, 2mu4 trigger is used from 0 p_{T}, mu6mu4 from 8 GeV and above, 2mu6 from 12 GeV, mu11mu6 from 24 GeV, and mu10mu6 and 2mu10 from 30 GeV. Numbers shown in the plots correspond to the fully corrected yields of $\Upsilon(n\mathrm{S})$ states for the signal and for the background N_{bkg} they are integrated in the mass region $8.2 < m^{\mu\mu} < 11.5$ GeV. Examples of final fits to 2mu4 trigger data are shown in Figure 41.

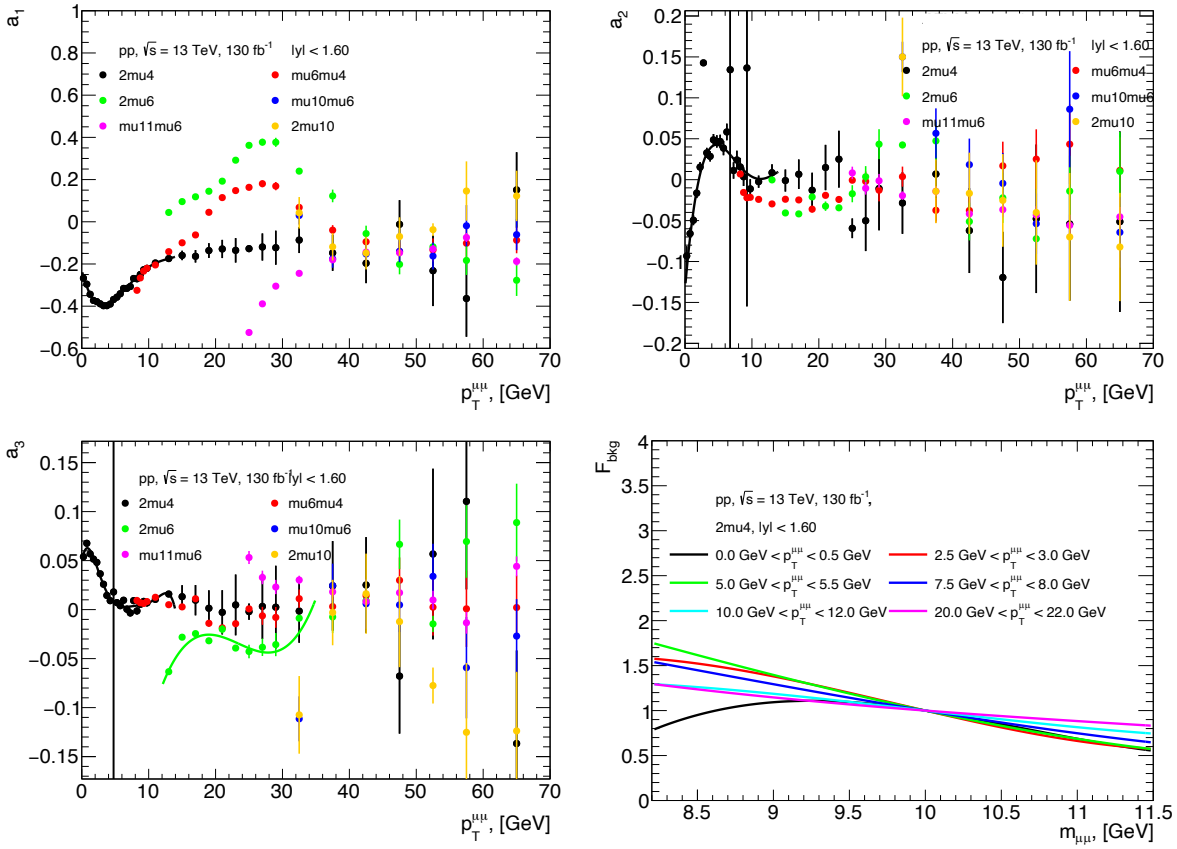

Figure 39: Parameters of the background parameterization as a function of $p_{\mathrm{T}}^{\mu\mu}$ (top left, top right and bottom left panels). Background parametrization (bottom right).

4.6.4 Shoulder subtraction method

Charged particle multiplicity and their kinematic distributions can be measured from the data by analyzing events in certain $m^{\mu\mu}$ intervals. In order to extract multiplicity distributions, one has to remove the combinatorial background. Distributions of charged particles, generally denoted as P, are measured in the data in 5 di-muon invariant mass intervals $[8.2, 9.0]$, $[9.1, 9.7]$, $[9.8, 10.1]$, $[10.2, 10.6]$, $[11.0, 11.5]$ given in units of GeV and denoted in the left panel of Figure 42 as $m_n^{\mu\mu}$, where $n = 0 - 4$. Distributions in the lower and upper intervals $P(m_0^{\mu\mu})$ and $P(m_4^{\mu\mu})$ are dominated by background, and the three middle intervals have significant contributions coming from one of the $\Upsilon(n\mathrm{S})$ states. Several examples of $P(m_n^{\mu\mu})$ measured for n_{ch} are shown in the right panel of Figure 42 with open markers.

Fits shown in the left panel of Figure 42 allow determining signal and background contributions in the intervals $n = 0 - 4$ to disentangle distributions associated with

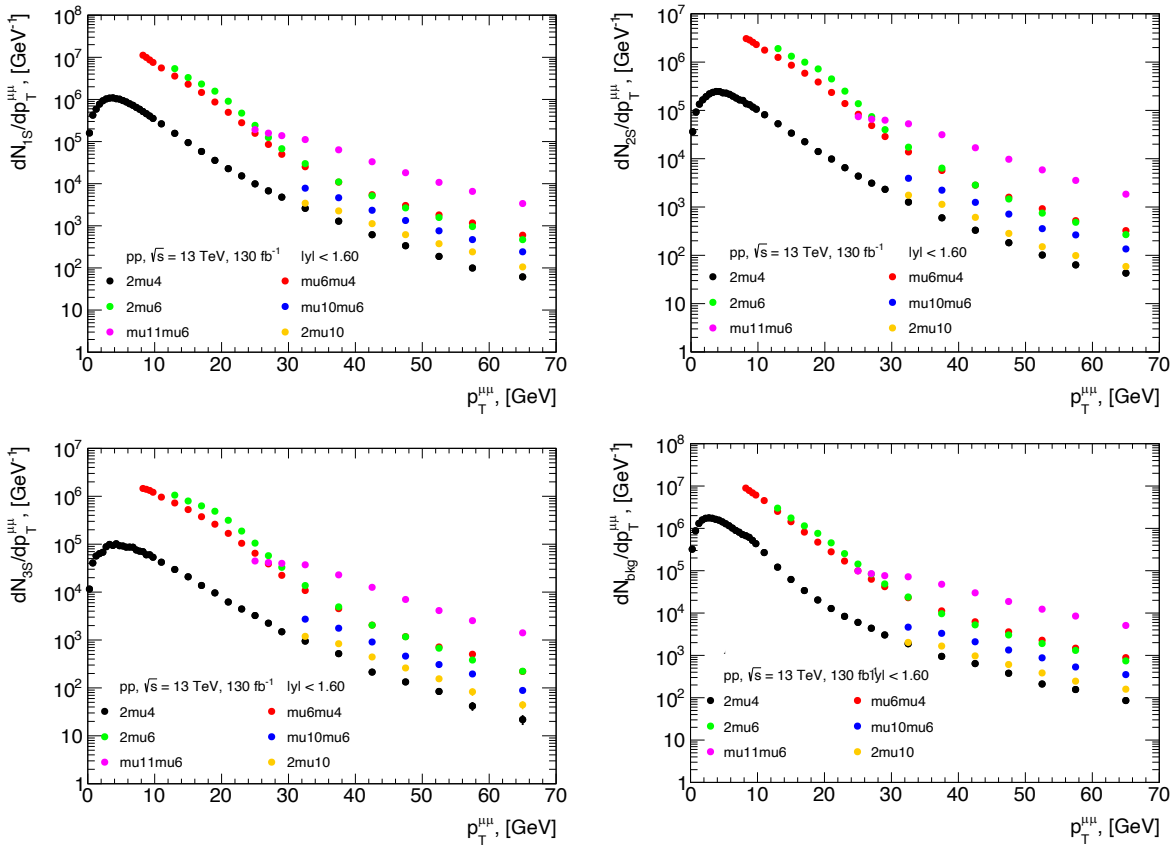

Figure 40: Yields of $\Upsilon(n\mathrm{S})$ and the background as a function of $p_{\mathrm{T}}^{\mu\mu}$. Background yield is integrated in the mass region $8.2 < m^{\mu\mu} < 11.5$ GeV.

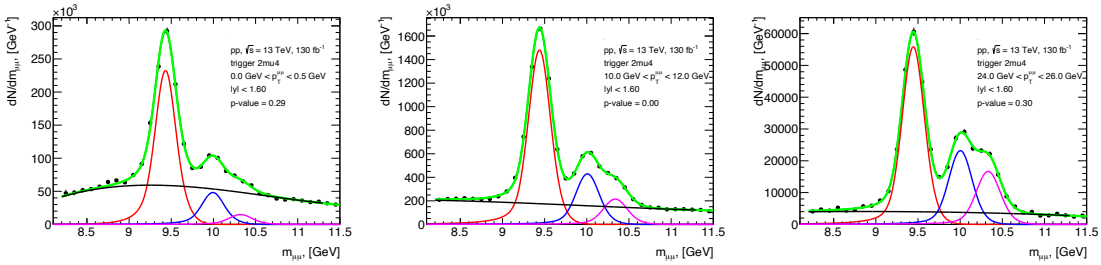

Figure 41: Examples of dimuon mass spectra fits for 2mu4 trigger.

different $\Upsilon(n\mathrm{S})$ states. Charged particle distributions coming from collisions with $\Upsilon(n\mathrm{S})$ in the mass intervals $m_k^{\mu\mu}$ with $n = k$ are denoted as s_n and contributions in the intervals $n \neq k$ as f_{nk}, they are calculated according to Equation (24).

$$
\begin{aligned}
s_n &= \frac{\int_{m_n^{\mu\mu}} N_{\Upsilon(n\mathrm{S})} F_n(m)\, dm}{\int_{m_n^{\mu\mu}} \mathrm{fit}(m)\, dm} \\
f_{nk} &= \frac{\int_{m_n^{\mu\mu}} N_{\Upsilon(k\mathrm{S})} F_k(m)\, dm}{\int_{m_n^{\mu\mu}} \mathrm{fit}(m)\, dm}
\end{aligned}
\tag{24}
$$

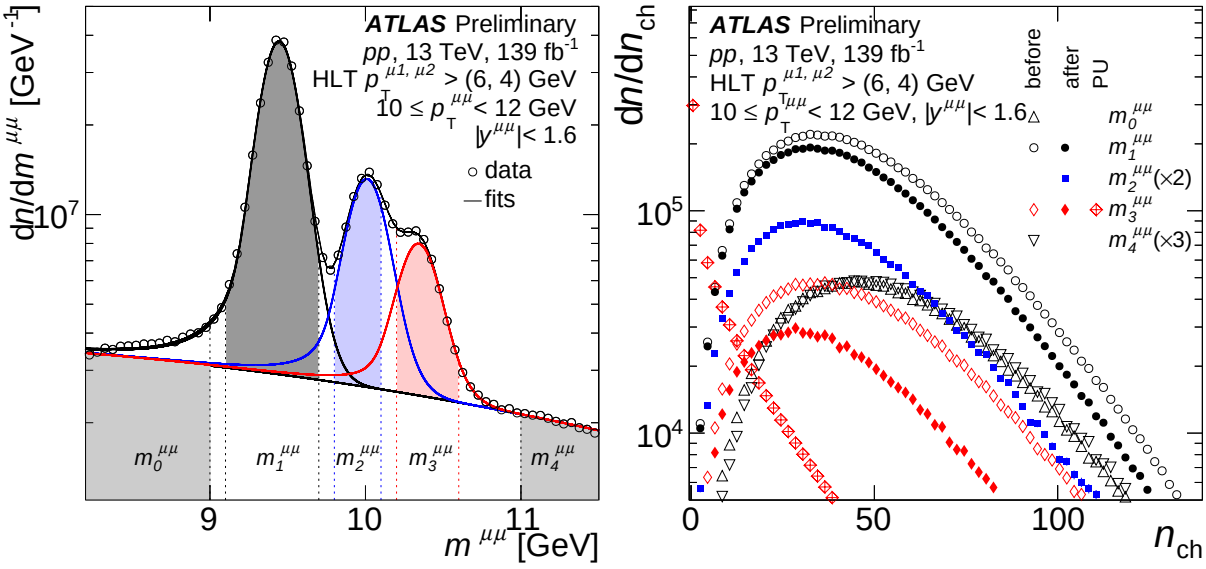

Figure 42: Left: Invariant mass distribution measured in the data in a $10 \leq p_{\mathrm{T}}^{\mu\mu} < 12$ GeV interval of the di-muon pair, fitted to the function used for extracting $\Upsilon(n\mathrm{S})$ yields. Indices $0-4$ denote $m^{\mu\mu}$ intervals used in the analysis. Right: Several n_{ch} distributions measured in the mass intervals indicated in the left panel. Open markers are distributions before subtracting the background are shown for four $m^{\mu\mu}$ intervals out of 5. Full markers are distributions after subtracting the background are shown for three mass intervals. Hatched markers indicate n_{ch} distribution coming from the PU that is measured in $m_3^{\mu\mu}$. PU distributions have the same shape in all intervals.

To assess the background contribution underneath the $\Upsilon(n\mathrm{S})$ peaks, the side-band subtraction method [94] is used. The contribution of the background in the n-th mass interval is taken as a weighted sum $k_n P_0 + (1 - k_n) P_4$ of the background distributions in mass intervals $m_0^{\mu\mu}$ and $m_4^{\mu\mu}$. Coefficient k_n is calculated according to Equation (25).

$$k_n = \frac{\langle F_{\mathrm{bkg}}(m)\rangle|_{m_4^{\mu\mu}} - \langle F_{\mathrm{bkg}}(m)\rangle|_{m_n^{\mu\mu}}}{\langle F_{\mathrm{bkg}}(m)\rangle|_{m_4^{\mu\mu}} - \langle F_{\mathrm{bkg}}(m)\rangle|_{m_0^{\mu\mu}}} \tag{25}$$

Thus $P(m_n^{\mu\mu})$ distributions measured in 5 mass intervals can be presented in the form of a matrix that links them to the contributions coming from $\Upsilon(n\mathrm{S})$ collisions as well as from the background in the low- and high-mass background intervals. This is given by

Equation (26).

$$\begin{pmatrix} P(m_0^{\mu\mu}) \\ P(m_1^{\mu\mu}) \\ P(m_2^{\mu\mu}) \\ P(m_3^{\mu\mu}) \\ P(m_4^{\mu\mu}) \end{pmatrix} = \begin{pmatrix} 1-f_{01} & f_{01} & 0 & 0 & 0 \\ k_1\,(1-s_1) & s_1 & 0 & 0 & (1-k_1)\,(1-s_1) \\ k_2\,(1-s_2-f_{21}-f_{23}) & f_{21} & s_2 & f_{23} & (1-k_2)\,(1-s_2-f_{21}-f_{23}) \\ k_3\,(1-s_3-f_{32}) & 0 & f_{32} & s_3 & (1-k_3)\,(1-s_3-f_{32}) \\ 0 & 0 & 0 & 0 & 1 \end{pmatrix} \begin{pmatrix} P_0 \\ P(\Upsilon(1\mathrm{S})) \\ P(\Upsilon(2\mathrm{S})) \\ P(\Upsilon(3\mathrm{S})) \\ P_4 \end{pmatrix} \quad (26)$$

There are matrix elements that are explicitly set to zero, reflecting the fact that the contribution of some physics processes to certain mass intervals is minimal and neglected. This matrix can be inverted to determine $P(\Upsilon(n\mathrm{S}))$ from $P(m_n^{\mu\mu})$ measured in the data.

Examples of the background-dominated distributions for n_{ch} in mass intervals $m_0^{\mu\mu}$ and $m_4^{\mu\mu}$ that are shown with triangles in the right panel of Figure 42 are seen to be close to each other, in spite of the fact that $P(m_0^{\mu\mu})$ has a small admixture f_{01} of the contribution $P(\Upsilon(1\mathrm{S}))$. This supports the usage of the side-band subtraction method to reliably determine the shape of the background n_{ch} distributions at any $m^{\mu\mu}$. Transformation by the matrix given by Equation (26) can be seen as the transition between the curves with open and closed markers of the same shape. These are shown for $m_1^{\mu\mu}$ and $m_3^{\mu\mu}$ intervals as having the largest and the smallest signal contributions, respectively. n_{ch} distributions for the three $\Upsilon(n\mathrm{S})$ states are shown with full markers. These distributions have visibly different mean values. All n_{ch} distributions have contributions coming from the PU that is shown only for $\Upsilon(3\mathrm{S})$ with hatched markers because all PU contributions have the same shape. Fitting of invariant mass distributions and signal extraction is done identically for all PU intervals that are explained earlier, but independently for each $p_{\mathrm{T}}^{\mu\mu}$ interval and for each trigger.

The accuracy of the procedure is checked using pseudo-experiments. High-statistics MC samples are produced for all signal n_{ch} distributions and for the background. Shapes of the simulated distributions in the pseudo-experiments are matched to be close to the data. Those distributions are then used to produce $P(m_n^{\mu\mu})$ distributions that are used as input to the procedure described above. This is done for all $p_{\mathrm{T}}^{\mu\mu}$ measured in the analysis. At most, 1% deviations are observed for the three $\Upsilon(n\mathrm{S})$ states from the simulated signal distributions. The difference between reconstructed and actual values is included in the systematic uncertainties.

4.6.5 PU removal

Data events are characterized with the PU estimator ν, and the analysis is performed in 0.5 track intervals of ν. The signal-extraction procedure described up to this point is done in a 'ν-invariant' way. All PU intervals have been treated in the same way. Figure 43 shows on the left the n_{ch} distributions in $m_1^{\mu\mu}$ and in the middle the n_{ch} distribution in

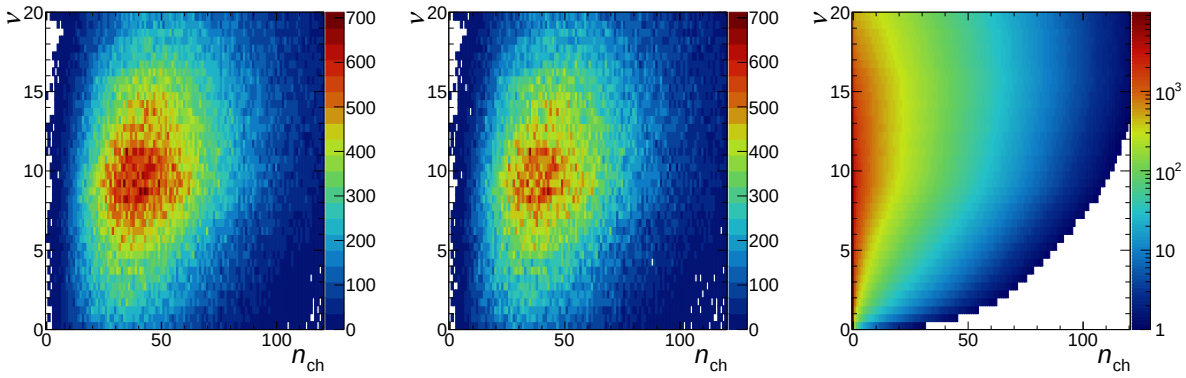

Figure 43: n_{ch} distributions in $m_1^{\mu\mu}$ (left) and Υ(1S) (middle) regions in a p_{T} slice, shown for different values of ν. The right panel shows a Mixed sample with the same number of events.

events with Υ(1S). The right panel of the figure shows the n_{ch} distribution for different ν in *Mixed* events. Each ν slice has the same number of events as in Υ(1S) data; however, the *Mixed* histogram is much better defined because it benefits from huge statistics of the *Mixed* event sample. The PU contribution also varies with $p_{\mathrm{T}}^{\mu\mu}$ due to the changing mixture of triggers during the data taking. For the kinematic distributions and for measuring the moments of the n_{ch} distributions, the corresponding matrices are projected onto the x-axis. The results are subtracted from each other to work out kinematic distributions. For the moments, they are treated according to the formula for the moments of convolved distributions.

$$\begin{aligned} \mathcal{M}_1^{\mathrm{signal}} &= \mathcal{M}_1^{\mathrm{measured}} - \mathcal{M}_1^{\mathrm{PU}} \\ \mathcal{M}_2^{\mathrm{signal}} &= \mathcal{M}_2^{\mathrm{measured}} - \mathcal{M}_2^{\mathrm{PU}} - 2\mathcal{M}_1^{\mathrm{measured}}\mathcal{M}_1^{\mathrm{PU}} \end{aligned} \tag{27}$$

where $\mathcal{M}_1$ and $\mathcal{M}_2$ are the first and the second moments respectively. However, as was mentioned in Section 4.3, there are two mechanisms of PU track production:

- The linear component is related to the presence of a track coming from PU events that are accepted into the analysis.
- The non-linear component is related to the increase of occupancy in the detector channels due to signal and PU tracks. Thus, this component depends on both types of tracks.

The procedure of evaluating and removing the linear PU component was discussed in Section 4.3. Correction for the non-linear PU component is worked out based on Figure 44. Different panels are for five $p_{\mathrm{T}}^{\mu\mu}$ intervals used in the analysis. Curves in each panel

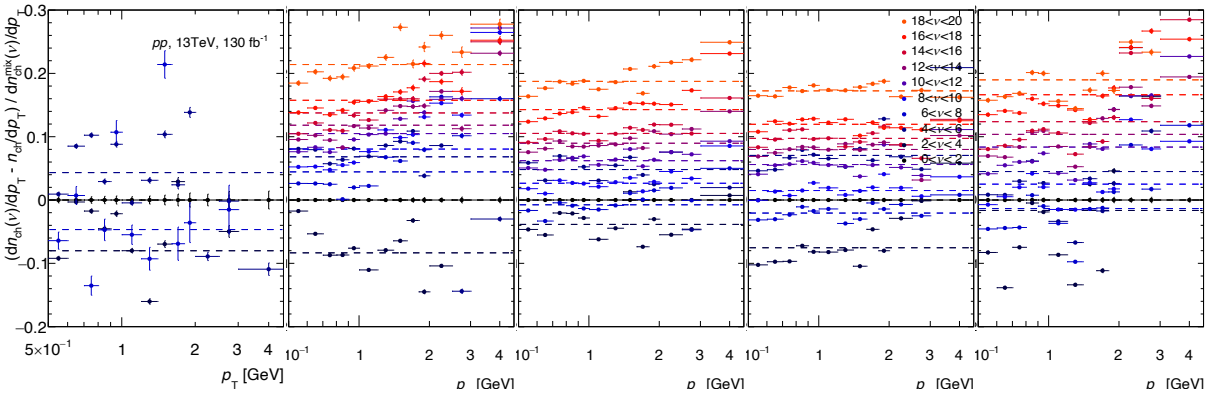

Figure 44: Residual ν dependence in $p_{\mathrm{T}}^{\mu\mu}$ interval used in the analysis. From left to right in GeV: [0,5], [5,10], [10,20], [20,30], [30...]. Different curves are for different intervals of ν as indicated in the panel. Dashed lines are constant fits to data points of the same color.

correspond to several intervals of ν. The analysis is performed in steps of PU estimator ν equal to 0.5, but this plot uses steps of $\nu = 2$ to increase the statistics of each curve. For the same reason, the results of different $\Upsilon(n\mathrm{S})$ are summed up. Each curve shown in the figure is a relative excess in the number of tracks n_{ch} in an interval of ν: $\mathrm{d}n_{\mathrm{ch}}(\nu)/\mathrm{d}p_{\mathrm{T}}$ over the interval with $\nu = 0$: $\mathrm{d}n_{\mathrm{ch}}(0)/\mathrm{d}p_{\mathrm{T}}$. Since such an interval is not available, the interval $\nu < 2$ is used instead. The is plotted relative to the Mixed p_{T} spectrum: $\mathrm{d}n_{\mathrm{ch}}^{\mathrm{mix}}(\nu)/\mathrm{d}p_{\mathrm{T}}$, at the same interval of ν by which it is divided. Data in the left panel does not have high-ν statistics, and therefore it has less curves.

Two observations can be made from Figure 44. In all panels, the magnitude of the points increases with increasing ν. In all curves, the p_{T} dependence of the points is weak. This supports the idea that the difference between the high- and low-ν to first order is a missing part of the Mixed spectrum, i.e., the PU. This can be due to the deviation of ν

from its actual value or the non-linear PU component. It also does not contradict possible detector instability, although it implies that the detector efficiency increases with time (following the increase of μ), which is less likely. In the first two cases, the residual PU corrections should make higher-ν data more consistent with low-ν. The curves shown in all panels are approximated with constant functions, and their dependence on ν is shown in the left panel of Figure 45. Curves for five $p_{\mathrm{T}}^{\mu\mu}$ intervals are consistent with each other.

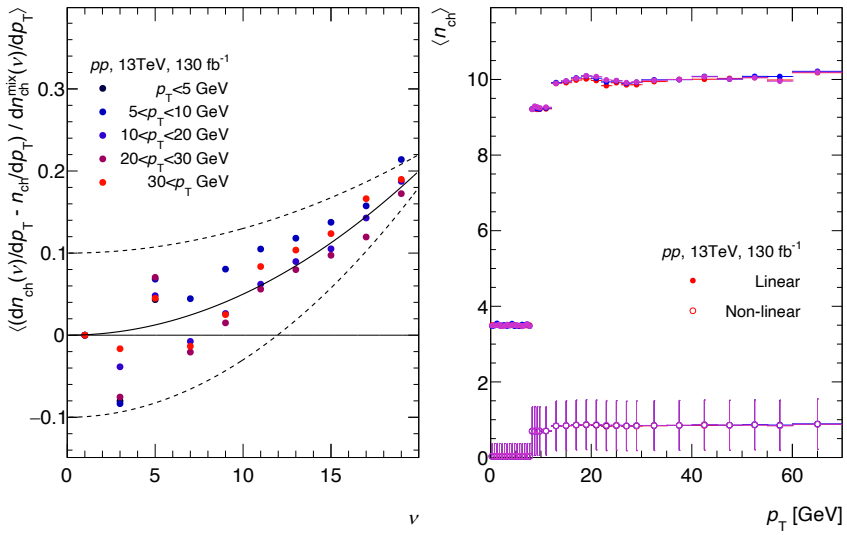

Figure 45: Left: Excess in $\langle n_{\mathrm{ch}} \rangle$ particles in different PU intervals over the lowest PU interval ($\nu = 0$) as a function of ν for different $p_{\mathrm{T}}^{\mu\mu}$ intervals. The solid line is the correction and dashed lines are its uncertainty. Right: Linear and Non-linear (with uncertainties) components of the PU as a function of $p_{\mathrm{T}}^{\mu\mu}$.

The solid line reflects the overall trend of all points and is taken as a correction. The curves are forced to zero at $\nu = 0$ by construction, as it becomes irrelevant when there is no PU. The shape of the curve is chosen as parabolic, although it can also be taken as linear. The curve reaches 0.2 at the highest $\nu = 20$ used in the analysis, reflecting the fact that such data shall be corrected by subtracting four more tracks in addition to 20 tracks subtracted for the linear PU component. The uncertainty on the correction comes from the spread between points and the fact that the (relative) correction is only loosely constrained at low-ν since the correction relies on the assumption that it zeroes out at $\nu = 0$.

The PU conditions and magnitudes of the corrections are shown in the right panel of Figure 45. Full circles show the linear PU component, and open circles - non-linear. For

all $\Upsilon(n\mathrm{S})$ states, the conditions are very similar. Both components have steps where they increase as a function of p_{T}, which corresponds to the use of higher p_{T} triggers which data is coming from later runs with higher luminosity μ and correspondingly higher ν. At low momentum, where all data is coming from a 2mu4 trigger, the PU is less than four tracks per event on average, and the highest p_{T} reaches ten tracks. The non-linear component that is coming from ν-distributions of individual $p_{\mathrm{T}}^{\mu\mu}$ bins is obtained by weighting the distributions with the curve shown in the left panel. The error bar reflects the uncertainty defined by the two dashed curves and relates to both linear and non-linear PU components.

4.7 Systematic uncertainties

There are three primary sources of *systematic uncertainties* that affect the charged particle multiplicity and kinematic distributions measured in the analysis. The first includes factors related to the performance of the ID tracking system - material uncertainties and the physics model used in simulation [89]. The second source of systematic uncertainties, which is the dominant contribution to the total uncertainty at low $p_{\mathrm{T}}^{\mu\mu}$, includes factors coming from the uncertainties and assumptions made in the $\Upsilon(n\mathrm{S})$ signal extraction. They are evaluated by varying the parameters of the fitting function, by changing the limits of invariant mass intervals shown in the left panel of Figure 42, where the charged distributions are extracted, and by performing the analysis in $|y^{\mu\mu}| < 1.05$ where the detector momentum resolution for the muons is higher. In addition, the signal extraction procedure is tested using MC-based pseudo-experiments, which have distributions closely matched to the data. This sample is constructed as follows.

- The shapes of $\Upsilon(n\mathrm{S})$ mass peaks are constructed using parametrized MC as shown in Figure 37 with red curves.

- The mass distributions of the combinatorial background is taken from the data using the parametrization shown in the bottom-right panel of Figure 39.

- Yields of the three Υ states and the background are taken with the weight obtained from the black curves (corresponding to trigger 2mu4) according to the curves shown in the four panels of Figure 40. These steps produce data-like invariant mass distributions for all p_{T} bins used in the analysis. An example of the invariant mass distribution is shown in the left panel of Figure 46 for $\Upsilon(1\mathrm{S})$ $p_{\mathrm{T}} < 5$ GeV. This

peak is a pseudo-experiment analog of the peak shown in the upper-left panel of Figure 41.

- The distributions of the n_{ch} are assumed to obey the negative binomial distribution with the mean values and the widths resembling the data. For that purpose, the p_{T}-dependencies $\langle n_{\mathrm{ch}} \rangle$ are fitted with smooth lines. Shape for $\Upsilon(n\mathrm{S})$, and background in low- and high-mass regions, denoted as B_L and B_H respectively, using the NBD are shown in the right panel of Figure 46.

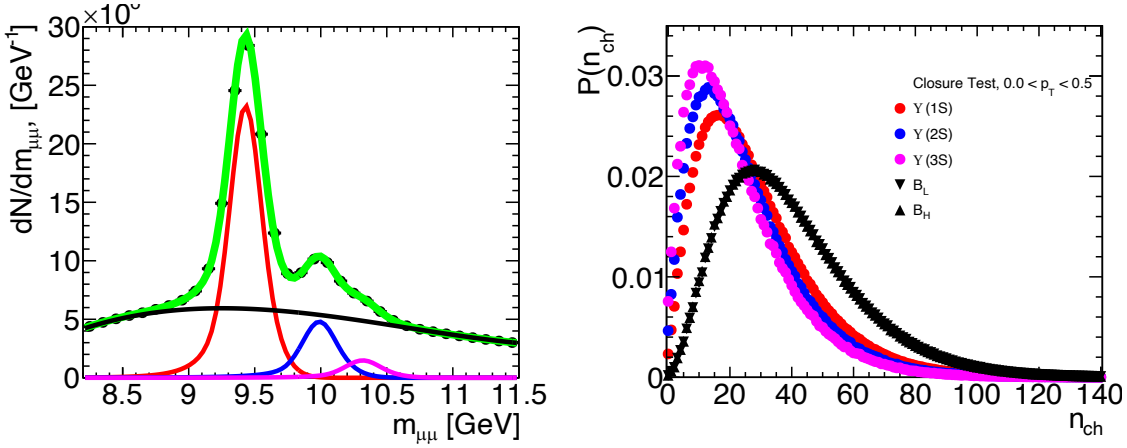

Figure 46: Left: Simulated dimuon mass distribution in the selected p_{T} interval. Right: Simulated n_{ch} distributions for $\Upsilon(n\mathrm{S})$ and combinatorial background.

- The mass dependence of the n_{ch} distribution of the background at any given mass is constructed from B_L and B_H shapes using Bernoulli trials with the probability

$$p\,(m) = \frac{m_{max} - m}{m_{max} - m_{min}}$$

- Each p_{T} interval uses 300 times more counts than the data.

- Since the signal extraction is insensitive to the presence of the PU component in the events, the PU is not a part of the pseudo-experiment.

The input of the pseudo-experiment is used for the fitting procedure, and its output is used to extract the signal. Figure 47 shows the comparison of the input (lines) and output (markers) of the closure test. Ratios shown in the lower panel demonstrate that the signal extraction procedure demonstrates better than 1% accuracy for all $\Upsilon(n\mathrm{S})$ at all

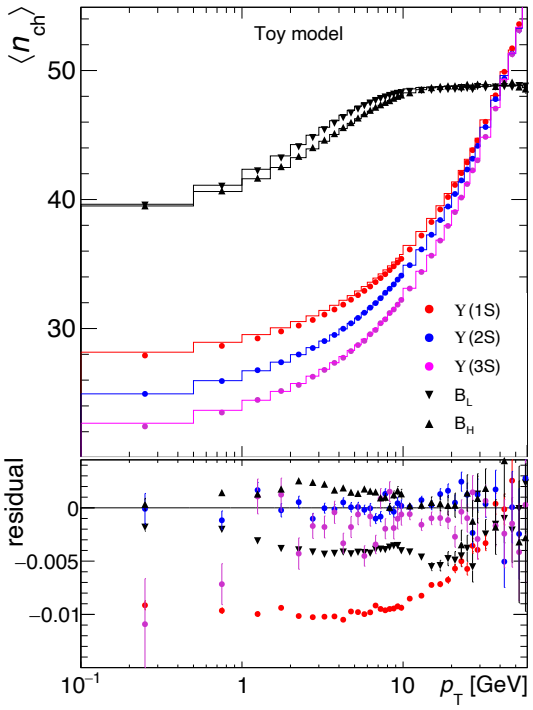

Figure 47: Left: Simulated n_{ch} distributions for $\Upsilon(n\mathrm{S})$ and combinatorial background. Right: Simulated dimuon mass distribution in the selected $p_{\mathrm{T}}^{\mu\mu}$ interval.

$p_{\mathrm{T}}^{\mu\mu}$. It is feasible that the largest deviation seen for $\Upsilon(1\mathrm{S})$ is due to neglecting the contribution of $\Upsilon(2\mathrm{S})$ to $m_1^{\mu\mu}$ mass region due to zeroing the corresponding matrix element in Equation (26) and can further be improved. However, being a subdominant contribution compared to other sources, it is currently added to other systematic uncertainties. The last source of systematic uncertainties includes PU subtraction, detector stability, and misreconstructed track production. Since the PU conditions varied significantly over the time of the data taking, these are considered together and assigned a common uncertainty. This uncertainty is studied by examining collisions with different PU conditions and evaluating residual discrepancies between the expectation based on the PU track estimator [79] and the mean number of measured tracks.

The resulting systematic uncertainties from different sources are plotted in Figure 48 for the three $\Upsilon(n\mathrm{S})$ states shown in the panels from left to right. Dominant systematic uncertainty comes from the difference-making the analysis in $|y^{\mu\mu}| < 1.6$ and in the barrel. It is dominant at low p_{T}. Next-to-the-leading systematic uncertainty is due to PU, and it is somewhat higher at high-p_{T}, where data is coming from high luminosity runs. Uncertainty due to the track reconstruction is flat at 1%, and other signal-extraction

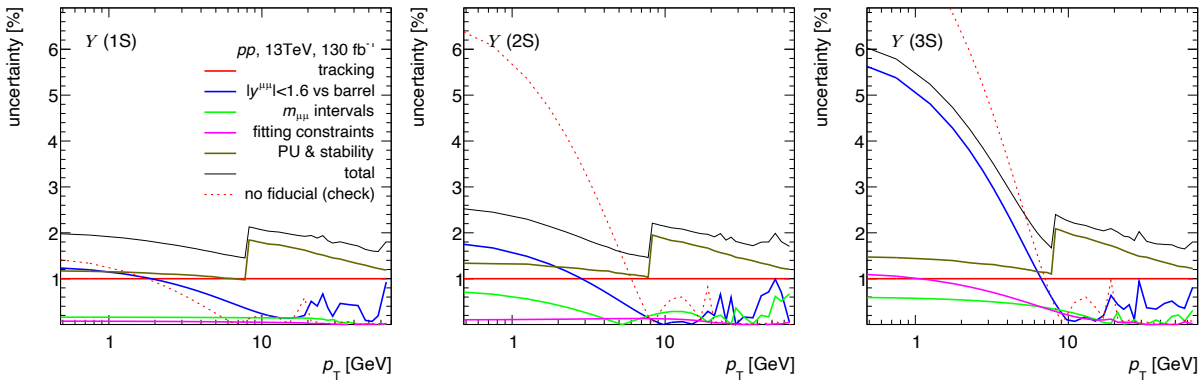

Figure 48: Total systematic uncertainties and their partial contributions to the Υ(1S), Υ(2S), and Υ(3S) states are plotted in the three panels from left to right as a function of $\Upsilon(n\mathrm{S})$ p_T. Dashed red curves corresponding to not applying fiducial acceptance correction are cross-checks and are not added to the total systematic uncertainty.

uncertainties have smaller magnitudes. Since sources of all uncertainties are independent, the resulting uncertainty is obtained by adding values in quadrature.

This analysis works out distributions resulting from subtraction n_ch measured in collisions of Υ(1S) and higher $\Upsilon(n\mathrm{S})$. For those values, tracking uncertainty and PU uncertainty are considered fully correlated and applied only once to the difference. Uncertainty related to the barrel region of the detector is also correlated. The difference between the systematics is taken for this source. Other uncertainties are also partially correlated, but they are small, and the degree of their correlation is difficult to estimate.

Table 3 lists the systematic uncertainties used in final plots for different kinematic

	$p_\mathrm{T}^{\mu\mu} \leq 4$ GeV	$4 < p_\mathrm{T}^{\mu\mu} \leq 12$ GeV	$12 < p_\mathrm{T}^{\mu\mu} \leq 30$ GeV	$p_\mathrm{T}^{\mu\mu} > 30$ GeV
Υ(1S)	0.5 – 0.6	0.5 – 0.7	0.7 – 0.8	0.8 – 0.9
Υ(2S)	0.6 – 0.6	0.5 – 0.7	0.7 – 0.8	0.8 – 1.0
Υ(3S)	0.9 – 1.3	0.5 – 0.8	0.7 – 0.8	0.8 – 0.9
Υ(1S) – Υ(2S)	0.11 – 0.15	0.06 – 0.10	0.12 – 0.21	0.2 – 0.5
Υ(1S) – Υ(3S)	0.6 – 0.9	0.14 – 0.36	0.14 – 0.15	0.16 – 0.19

Table 3: Systematic uncertainties for $\langle n_\mathrm{ch} \rangle$ measurements and their differences for different $\Upsilon(n\mathrm{S})$ states and for the difference between $\langle n_\mathrm{ch} \rangle$ measured for $\Upsilon(1\mathrm{S}) - \Upsilon(n\mathrm{S})$. The values are the number of charged particles with $0.5 \leq p_\mathrm{T} < 10$ GeV and $|\eta| < 2.5$.

intervals of $\Upsilon(n\mathrm{S})$. The systematic uncertainty is given in the absolute number of n_{ch}.

4.8 Main findings of the Upsilon–UE correlation studies

4.8.1 Kinematic distributions

Figure 49 shows the kinematic distributions of charged particles measured in collisions with $\Upsilon(n\mathrm{S})$ states. The left panel shows the p_{T} distributions, and the right panel the distributions of the azimuthal angle between the directions of the particles and the Υ-meson ($\Delta\phi$). In both panels, cross-shaped markers shown in black are distributions measured in collisions with $\Upsilon(1\mathrm{S})$ meson for different intervals of the momentum of the muon pair. We shall discuss them first. The lowest black curves in each panel correspond to the lowest interval of $p_{\mathrm{T}}^{\mu\mu} < 4$ GeV. In the right panel, this distribution is nearly flat, demonstrating that the direction of the $\Upsilon(1\mathrm{S})$ and charged particles are uncorrelated. With the increasing momentum of the muon pair, the $\Delta\phi$ curves start to develop characteristic peaks corresponding to the near-side ($\Delta\phi \approx 0$) and away-side ($\Delta\phi \approx \pi$) jets. Notably, the near-side peaks are weaker, which is due to the fact that $\Upsilon(1\mathrm{S})$, as a leading particle, takes upon itself a significant part of the jet energy. Thus the near-side peak has lesser particles than the away-side peak. This also explains the flatness of the $\Delta\phi$-distribution in the lowest $p_{\mathrm{T}}^{\mu\mu} < 4$ GeV interval as particles forming it are coming from the UE because jets are constrained by the low momentum of the leading particle and momentum balance. This allows making the statement that plays a vital role in understanding the results. *Kinematic distribution of the charged particles in the UE can be approximated by the curves corresponding to the lowest momentum of $\Upsilon(1S)$.* Since there is no other experimental way to separate the particles of the UE from particles accompanying Υ production, we rely on the above statement.

Black solid lines drawn close to black markers are calculations made with Pythia8 [17] MC generator. These results include the feed-down processes of higher $\Upsilon(n\mathrm{S})$ states decaying into $\Upsilon(1\mathrm{S})$, but they do not take into account $\chi_b(m\mathrm{P}) \to \Upsilon(n\mathrm{S})$ decay channels. Generally, Pythia8 does not reproduce the data, especially in the region of the near-side jet, and it also predicts lower UE than it is measured in the data. Details concerning the quarkonia production mechanism in Pythia8 that would explain visible discrepancies are known [95] but are not a part of this project.

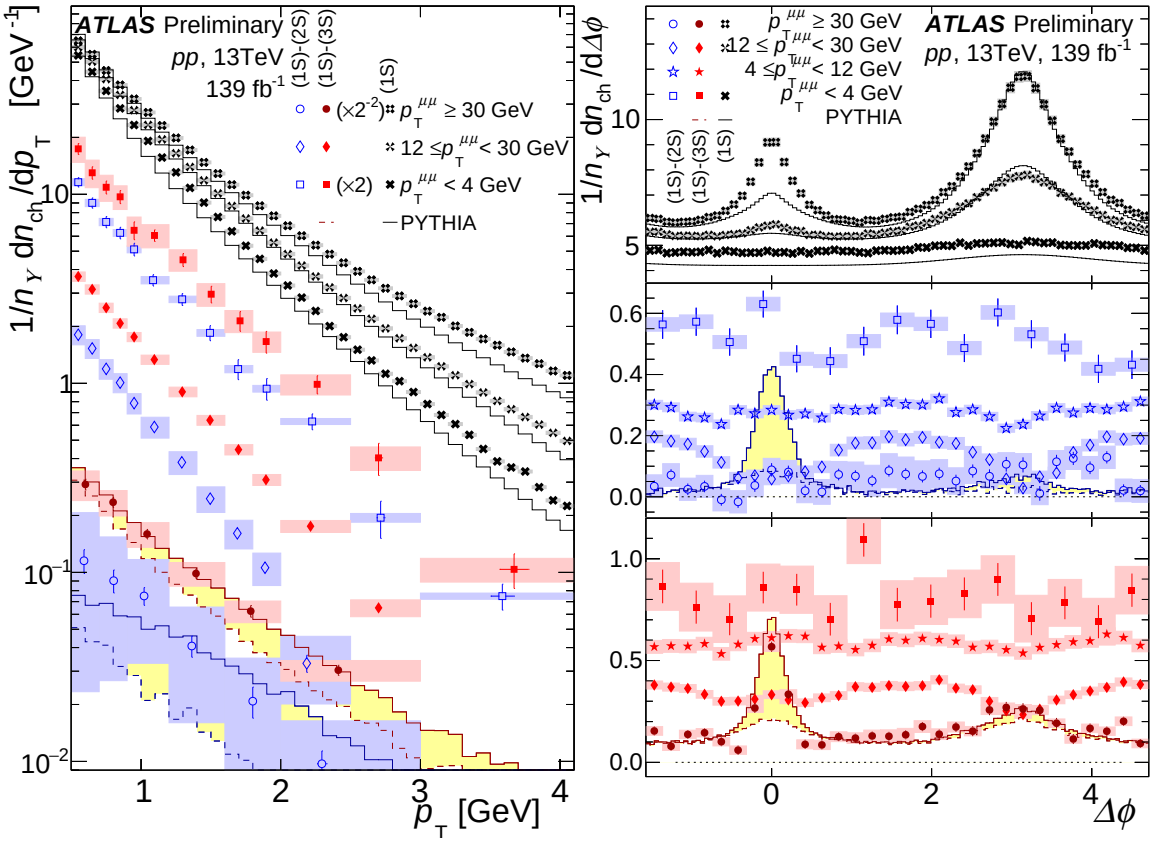

Figure 49: Distributions of charged particles in p_{T} (left) and $\Delta\phi$ (right) in collisions with different Υ-meson $p_{\mathrm{T}}^{\mu\mu}$. Cross-shaped markers correspond to $\Upsilon(1\mathrm{S})$, open markers to $\Upsilon(1\mathrm{S}) - \Upsilon(2\mathrm{S})$, and full markers to $\Upsilon(1\mathrm{S}) - \Upsilon(3\mathrm{S})$, respectively. Pythia8 predictions are plotted in solid black lines for $\Upsilon(1\mathrm{S})$. In the subtracted distributions, Pythia8 simulations are plotted in colored lines for the $p_{\mathrm{T}}^{\mu\mu} \geq 30$ GeV selections. Solid and dashed lines are Pythia8 predictions with and without $\Upsilon(n\mathrm{S}) \to \Upsilon(m\mathrm{S})$ contributions, respectively. Regions filled with yellow represent the difference between the predictions with and without feed-down decays. Bars and boxes are statistical and systematic uncertainties, respectively. p_{T} distributions of subtracted results are scaled for plot clarity, as indicated in the legend.

Other curves shown in Figure 49 with colored markers are the *subtracted* distributions, i.e., the differences between the results measured in collisions with $\Upsilon(1\mathrm{S})$ and higher $\Upsilon(n\mathrm{S})$ states, $\Upsilon(1\mathrm{S}) - \Upsilon(2\mathrm{S})$ are shown with blue (open) markers and $\Upsilon(1\mathrm{S}) - \Upsilon(3\mathrm{S})$ with red (full) markers. The distributions are also shown in several intervals of $p_{\mathrm{T}}^{\mu\mu}$.

A striking feature that is clearly visible in the data is that all subtracted distributions are strictly positive, including even the highest measured $p_{\mathrm{T}}^{\mu\mu}$ interval. This points to the

fact that there are more charged particles present in collisions with $\Upsilon(1S)$ than in collisions with excited $\Upsilon(n\mathrm{S})$ states. For both excited states, the effect is more pronounced at the lower $p_{\mathrm{T}}^{\mu\mu}$ but retains at any measured momentum. $\Upsilon(1S) - \Upsilon(2S)$ measures up to 0.5 extra charged particles per unit of azimuthal angle, and $\Upsilon(1S) - \Upsilon(3S)$ up to 0.8 particles.

Another striking feature is that the subtracted distributions are consistent in shape with the $\Upsilon(1S)$ distributions measured for the lowest $p_{\mathrm{T}}^{\mu\mu} < 4$ GeV, i.e., as we argued earlier, they have the kinematics of the UE. This is clearly visible for both species with $p_{\mathrm{T}}^{\mu\mu} < 30$ GeV, and above that, subtracted distributions start to develop jet-like features and get harder spectrum. To a large extent this departure of the shapes from the UE towards jets can be explained by the feed-down processes of higher $\Upsilon(n\mathrm{S})$ states into $\Upsilon(1S)$. This is shown with colored lines that are modified PYTHIA8 distributions corresponding to $p_{\mathrm{T}}^{\mu\mu} > 30$ GeV momentum interval.

The modified PYTHIA8 distributions are constructed in the following way. Since PYTHIA8 does not reproduce the effect of different n_{ch} in collisions with different species, the simulated distributions are first normalized to the data. This normalization is done by matching integrals of measured and simulated distributions outside the region of the near-side peak. Then the simulated distributions for $\Upsilon(n\mathrm{S})$ are subtracted from $\Upsilon(1S)$ and plotted in Figure 49 with colored solid lines. After that, the simulated charged particles that are coming from the feed-down decay processes $\Upsilon(n\mathrm{S}) \to \Upsilon(1S)$ are removed from the subtracted distributions keeping the same normalization, and the results are plotted with dashed lines. For visibility, the difference between the distributions with and without feed-downs is highlighted in yellow color. It is easy to see that the hardening of the n_{ch} p_{T} spectra and jet-like peak in $\Upsilon(3S) - \Upsilon(1S)$ can be largely explained by the feed-downs.

Other non-uniformities in subtracted $\Delta\phi$ distributions become pronounced in $12 \leq p_{\mathrm{T}}^{\mu\mu} < 30$ GeV momentum interval. Several physics processes may contribute to this, including feed-down decays from $\chi_b(m\mathrm{P})$ mesons into $\Upsilon(n\mathrm{S})$ (which are not accounted for in the PYTHIA8 predictions), slightly more energetic jets containing lighter Υ mesons and other factors. Nevertheless, in the region around $\Delta\phi = \pm\pi/2$, the difference in the $\mathrm{d}n_{\mathrm{ch}}/\mathrm{d}\Delta\phi$ always remains above zero for both $\Upsilon(1S) - \Upsilon(2S)$ and $\Upsilon(1S) - \Upsilon(3S)$ distributions. This allows the conclusion that the difference between collisions of $\Upsilon(n\mathrm{S})$ states with the same momentum is mainly in the activity of the UE and much less associated with jets that are correlated to Υ mesons.

The main finding of the $\Upsilon(n\mathrm{S})$–UE correlation analysis is that the excited $\Upsilon(n\mathrm{S})$ states reside in the event with lesser n_{ch}. The particles that are present in events with $\Upsilon(1\mathrm{S})$ and missing in the others have the distribution consistent with the UE. The effect is most pronounced at lower p_{T} of the Υ meson but is visible at any measured momentum. Known effects like feed-downs from higher $\Upsilon(n\mathrm{S})$ states into the ground state do not explain the phenomenon. Pythia8 event generator does not have this effect either. A similar mismatch between data and Pythia8 was reported in Ref. [96].

4.8.2 Consistency with CMS results

The results presented in this report can be compared to the results obtained by CMS collaboration [15]. This comparison can only be made quantitatively for two reasons. The first is that the CMS results are measured at $\sqrt{s} = 7$ TeV. The second is that the particle ratios published by the CMS are composite values.

$$\frac{\Upsilon(n\mathrm{S})(p_{\mathrm{T}}, n_{\mathrm{ch}})}{\Upsilon(1\mathrm{S})(p_{\mathrm{T}}, n_{\mathrm{ch}})} = \frac{\mathrm{d}\sigma^{n\mathrm{S}}/\mathrm{d}p_{\mathrm{T}}(p_{\mathrm{T}})}{\mathrm{d}\sigma^{1\mathrm{S}}/\mathrm{d}p_{\mathrm{T}}(p_{\mathrm{T}})} \times \frac{P(n\mathrm{S}, n_{\mathrm{ch}})}{P(1\mathrm{S}, n_{\mathrm{ch}})}$$

The first term, $\left(\mathrm{d}\sigma^{n\mathrm{S}}/\mathrm{d}p_{\mathrm{T}}(p_{\mathrm{T}})\right) / \left(\mathrm{d}\sigma^{1\mathrm{S}}/\mathrm{d}p_{\mathrm{T}}(p_{\mathrm{T}})\right)$, is the ratio of the cross sections and at $\sqrt{s} = 13$ TeV is not yet measured by the ATLAS experiment. On the other hand, this term is just some numerical factor, and it does not affect the shapes. The second term in the equation is $P(n\mathrm{S}, n_{\mathrm{ch}})/P(1\mathrm{S}, n_{\mathrm{ch}})$ is the ratio of the probability distributions, and these are directly measured in the ATLAS analysis and unfolded for the PU. They are shown in Figure 50 for several $p_{\mathrm{T}}^{\mu\mu}$ intervals.

Comparison to the CMS results is given in Figure 51. Since the $P(n\mathrm{S}, n_{\mathrm{ch}})$ distributions are normalized to unity, their ratios are also close to unity. Therefore they are scaled by arbitrary factors for figure clarity. It is clear that the results of the CMS experiment can be reproduced in this study with higher statistical accuracy and in wider n_{ch} intervals. To the extent such comparison is adequate, the results are consistent.

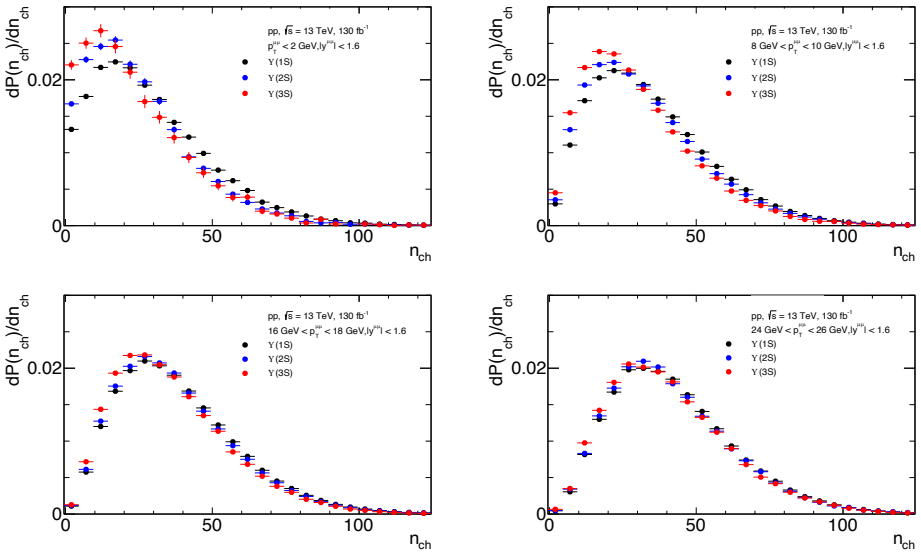

Figure 50: Examples of unfolded n_{ch} distributions of $\Upsilon(n\mathrm{S})$ states in different $p_{\mathrm{T}}^{\mu\mu}$ intervals.

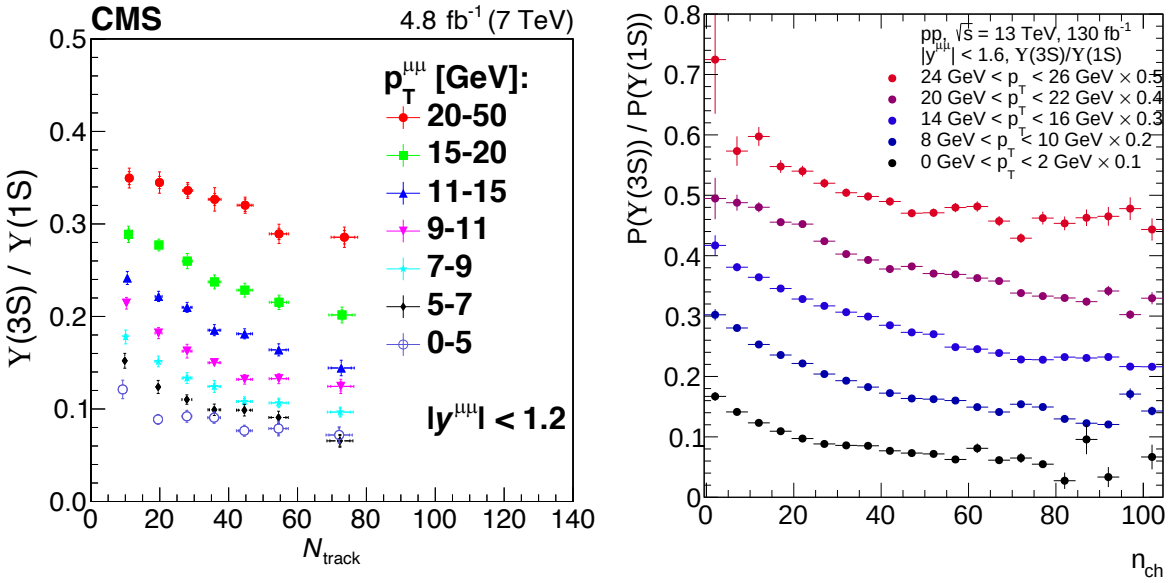

Figure 51: Left: results of CMS experiment from Ref. [15]. Right: Ratios of n_{ch} distributions for $\Upsilon(2\mathrm{S})/\Upsilon(1\mathrm{S})$ and for $\Upsilon(3\mathrm{S})/\Upsilon(1\mathrm{S})$. Ratios have arbitrary normalization for figure clarity.

5 Analysis 2. Analysis of meson spectra at the LHC

5.1 Motivation and the goal

This analysis is a direct outcome of the finding made in the process of working on Υ–UE correlations. Once it became clear that the $n_{\rm ch}$ is different in events with different $\Upsilon(n\rm S)$ it supported the idea of the Υ suppression in pp. In such a case, the yields of the mesons should be modified and, in principle, measurable in the experiment. Since there is no a-priory knowledge about the production cross-sections of $\Upsilon(n\rm S)$ states, and available theoretical calculations [97], although they show significant discrepancies with the data and have limited accuracy at the lowest $p_{\rm T}$.

It is also shown in Section 4.8 that the difference in $n_{\rm ch}$ between $\Upsilon(1\rm S)-\Upsilon(n\rm S)$ changes with $p_{\rm T}$. That hints to the fact that not only the yields but the spectral shapes of different $\Upsilon(n\rm S)$ states can also be modified. We explored this possible modification starting with the assumption that *particles with identical quark content and identical masses should have identical $p_{\rm T}$ distribution*. Although this only is an assumption, it is well based on the first principle.

The three $\Upsilon(n\rm S)$ states are all $b\bar{b}$ states with rather similar masses that only differ by 9% (between $\Upsilon(1\rm S)$ and $\Upsilon(3\rm S)$) and have a range from 9.46 GeV to 10.35 GeV. The difference in spectral shape that results from such difference in masses can be estimated using the so-called transverse mass ($m_{\rm T}$) scaling. $m_{\rm T}$-scaling was proposed by R. Hagedorn [98] and based on a statistical thermodynamic approach. In Ref. [98], it was suggested that hadron production in proton-proton (pp) collisions scales with the transverse mass of the produced particles. Transverse mass is defined as $m_{\rm T} = \sqrt{p_{\rm T}^2 + m^2}$, where $p_{\rm T}$ is the momentum of the hadron in the plane orthogonal to the collision axis, and m is its rest mass. This scaling was demonstrated experimentally in measurements at the ISR experiment [99, 100]. Although no longer thought to represent a fundamental hadronic temperature as originally proposed, it has since been used by many experiments and phenomenological studies to understand particle production in pp and nucleus-nucleus collisions from the SPS to RHIC and the LHC [18, 19, 19, 20]. Thus the $m_{\rm T}$ scaling, which is worked out here, is used as an empirical but robust approach to estimate how much $p_{\rm T}$ distributions of different $\Upsilon(n\rm S)$ states should differ from each other due to different

masses.

5.2 Data selection

This analysis uses published data from pp collisions at $\sqrt{s} = 7$, 8, and 13 TeV measured by ALICE [101–113], ATLAS [5, 114–120], CMS [6–8, 121–128], and LHCb [9–11, 129–137] experiments. The data points and their uncertainties are obtained from the values reported in the HEP database. The approach used in this analysis is first to validate the applicability of the m_{T}-scaling for high-energy LHC data and then use it to work out predictions for $\Upsilon(n\mathrm{S})$ states.

Published experimental data are selected and processed as follows:

- Only measurements of mesons are considered because baryons are known to obey the m_{T}-scaling with different parameters compared to mesons [138].
- Where available, the prompt production component is used. For charmonia states, it excludes feed-down contributions from B mesons but includes the feed-down from decays of heavier charmonium states. These processes may contribute more than 30% of the measured charmonium cross section [122], and even more than that for bottomonium states [139].
- In measurements that are corrected using different assumptions of the meson polarization, the results corresponding to zero polarization are selected.
- Measurements reported within a detector's fiducial acceptance are corrected to the total cross-sections using the zero polarization assumption.
- Since particle ratios for quarkonia states considered in this analysis are typically measured in dilepton decay channels; the particle ratios also include branching ratios.
- Cross-sections measured to rapidity larger than three but reported deferentially in rapidity are selected with $|y| < 3$ for better consistency with the results measured at mid-rapidity.

Measurements that contain less than 5 data points or span less than several GeV in transverse momentum are not used in the analysis. Where the same experiment provides

multiple measurements of the same particle, the measurements are considered to be independent and combined together using a constant scaling factor applied to one of the measurements. This factor is calculated to account for small differences in the properties of the different measurements, for example, the rapidity coverage. The magnitude of the factor is close to or equal to unity. Measurements of isospin-partner particles made by the same experiment and measurements of the same particles performed by different experiments are not combined. Altogether, this analysis uses 72 combined data samples of 18 particle species and their isospin partners with 1509 experimental data points and 15 measurements of particle ratios with 327 data points. They span transverse momentum interval from 0 to 150 GeV and absolute rapidity from 0 to 4.5.

5.3 Establishing the transverse-mass scaling validity

Each data sample is fitted to the functional form given by

$$\frac{\mathrm{d}^2\sigma}{\mathrm{d}y\mathrm{d}m_{\mathrm{T}}} \propto \left(1 + \frac{m_{\mathrm{T}}}{nT}\right)^{-n} \tag{28}$$

that may be derived from Tsallis statistics [138, 140]. Point-by-point uncorrelated uncertainties are used in the fits. Point-by-point fully correlated uncertainties (scaling factors) are not considered because the spectra of different particles are re-normalized in the analysis. The point-by-point correlated uncertainties are plotted but not input into the fits.

In addition to the general data handling discussed above, several data exclusions are made in the fitting procedure. Measurements of π^0 and $\pi^{\pm}$ with $p_{\mathrm{T}} < 2$ GeV are excluded based on the considerations discussed in Refs. [20, 105]. Low momentum, $p_{\mathrm{T}} < 5$ GeV, Υ meson measurements are also excluded from the fitting because in that region there is a large contribution from $\chi_b(\mathrm{mP}) \to \Upsilon(n\mathrm{S})\gamma$ decays with $m \geq n$. Correction for feed-down decays from heavier mesons (χ_c, χ_b) is not applied because it cannot be reliably determined from existing data, although it is expected to be similar in magnitude for all $\Upsilon(n\mathrm{S})$ states [13].

Since the fit parameters, T and n are strongly correlated; unconstrained fits produce results that are difficult to interpret coherently. Therefore, the parameter T is fixed to 254 MeV for all analyzed particles. This value is obtained from a simultaneous fit to several selected data sets at $\sqrt{s} = 7$ GeV and is close to the same parameter used in [20]. The exponent, n, obtained from the fits is plotted versus the particle rest mass in Figure 52

which shows that the values of n for u,d,s and ground-state heavy quarkonia ($q\bar{q}$) mesons

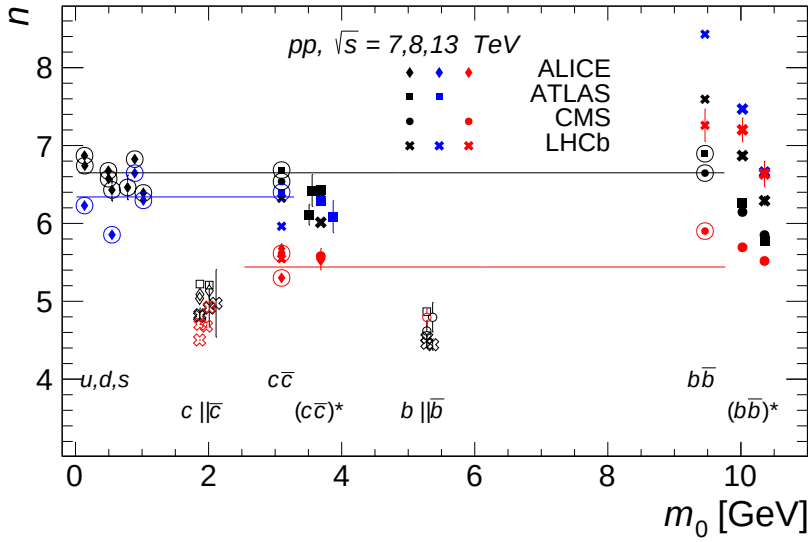

Figure 52: The mass dependence of the m_{T}-spectra exponent n for different measured species. Symbol shapes denote experiments, open symbols denote open heavy flavor particles, and larger symbols denote excited quarkonia states. Error bars are uncertainties of the fits. Encircled points indicate the results which are used in the common fit. Different colors represent different collision energies.

are similar.

Several trends are visible in Figure 52. Particles produced in collisions with higher $\sqrt{s}$ have harder spectra (lower n). The magnitude of n depends on the quark content of the particle. Open heavy flavor mesons ($q||\bar{q}$) demonstrate significantly harder spectra compared to other species and harder for the open bottom ($b||\bar{b}$) than for open charm ($c||\bar{c}$).

At each collision energy, the LHCb results for Υ-mesons are above others because they are measured at higher rapidity. Comparing results at the same energy as it is done in [140] shows that n increases with rapidity. Figure 52 shows that the exponent n for u,d,s and $q\bar{q}$ mesons are similar. At the same time, $(q\bar{q})^{\star}$ have lower values of n than the ground-state: $n_{J/\Psi} > n_{\Psi(2\mathrm{S})}$, and for bottomonia states: $n_{\Upsilon(1\mathrm{S})} > n_{\Upsilon(2\mathrm{S})} > n_{\Upsilon(3\mathrm{S})}$.

Based on these observations, the values of n for u,d,s and ground-state $q\bar{q}$ mesons measured at midrapidity (circled data points in Figure 52) are fit to extract a common n. There are 12, 5, and 3 data samples at $\sqrt{s}$ = 7, 8, and 13 TeV, respectively. The $\sqrt{s} = 7$ TeV values are fit to a linear function, which becomes constant for $T = 254$ MeV. Due to the low number of selected data sets at higher energies, the 8 and 13 TeV data

are initially fit to a constant. The values of n ($\sqrt{s} = 7, 8, 13$[TeV]) $= (6.65, 6.34, 5.44)$, are shown in Figure 52 with lines.

5.4 Exploring the common fit

Figure 53 shows the $\Upsilon(n\mathrm{S})$ results at 3 collision energies, divided by the common fit. The

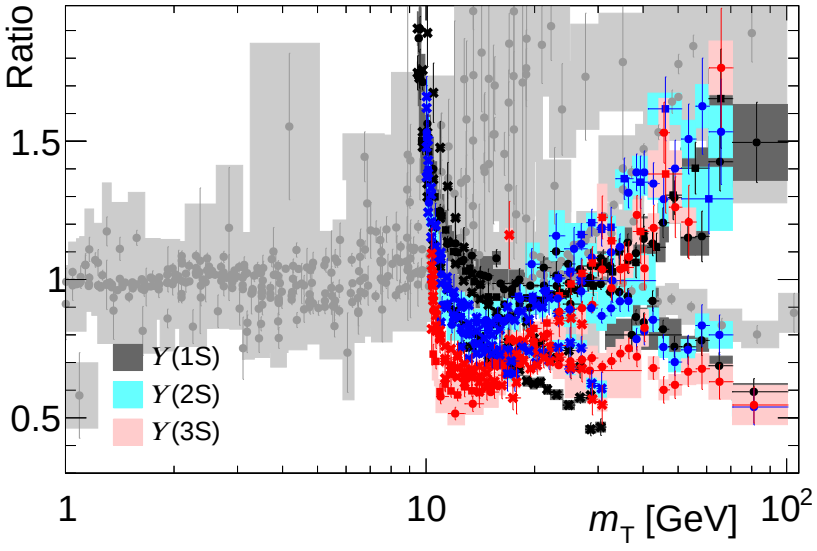

Figure 53: Spectra of individual particles divided by the common fit. Measurements used in the common fit are shown in gray. From reference [141].

Υ-points are shown in different colors, regardless of energy, and points that are used in the common fit are shown in gray. The latter demonstrate reasonable agreement with unity, although at high-p_T $q\bar{q}$ spectra tend to rise up to a factor of 2, somewhat similar to what can be seen in Ref. [140]. Using Equation (28) at high m_T this translates to $\mathrm{d}n/n \approx 1/n \times \mathrm{d}\sigma/\sigma \approx$ 15–18% deviation of n from the 'true scaling' value, which is comparable or even smaller than the difference in n at three measured energies. Similarly, the LHCb results, which are measured at high rapidity, yield a value of n that is larger approximately by 1 (see Figure 52) and constitutes approximately the same 20% deviation from the common n.

A significant rise for all $\Upsilon(n\mathrm{S})$ states at low p_T, i.e., $m_\mathrm{T} \gtrsim m$, is clearly visible. The contribution of $\chi_b(1\mathrm{P}) \to \Upsilon(1\mathrm{S})$ has been estimated using Pythia8 [142] simulations to work out the prompt fraction of $\Upsilon(1\mathrm{S})$. Inclusive data that is used in the analysis and the prompt fraction, estimated from Pythia8 are shown in Figure 54 with full and open

circles, respectively. The prompt fraction has only a weak excess at $m_{\mathrm{T}} \gtrsim m$, but it still

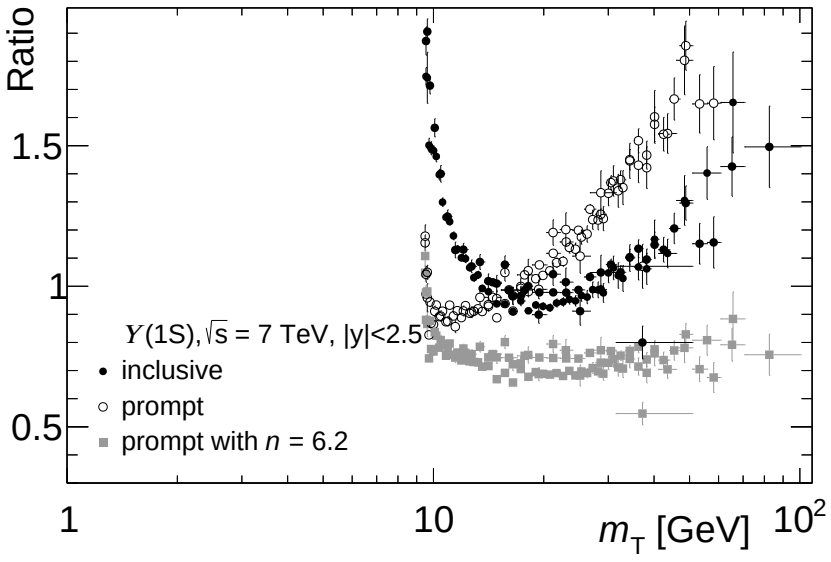

Figure 54: Spectra of $\Upsilon(1\mathrm{S})$ at $\sqrt{s} = 7$ TeV at midrapidity divided by the common fit. As used in the analysis (full circles), prompt fraction (empty circles), using different n in a common fit (squares). Points are shifted vertically for visibility.

rises at high p_{T}. Decreasing n by 8% flattens the ratio, as shown in the figure with squares. Nevertheless, inclusive data with $p_{\mathrm{T}} > 5$ GeV is used in the fit because prompt fractions for $\Upsilon(n\mathrm{S})$ are not yet reliably measured experimentally nor fully modeled successfully.

5.5 Particle ratios

The ratios of all $(q\bar{q})^{\star}/q\bar{q}$ measured at the LHC are shown in Figure 55. The ratio curves derived from m_{T}-scaling are drawn normalized to data at $p_{\mathrm{T}} > 50$ GeV, which uncertainties are shown with thin solid lines. Dashed lines correspond to higher energies. The shape of the curves can be directly derived from Equation (28) and is governed by their minimum-to-maximum span:

$$\frac{\min}{\max} \approx 1 - \frac{\Delta m}{nT + m} n, \tag{29}$$

where m corresponding to $\Upsilon(1\mathrm{S})$ is equal to 9.46 GeV and Δm is 0.9 GeV for $\Upsilon(3\mathrm{S})$. Equation (29) makes it clear that the value of T has only a minor effect on the shape because $nT \ll m$. Since $\Delta m \ll m$, even for $\Upsilon(3\mathrm{S})$, the ratio before n in Equation (29) is ≈ 0.08; therefore the two curves for $\sqrt{s} = 7$ and 13 TeV are close to each other. As discussed above, residual non-flatness of the common fit and the rapidity dependence

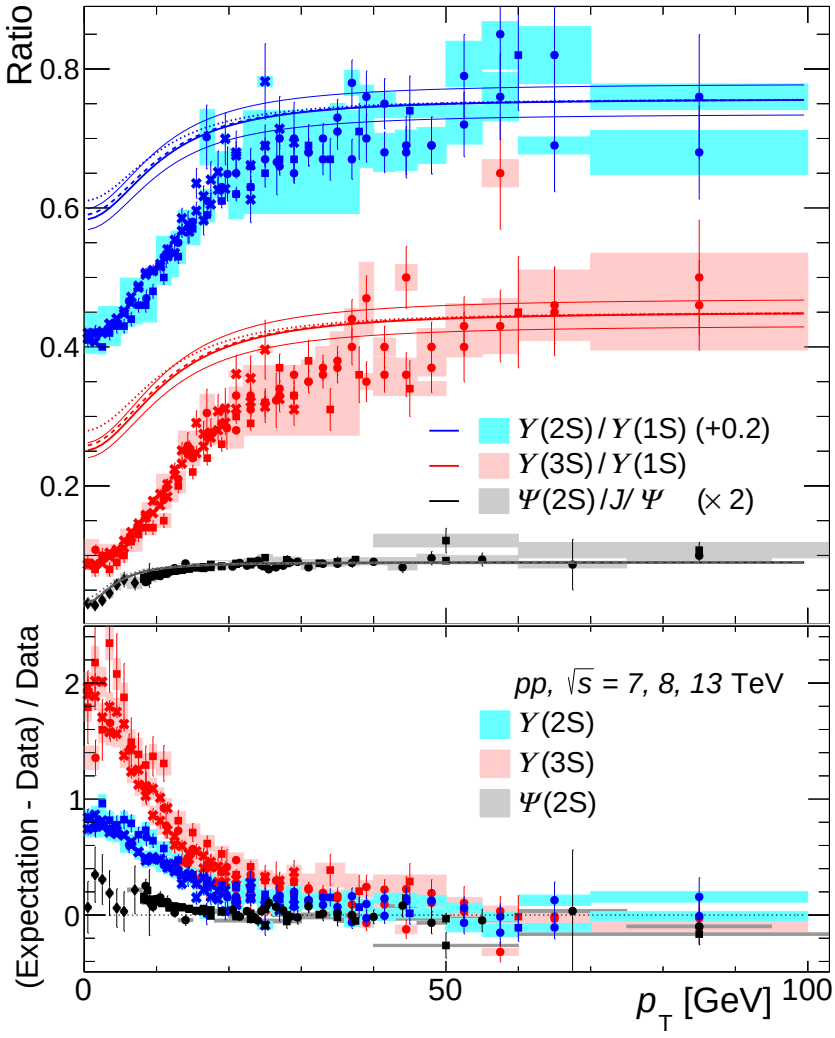

Figure 55: Measured $(q\bar{q})^\star/q\bar{q}$ ratios (markers) and m_{T}-scaling prediction normalized to the data at $p_{\mathrm{T}} > 50$ GeV with normalization uncertainties (solid lines). The dashed (dotted) lines correspond $\sqrt{s} = 8$ (13) TeV. From reference [141].

have similar or smaller impacts on n compared to $\sqrt{s}$. None of these effects can explain the drastic difference between the experimentally measured $(b\bar{b})^\star/b\bar{b}$ ratios and the curves shown in Figure 55. To reconcile $\Upsilon(2\mathrm{S})/\Upsilon(1\mathrm{S})$-ratio curve with the data, the feed downs from Pythia8 that are consistent with LHCb results [139] and nearly eliminate the peak at $m \lesssim m_{\mathrm{T}}$ in Figure 54, should be increased by 2.5 and even more than that for $\Upsilon(3\mathrm{S})$, which is not plausible.

5.6 Main findings of the spectra scaling studies

Particle ratios for excited-to-ground state $(q\bar{q})^\star/q\bar{q}$ states measured by different LHC experiments at different incident energies in pp collisions show shapes that are inconsistent

with the assumption made in Section 5.1 that particles with the same quark content and the same masses should have the same kinematics. An analysis of all available LHC data is used to demonstrate the robustness of the m_{T} scaling that holds for mesons in the mass range from pions to Υ mesons. Certain deviations that are seen in the data from the common scaling either relate to $q||\bar{q}$ particles that are not explored in this analysis or can be explained by differences in the conditions of the measurements. At the same time, the $(q\bar{q})^{\star}/q\bar{q}$, and especially $(b\bar{b})^{\star}/b\bar{b}$ ratios, violate the scaling, even though the particle masses of the particles are very close, less than 10% different. None of the known mechanisms, such as feed-downs, including feed-down from not fully explored χ_b states, can reconcile the observed differences.

To quantify the discrepancy between the data and the m_{T}-scaling prediction, one can build the particles' 'missing fraction': $(q\bar{q})^{\star}_{\mathrm{expected}}/(q\bar{q})^{\star}_{\mathrm{measured}} - 1$. This fraction is shown in the lower panel of Figure 55. Assuming the m_{T}-scaling scenario and the $\Upsilon(1\mathrm{S})$-meson production cross-section, expected $\Upsilon(2\mathrm{S})$ production at low p_{T} is approximately twice higher than the measurement and $\Upsilon(3\mathrm{S})$ is roughly three times higher. Using the 'missing fraction' and the measured differential cross section of $\Upsilon(n\mathrm{S})$ states (for the full list of references see [141]), one can estimate that the measured cross-sections of $\Upsilon(2\mathrm{S})$ and $\Upsilon(3\mathrm{S})$ mesons are 'suppressed' by factors of 1.6 and 2.4 compared to the expectation from the production rates of $\Upsilon(1\mathrm{S})$. Despite the quantitative nature of this exploratory analysis, the leading systematic uncertainty is much smaller than the observed effect.

6 Results and discussion

6.1 Simultaneous assessment of the results

The mean number of charged particles with transverse momentum between 0.5 and 10 GeV measured in the pseudorapidity range $|\eta| < 2.5$ in events with reconstructed $\Upsilon(n\mathrm{S})$ mesons are shown in the left panel of Figure 56 as a function of Υ $p_{\mathrm{T}}^{\mu\mu}$. The upper

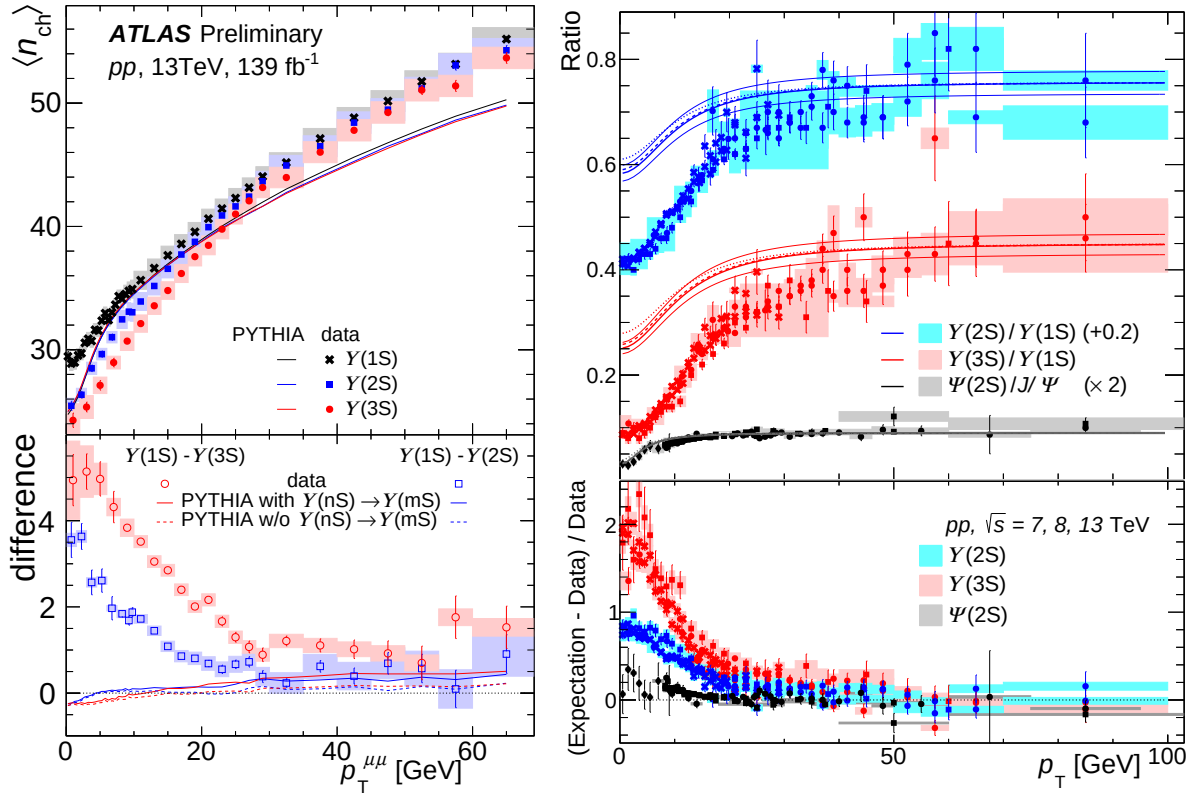

Figure 56: Left: The mean number of charged particles with $0.5 < p_{\mathrm{T}} < 10$ GeV and $|\eta| < 2.5$ in events with $\Upsilon(n\mathrm{S})$ mesons (top) and difference of this quantity between the excited and ground $\Upsilon(n\mathrm{S})$ state (bottom). Right: Measured $(q\bar{q})^{\star}/q\bar{q}$ ratios (top) and the difference of the expected value based on m_{T}-scaling to the measurement divided by the measurement (bottom).

panel shows the results for the three measured Υ states, and the lower panel shows the differences $\Upsilon(1\mathrm{S})$ less $\Upsilon(2\mathrm{S})$ and $\Upsilon(1\mathrm{S})$ less $\Upsilon(3\mathrm{S})$ states. The Figure shows significant differences in $\langle n_{\mathrm{ch}} \rangle$. Unlike the data, the Pythia8 prediction shows very similar particle multiplicity for all three Υ states. This conclusion is unchanged by changing the color reconnection scheme in the Pythia8 simulation. At the lowest measured $p_{\mathrm{T}}^{\mu\mu}$, the differ-

ence in $\langle n_{\rm ch}\rangle$ for $\Upsilon(1S)-\Upsilon(2S)$ is 3.6 ± 0.4 and for $\Upsilon(1S)-\Upsilon(3S)$ it is 4.9 ± 1.1, where the uncertainties correspond to systematic and statistical uncertainties added in quadrature. The $p_{\rm T}^{\mu\mu}$ dependencies of the differences between the excited and ground states are similar for both excited states. This measurement is qualitatively consistent with the finding of the CMS experiment [15], but ATLAS shows much higher magnitudes than are reported by the CMS, which observes about one particle between the states. This effect measured by ATLAS reaches $12\pm1\%$ for $\Upsilon(1S)-\Upsilon(2S)$ and $17\pm4\%$ for $\Upsilon(1S)-\Upsilon(3S)$. This cannot be explained by known effects like the feed-downs between $\Upsilon(n{\rm S})$ states, which are compared in the lower-left panel of Figure 56 to the data using MC simulations based on Pythia8. The discussion of Figure 49 leads to the conclusion that the effects are related to the UE and not to the jet part of the collision. The CMS experiment arrived to the same conclusions based on the analysis of the event sphericity.

Much novel insight into the physics behind the observed phenomenon can be obtained from the analysis of the expected vs. measured $\Upsilon(n{\rm S})$ yields that is done implying the $m_{\rm T}$-scaling analysis. The results of this study are shown in the right panel of Figure 56 to enable a side-by-side comparison of the results.

The upper panel of the right panel shows particle ratios are known to only weakly depend on rapidity and $\sqrt{s}$. Therefore all available LHC data is shown in the same plot. The data are compared to expectations based on $m_{\rm T}$-scaling, which are shown with solid lines for the three collision energies. The $m_{\rm T}$ expectations are normalized to data at $p_{\rm T} >$ 50 GeV, and the uncertainties resulting from the normalization are shown with thin lines. Employing the $m_{\rm T}$-scaling to compare particle spectra distributions is a commonly-used technique performed in many studies (e.g.:Ref. [105]). Such studies typically demonstrate a very good agreement between the $m_{\rm T}$-scaling and measured particle ratios.

Figure 56, on the contrary, demonstrate clear differences between the expectation and the data for $(b\bar{b})^\star$ species and significantly better consistency for $(c\bar{c})^\star$. To quantify the discrepancies, the lower panel shows the particles' 'missing fraction' constructed from the ratios. It is the measured value subtracted from the expected value and normalized to the measured, this normalization cancels the ground state production rate, and thus the quantity represents the 'missing' excited state production equal to $(q\bar{q})^\star_{\rm expected}/(q\bar{q})^\star_{\rm measured}-1$. The normalization uncertainty is added to the systematic uncertainty drawn at each point. The curves show that assuming the $m_{\rm T}$-scaling scenario and $\Upsilon(1S)$-meson cross-section, at

low p_{T}, the $\Upsilon(2S)$ production expectation is approximately twice as high as the measurement and $\Upsilon(3S)$ is roughly three times higher. Estimation for $\Psi(2S)$ at low p_{T} is above zero, suggesting that the $(c\bar{c})^{\star}$ may also be affected, although to a much lesser extent than the Υ case. With the existing data and understanding of the prompt fraction in J/Ψ, a conclusion about $(c\bar{c})^{\star}$ cannot be drawn with a large degree of certainty. At higher p_{T}, $\Upsilon(2S)$ and $\Upsilon(3S)$ points are significantly above zero to at least 30 GeV.

There is a striking similarity between results presented in both lower panels of Figure 56. Curves shown in the left panel are the difference in the $\langle n_{\mathrm{ch}} \rangle$ between $\Upsilon(n\mathrm{S})$ states, and curves in the right panel showing the missing fraction of events between these states have the same shape and the same ordering. This level of similarity excludes the possibility of that being a random coincidence. At the same time, there is a very clear scenario that can explain the two effects simultaneously. *There exists an interaction between the particles produced in a hard scattering of two energetic partons with the UE of the pp collision that is coming from different parton-parton interactions.* Excited $\Upsilon(n\mathrm{S})$ states would be destroyed in such interactions more intensely when the UE is larger, and therefore, the fraction of such events would have the same profile as the excess of $\langle n_{\mathrm{ch}} \rangle$ in the events where they survive. This is the first evidence that such a phenomenon exists in pp collisions.

The m_{T}-scaling allows us to estimate the magnitude of the effect, i.e., how many $\Upsilon(n\mathrm{S})$ would be produced is pp collisions if such interactions would not exist. For that, the missing fraction has to be multiplied by the measured cross-sections and added to it. This exercise shows that for the $\Upsilon(2S)$, the cross-section has to be 1.6 times larger for $\Upsilon(2S)$ and 2.4 times larger for $\Upsilon(3S)$ mesons. This estimate, of course, fully relies on the assumption of the m_{T}-scaling, and within this assumption, the accuracy of the estimates is rather high and consists of approximately 5% that is coming from the limited statistics of high-p_{T} normalization of the calculated ratios to the measured ones. It also has a contribution from the uncertainties of the T and n parameters, which are included in that number.

Studies described in this report suggest that this interaction significantly changes the production rates of $(b\bar{b})^{\star}$ states. It would be natural to ask a question what other particles can be affected? The m_{T}-scaling analysis is also applied for $\Psi(2S)$, for which ratio to J/Ψ is shown on the right panel of Figure 56. Clearly, the same mechanism does not affect

the production of $\Psi(2S)$ to the same extent as $(b\bar{b})^{\star}$. However, the effect cannot be fully excluded either. The most direct way to answer the question about $\Psi(2S)$ is to measure its correlation to the $\langle n_{\mathrm{ch}} \rangle$ UE.

6.2 Connection to HI physics

The effect observed in these studies has a clear ordering such that it is larger for $\Upsilon(3S)$ than for $\Upsilon(2S)$. This suggests that the effect is related to the binding of the quarks in the particles or to the size of the particle wave function. If this is the driving parameter, it would be logical to assume that $\chi_b(n\mathrm{P})$ and possibly $\chi_c(n\mathrm{P})$ states can be affected as well. Unfortunately, reconstructing these particles is challenging experimentally, but they can provide another insight into the physics of the observed phenomenon.

Both studies presented in the report use $\Upsilon(1S)$ as a baseline, and therefore they are insensitive to possible modification of $\Upsilon(1S)$ rates. Indirectly, an insight on whether $\Upsilon(1S)$ is also modified in pp may be coming from the measurements of R_{AA} performed in Pb+Pb. Since the effects for $\Upsilon(1S)$ are expected to be smaller than for higher $\Upsilon(n\mathrm{S})$, one can benefit from the larger size of the system. Figure 57 shows the R_{AA} as a function of

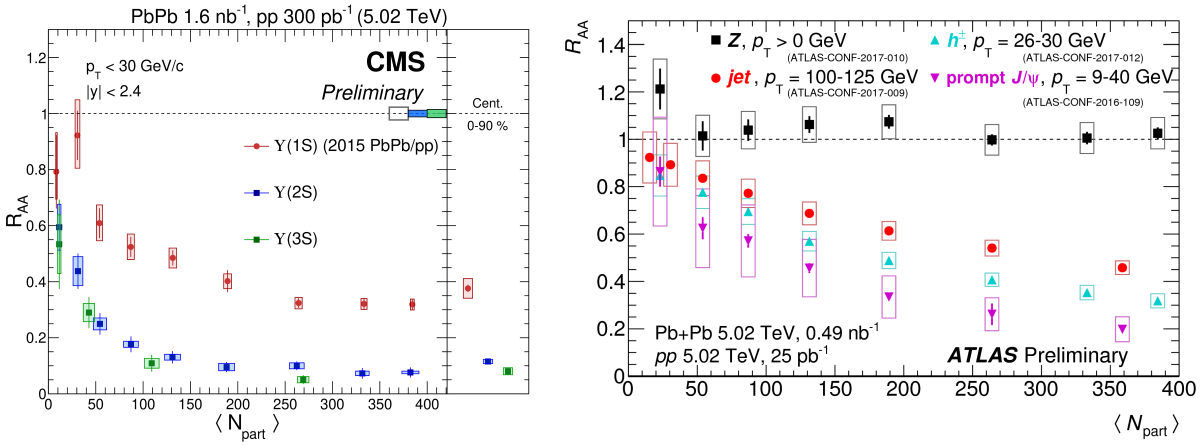

Figure 57: Left: Nuclear modification factors for different Υ states as a function of $\langle N_{\mathrm{part}} \rangle$ [16]. Right: Compilation of results for the nuclear modification factor R_{AA} vs number of participating nucleons N_{part} in different channels from the Run 2 Pb+Pb and pp data [56].

the mean number of participants $\langle N_{\mathrm{part}} \rangle$ for different Υ states (left) and for other particles (right). The level of $\Upsilon(1S)$ suppression is comparable to magnitudes registered for other hadrons, but $\Upsilon(2S)$ and $\Upsilon(3S)$ exhibit much stronger suppression. This does not answer

the question about Υ(1S) suppression in pp, but it suggests that it should be comparable to the effect for other hadrons. At the same time, Figure 57 suggests that Υ(1S) has a higher probability of getting out from the fireball from various points within the size of the system. With increasing the system size (N_{part}), it warrants a downward trend with decreasing centrality (increasing fireball radius). Υ(2S), on the other hand, shows much flatter behavior above $N_{\text{part}} = 100$, which suggests that they can get out of the system only from a relatively limited distance below the surface, and for Υ(3S), this layer should be even thinner than for Υ(2S). It is directly related to the effects described in the report.

Unfortunately, there is no theoretical guidance for the effect, and the only insight into the data can be inferred from the PYTHIA8 event generator. First of all, in the PYTHIA8 model, quarkonia are produced through dedicated processes that are distinct from perturbative quantum chromodynamics (pQCD) hard particle production. This means that PYTHIA8 does not produce quarkonia inside of jets. Therefore it contains no near-side jet, and for that reason, PYTHIA8 does not describe the near-side peak well. Secondly, PYTHIA8 does not have the effect of interactions with the UE, and therefore it shall be normalized to the data as it was earlier explained. A disadvantage of that can be seen, for example, in Figure 49 where PYTHIA8 curves more or less describe the feed-downs of $\Upsilon(n\text{S}) \rightarrow \Upsilon(1\text{S})$ for Υ(3S) curve shown in the lower-right panel, but not so well for Υ(2S) shown in the middle-right panel. This may be misleading. PYTHIA8 curves shown in that panel correspond to open circles, which do have an elevation around $\Delta\phi = 0$, although smaller than suggested by PYTHIA8. However, the curves that are normalized at all $\Delta\phi$ appear even higher. But in the region that is the most interesting for this analysis, i.e., at $\Delta\phi = \pm\pi$ Υ(2S) points are clearly above zero, and that has nothing to do with the feed-downs. This has an interesting consequence on the results shown in the lower-left panel of Figure 56. It can be seen that above 30 GeV PYTHIA8 curve that includes the feed-downs (solid line) reasonably describes at least Υ(2S) data, but it can be not so. The discussion given above may suggest that this is just a coincidence and the excess above zero seen for both $\Upsilon(n\text{S}) - \Upsilon(1\text{S})$ curves need to be explained based on other considerations.

6.3 Connection to theoretical calculations of Upsilon cross-sections

In Ref. [97], one can find the theoretical study of $\Upsilon(n\mathrm{S})$ and χ_b production at next-to-leading order in α_s in nonrelativistic QCD (NRQCD) using the LHC data. To fit the model, authors are using differential cross sections of $\Upsilon(n\mathrm{S})$ measured by ATLAS [5] and CMS [6], and fractions of $\Upsilon(n\mathrm{S})$ production originating from $\chi_b(nP)$ feed down contributions measured by LHCb [139]. Comparisons between the model and data are shown in Figure 58. One can see the discrepancy of the model in $p_{\mathrm{T}} < 20$ GeV region for all three

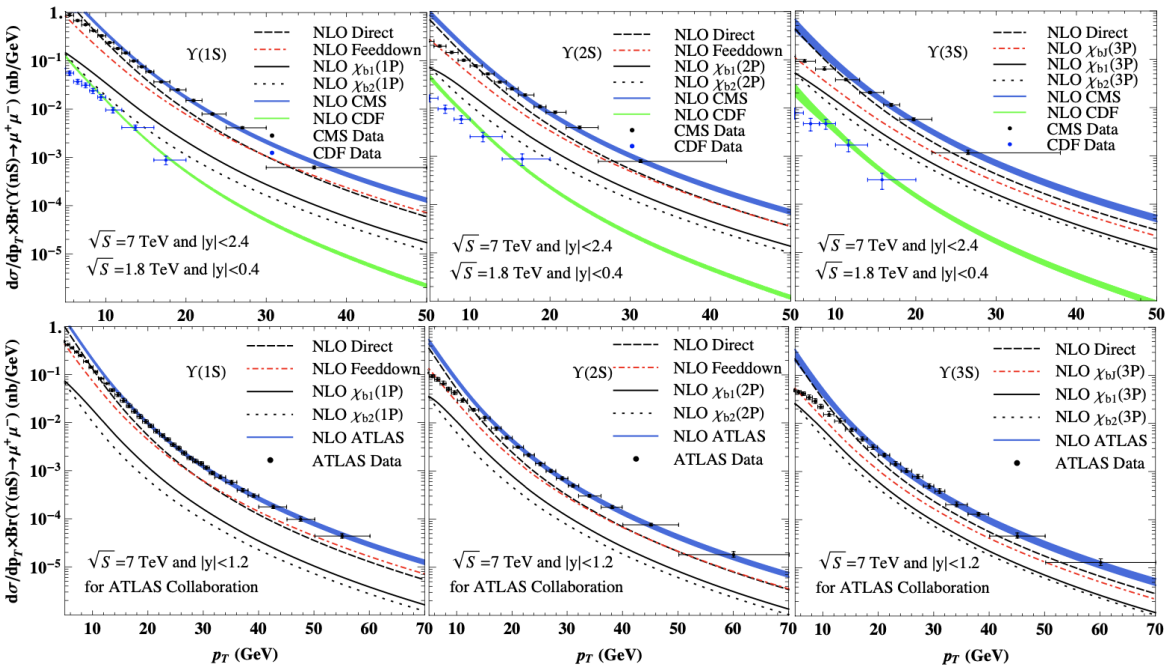

Figure 58: Differential p_{T} cross sections for the experimental data of ATLAS, CMS and CDF. From left to right: $\Upsilon(1\mathrm{S})$, $\Upsilon(2\mathrm{S})$, $\Upsilon(3\mathrm{S})$. The contributions from direct production are denoted by dashed lines, while those from feed down by dashed-dotted lines. The $\chi_{b_1}(nP) - \Upsilon(n\mathrm{S})$ and $\chi_{b_2}(nP) - \Upsilon(n\mathrm{S})$ feed down contributions are denoted by the solid and dotted lines respectively [97].

$\Upsilon(n\mathrm{S})$ states. These differences are larger for higher Υ states; however, the difference between the data and the model prediction is significant even for $\Upsilon(1\mathrm{S})$. We cannot measure suppression of $\Upsilon(1\mathrm{S})$ state, but from these plots, one can assume that the ground Υ state can also be affected.

6.4 Connection to the Comover Interaction Model

Within the framework of the comover interaction model (CIM) [143–147], quarkonia are broken by collisions with comovers, i.e., final state particles with similar rapidities. In this model, recombination effects are neglected. The basic ingredient of this model is the profile function of the proton, taken as a Fermi function. The comover density is proportional to the number of binary parton-parton collisions per unit of transverse area and rapidity at a given impact parameter, which in turn is proportional to the overlap between protons [148]. The quarkonium abundance is driven by its interaction cross-section with comovers. One can recall two features of the comover approach:

- Larger particles are more affected by dissociation due to larger interaction cross sections. As a consequence, excited states are more suppressed than ground states.
- The suppression increases with comover densities, which is proportional to particle multiplicities.

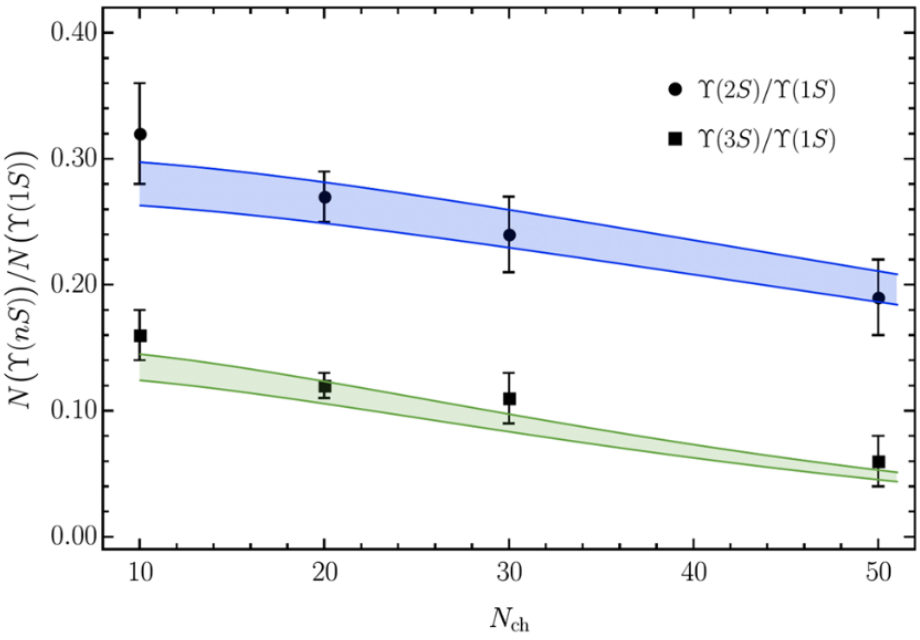

Figure 59: Relative yields of excited-to-ground state Υ as a function of multiplicity for pp collisions at 2.76 TeV [14]. The bands follow the uncertainties of the six cross sections that contribute via the feed down, and uncertainties of phenomenological parameters. [149]

Figure 59 shows the applicability of CIM to describing the yields of Υ mesons. Points are the relative Υ yields, measured by CMS at 2.76 TeV, as a function of the number of

charged tracks within $p_{\mathrm{T}} > 400$ MeV and $\eta < 2.4$ [14]. From Figure 59, one may confirm the validity of the model; however, to answer the question of whether the CIM is able to describe our results or not, one needs to measure 2PC between Υ meson and charged particle.

6.5 Connection to other species

It is interesting to note that, in spite of the strangeness enhancement, discussed in Section 2.4, the particle ratio of K^{*0}/K, measured by ALICE [150, 151] and STAR [152] collaborations, also go down with n_{ch} for both A+A and pp collision systems (see, for example, Figure 60). Possibly, it is a manifestation of the same effect.

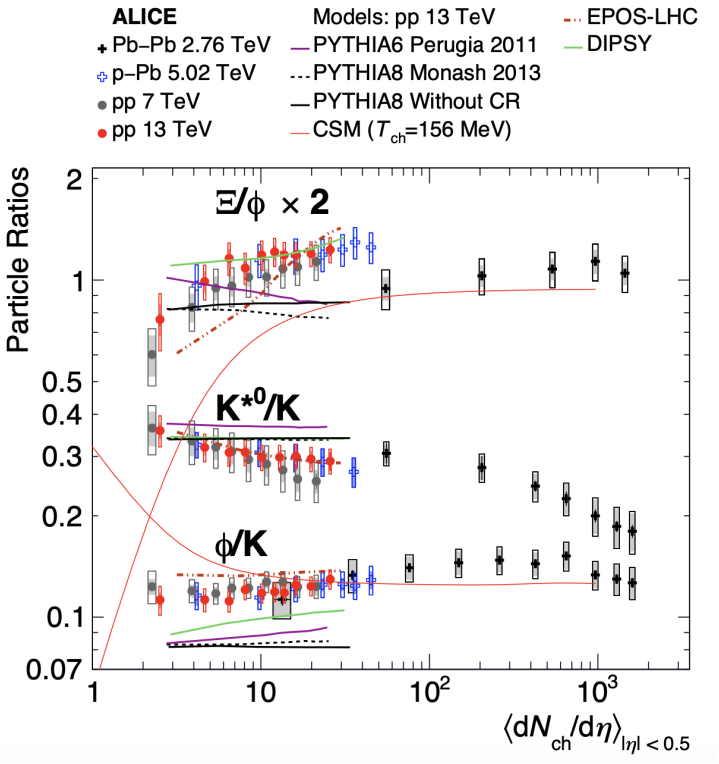

Figure 60: Ratios of p_{T}-integrated yields of Ξ/ϕ, K^{*0}/K, and ϕ/K as functions of $\langle dN_{ch}/d\eta \rangle$ for pp, $p+\mathrm{Pb}$ and $\mathrm{Pb}+\mathrm{Pb}$ collision systems [150].

References

[1] ATLAS Collaboration. Underlying event characteristics and their dependence on jet size of charged-particle jet events in pp collisions at $\sqrt{s} = 7$ TeV with the ATLAS detector. Phys. Rev. D, 86:072004, 2012.

[2] ATLAS Collaboration. Measurement of distributions sensitive to the underlying event in inclusive Z-boson production in pp collisions at $\sqrt{s} = 7$ TeV with the ATLAS detector. Eur. Phys. J. C, 74(12):3195, 2014.

[3] ATLAS Collaboration. Measurement of charged-particle distributions sensitive to the underlying event in $\sqrt{s} = 13$ TeV proton-proton collisions with the ATLAS detector at the LHC. JHEP, 03:157, 2017.

[4] ATLAS Collaboration. Measurement of the $\Upsilon(1S)$ production cross-section in pp collisions at $\sqrt{s} = 7$ TeV in ATLAS. Phys. Lett. B, 705:9–27, 2011.

[5] Georges Aad et al. Measurement of Υ production in 7 TeV pp collisions at ATLAS. Phys. Rev. D, 87(5):052004, 2013.

[6] CMS Collaboration. Measurement of the $\Upsilon(1S)$, $\Upsilon(2S)$, and $\Upsilon(3S)$ Cross Sections in pp Collisions at $\sqrt{s} = 7$ TeV. Phys. Lett. B, 727:101–125, 2013.

[7] Vardan Khachatryan et al. Measurements of the $\Upsilon(1S)$, $\Upsilon(2S)$, and $\Upsilon(3S)$ differential cross sections in pp collisions at $\sqrt{s} = 7$ TeV. Phys. Lett. B, 749:14–34, 2015.

[8] CMS Collaboration. Measurement of quarkonium production cross sections in pp collisions at $\sqrt{s} = 13$ TeV. Phys. Lett. B, 780:251–272, 2018.

[9] LHCb Collaboration. Production of J/psi and Upsilon mesons in pp collisions at sqrt(s) = 8 TeV. JHEP, 06:064, 2013.

[10] Roel Aaij et al. Forward production of Υ mesons in pp collisions at $\sqrt{s} = 7$ and 8 TeV. JHEP, 11:103, 2015.

[11] R. Aaij et al. Measurement of Υ production in pp collisions at $\sqrt{s} = 13$ TeV. JHEP, 07:134, 2018. [Erratum: JHEP 05, 076 (2019)].

[12] Jean-Philippe Lansberg. New Observables in Inclusive Production of Quarkonia. Phys. Rept., 889:1–106, 2020.

[13] A. Andronic et al. Heavy-flavour and quarkonium production in the LHC era: from proton–proton to heavy-ion collisions. Eur. Phys. J. C, 76(3):107, 2016.

[14] Serguei Chatrchyan et al. Event Activity Dependence of Y(nS) Production in $\sqrt{s_{\rm NN}} = 5.02$ TeV p+Pb and $\sqrt{s} = 2.76$ TeV pp Collisions. JHEP, 04:103, 2014.

[15] Albert M Sirunyan et al. Investigation into the event-activity dependence of Υ(nS) relative production in proton-proton collisions at $\sqrt{s} = 7$ TeV. JHEP, 11:001, 2020.

[16] CMS Collaboration. Observation of the Υ(3S) meson and sequential suppression of Υ states in PbPb collisions at $\sqrt{\rm s_{NN}} = 5.02$ TeV. Technical report, CERN, Geneva, 2022.

[17] Torbjorn Sjostrand, Stephen Mrenna, and Peter Z. Skands. A brief introduction to pythia 8.1. Comput. Phys. Commun., 178:852–867, 2008.

[18] E. L. Bratkovskaya, W. Cassing, and U. Mosel. Meson $m_{\rm T}$- scaling in heavy ion collisions at SIS energies. Phys. Lett. B, 424:244–252, 1998.

[19] B. I. Abelev et al. Strange particle production in pp collisions at $\sqrt{s} = 200$-GeV. Phys. Rev. C, 75:064901, 2007.

[20] Lucas Altenkämper, Friederike Bock, Constantin Loizides, and Nicolas Schmidt. Applicability of transverse mass scaling in hadronic collisions at energies available at the CERN Large Hadron Collider. Phys. Rev. C, 96(6):064907, 2017.

[21] S. L. Glashow, J. Iliopoulos, and L. Maiani. Weak interactions with lepton-hadron symmetry. Phys. Rev. D, 2:1285–1292, Oct 1970.

[22] Steven Weinberg. A model of leptons. Phys. Rev. Lett., 19:1264–1266, Nov 1967.

[23] M. Tanabashi and et. al. Review of particle physics. Phys. Rev. D, 98:030001, Aug 2018.

[24] Abdus Salam. Weak and Electromagnetic Interactions. Conf. Proc. C, 680519:367–377, 1968.

[25] F. Englert and R. Brout. Broken symmetry and the mass of gauge vector mesons. Phys. Rev. Lett., 13:321–323, Aug 1964.

[26] Georges Aad et al. Observation of a new particle in the search for the Standard Model Higgs boson with the ATLAS detector at the LHC. Phys. Lett. B, 716:1–29, 2012.

[27] Serguei Chatrchyan et al. Observation of a New Boson at a Mass of 125 GeV with the CMS Experiment at the LHC. Phys. Lett. B, 716:30–61, 2012.

[28] Murray Gell-Mann. Symmetries of baryons and mesons. Phys. Rev., 125:1067–1084, Feb 1962.

[29] O. W. Greenberg. Spin and unitary-spin independence in a paraquark model of baryons and mesons. Phys. Rev. Lett., 13:598–602, Nov 1964.

[30] R. P. Feynman. THE BEHAVIOR OF HADRON COLLISIONS AT EXTREME ENERGIES. pages 497–518, 1989.

[31] F. Halzen and Alan D. Martin. QUARKS AND LEPTONS: AN INTRODUCTORY COURSE IN 1984.

[32] David J. Gross and Frank Wilczek. Asymptotically free gauge theories. i. Phys. Rev. D, 8:3633–3652, Nov 1973.

[33] H. David Politzer. Asymptotic Freedom: An Approach to Strong Interactions. Phys. Rept., 14:129–180, 1974.

[34] R. Hagedorn. Statistical thermodynamics of strong interactions at high-energies. Nuovo Cim. Suppl., 3:147–186, 1965.

[35] Edward V. Shuryak. THE QCD VACUUM AND QUARK - GLUON PLASMA. Z. Phys. C, 38:141–145, 1988.

[36] P. Rosnet. Quark-Gluon Plasma: from accelerator experiments to early Universe. In 11th Rencontres du Vietnam: Cosmology: 50 years after CMB discovery, 10 2015.

[37] Z. Fodor and S. D. Katz. Critical point of QCD at finite T and mu, lattice results for physical quark masses. JHEP, 04:050, 2004.

[38] Jaroslav Adam et al. Direct photon production in Pb-Pb collisions at $\sqrt{s_{NN}} = 2.76$ TeV. Phys. Lett. B, 754:235–248, 2016.

[39] Szabolcs Borsanyi, Gergely Endrodi, Zoltan Fodor, Antal Jakovac, Sandor D. Katz, Stefan Krieg, Claudia Ratti, and Kalman K. Szabo. The QCD equation of state with dynamical quarks. JHEP, 11:077, 2010.

[40] C. Y. Wong. Introduction to high-energy heavy ion collisions. 1995.

[41] Matthew Allan Charles Lamont. Neutral Strange Particle Production in Ultra-Relativistic Heavy PhD thesis, Birmingham U., 2002.

[42] Roger D. Woods and David S. Saxon. Diffuse Surface Optical Model for Nucleon-Nuclei Scattering. Phys. Rev., 95:577–578, 1954.

[43] CMS Collaboration. Observation of Long-Range Near-Side Angular Correlations in Proton-Proton Collisions at the LHC. JHEP, 09:091, 2010.

[44] ATLAS Collaboration. Two-particle azimuthal correlations in photonuclear ultraperipheral Pb + Pb collisions at 5.02 TeV with ATLAS. Phys. Rev. C, 104(1):014903, 2021.

[45] James L. Nagle and William A. Zajc. Small System Collectivity in Relativistic Hadronic and Nuclear Collisions. Ann. Rev. Nucl. Part. Sci., 68:211–235, 2018.

[46] Constantin Loizides. Experimental overview on small collision systems at the LHC. Nucl. Phys. A, 956:200–207, 2016.

[47] PHENIX. Creation of quark–gluon plasma droplets with three distinct geometries. Nature Phys., 15(3):214–220, 2019.

[48] CMS Collaboration. Evidence for collectivity in pp collisions at the LHC. Phys. Lett. B, 765:193–220, 2017.

[49] Chun Shen. Studying qgp with flow: A theory overview. Nuclear Physics A, 1005:121788, 2021. The 28th International Conference on Ultra-relativistic Nucleus-Nucleus Collisions: Quark Matter 2019.

[50] Jaroslav Adam et al. Enhanced production of multi-strange hadrons in high-multiplicity proton-proton collisions. Nature Phys., 13:535–539, 2017.

[51] D.S.D. Albuquerque. Hadronic resonances, strange and multi-strange particle production in xe-xe and pb-pb collisions with alice at the lhc. Nuclear Physics A, 982:823–826, 2019. The 27th International Conference on Ultrarelativistic Nucleus-Nucleus Collisions: Quark Matter 2018.

[52] ATLAS Collaboration. Charged hadron R_{AA} in p + Pb, Pb + Pb and Xe+Xe at $\sqrt{s_{\mathrm{NN}}} = 5$ TeV with the ATLAS detector. 2021.

[53] Georges Aad et al. Centrality and rapidity dependence of inclusive jet production in $\sqrt{s_{\mathrm{NN}}} = 5.02$ TeV proton-lead collisions with the ATLAS detector. Phys. Lett. B, 748:392–413, 2015.

[54] Michelangelo L. Mangano and Benjamin Nachman. Observables for possible QGP signatures in central pp collisions. Eur. Phys. J. C, 78(4):343, 2018.

[55] Morad Aaboud et al. Measurement of photon–jet transverse momentum correlations in 5.02 TeV Pb + Pb and *pp* collisions with ATLAS. Phys. Lett. B, 789:167–190, 2019.

[56] Georges Aad et al. HI summary plots. 2018.

[57] Serguei Chatrchyan et al. Jet momentum dependence of jet quenching in PbPb collisions at $\sqrt{s_{NN}} = 2.76$ TeV. Phys. Lett. B, 712:176–197, 2012.

[58] ATLAS Collaboration. Measurement of photon-jet transverse momentum correlations in 5.02 TeV Pb+Pb and *pp* collisions with ATLAS. Phys. Lett. B, 789:167, 2019.

[59] Harald Fritzsch. Producing heavy quark flavors in hadronic collisions—' a test of quantum chromodynamics. Physics Letters B, 67(2):217–221, 1977.

[60] R. Baier and R. Ruckl. Hadronic Collisions: A Quarkonium Factory. Z. Phys. C, 19:251, 1983.

[61] Geoffrey T. Bodwin, Eric Braaten, and G. Peter Lepage. Erratum: Rigorous qcd analysis of inclusive annihilation and production of heavy quarkonium [phys. rev. d 51, 1125 (1995)]. Phys. Rev. D, 55:5853–5854, May 1997.

[62] Jan Cepila, Jan Nemchik, Michal Krelina, and Roman Pasechnik. Theoretical uncertainties in exclusive electroproduction of S-wave heavy quarkonia. Eur. Phys. J. C, 79(6):495, 2019.

[63] T. Matsui and H. Satz. J/ψ Suppression by Quark-Gluon Plasma Formation. Phys. Lett. B, 178:416–422, 1986.

[64] D. Besson and T. Skwarnicki. Υ spectroscopy. Ann. Rev. Nucl. Part. Sci., 43:333–378, 1993.

[65] Jean-Marc Richard. An introduction to the quark model. In Ferrara International School Niccolò Cabeo 2012: Hadronic spectroscopy, 5 2012.

[66] LHC Machine. JINST, 3:S08001, 2008.

[67] Esma Mobs. The CERN accelerator complex. Complexe des accélérateurs du CERN. 2016. General Photo.

[68] G. Aad et al. The ATLAS Experiment at the CERN Large Hadron Collider. JINST, 3:S08003, 2008.

[69] S. Chatrchyan et al. The CMS Experiment at the CERN LHC. JINST, 3:S08004, 2008.

[70] A. Augusto Alves, Jr. et al. The LHCb Detector at the LHC. JINST, 3:S08005, 2008.

[71] K. Aamodt et al. The ALICE experiment at the CERN LHC. JINST, 3:S08002, 2008.

[72] ATLAS Collaboration. The ATLAS Experiment at the CERN Large Hadron Collider. JINST, 3:S08003, 2008.

[73] ATLAS Collaboration. ATLAS Insertable B-Layer Technical Design Report. ATLAS-TDR-19, 2010.

[74] ATLAS Collaboration. ATLAS Insertable B-Layer Technical Design Report Addendum. ATLAS-TDR-19-ADD-1, 2012.

[75] B. Abbott et al. Production and integration of the ATLAS Insertable B-Layer. JINST, 13(05):T05008, 2018.

[76] ATLAS Collaboration. The ATLAS Experiment at the CERN Large Hadron Collider. JINST, 3:S08003, 2008.

[77] Christian W. Fabjan and Fabiola Gianotti. Calorimetry for particle physics. Rev. Mod. Phys., 75:1243–1286, Oct 2003.

[78] P. Puzo. Atlas calorimetry. Nuclear Instruments and Methods in Physics Research Section A: Accelerators, Spectrometers, Detectors and Associated Equipment, 494(1):340 – 345, 2002.

[79] Morad Aaboud et al. Measurement of long-range two-particle azimuthal correlations in Z-boson tagged pp collisions at $\sqrt{s} = 8$ and 13 TeV. Eur. Phys. J. C, 80(1):64, 2020.

[80] A Krasznahorkay. Tools for Trigger Aware Analyses in Atlas. Technical report, CERN, Geneva, Nov 2010.

[81] ATLAS Collaboration. Muon reconstruction performance of the ATLAS detector in proton–proton collision data at $\sqrt{s} = 13$ TeV. Eur. Phys. J. C, 76(5):292, 2016.

[82] ATLAS Collaboration. Performance of the ATLAS Track Reconstruction Algorithms in Dense Environments in LHC Run 2. Eur. Phys. J. C, 77(10):673, 2017.

[83] Tracking CP Working Group. Final Tracking CP Recommendations for Run 2. Technical report.

[84] Zvi Hirsh Citron, Brian Cole, Alexander Milov, and Soumya Mohapatra. Measurement of long-range azimuthal correlations in Z-boson tagged pp collisions at $\sqrt{s} = 8$ and 13 TeV. Technical report, CERN, Geneva, Dec 2017.

[85] Morad Aaboud et al. Luminosity determination in pp collisions at $\sqrt{s} = 8$ TeV using the ATLAS detector at the LHC. Eur. Phys. J. C, 76(12):653, 2016.

[86] ATLAS Collaboration. Performance of the ATLAS Trigger System in 2015. Eur. Phys. J. C, 77(5):317, 2017.

[87] ATLAS Collaboration. Performance of the ATLAS muon triggers in Run 2. JINST, 15(09):P09015, 2020.

[88] Charged-hadron production in pp, p+Pb, Pb+Pb, and Xe+Xe collisions at $\sqrt{s_{\mathrm{NN}}} =$ 5 TeV with the ATLAS detector at the LHC. 11 2022.

[89] ATLAS Collaboration. Charged-particle distributions in $\sqrt{s} = 13$ tev pp interactions measured with the atlas detector at the lhc. Phys. Lett. B, 758:67–88, 2016.

[90] Ewa Stanecka. ATLAS Inner Tracker Performance at the Beginning of the LHC Run 2. Technical report, CERN, Geneva, 2016.

[91] ATLAS Collaboration. Z boson production in Pb + Pb collisions at $\sqrt{s_{\mathrm{NN}}} = 5.02$ TeV measured by the ATLAS experiment. Phys. Lett. B, 802:135262, 2020.

[92] ATLAS Collaboration. Measurement of quarkonium production in proton-lead and proton-proton collisions at 5.02 TeV with the ATLAS detector. Eur. Phys. J. C, 78(3):171, 2018.

[93] Particle Data Group. Review of Particle Physics. PTEP, 2020(8):083C01, 2020.

[94] ATLAS Collaboration. Probing lepton flavour violation via neutrinoless $\tau \longrightarrow 3\mu$ decays with the ATLAS detector. Eur. Phys. J. C, 76(5):232, 2016.

[95] https://indico.cern.ch/event/78640/contributions/2095054/attachments/1058988/1510078/AafkeKraan.pdf.

[96] CMS Collaboration. Fragmentation of jets containing a prompt J/ψ meson in PbPb and pp collisions at sNN=5.02TeV. Phys. Lett. B, 825:136842, 2022.

[97] Hao Han, Yan-Qing Ma, Ce Meng, Hua-Sheng Shao, Yu-Jie Zhang, and Kuang-Ta Chao. $\Upsilon(nS)$ and $\chi_b(nP)$ production at hadron colliders in nonrelativistic QCD. Phys. Rev. D, 94(1):014028, 2016.

[98] Rolf Hagedorn. Statistical thermodynamics of strong interactions at high energies. Nuovo Cimento, Suppl., 3:147–186, 1965.

[99] B. Alper et al. Large angle inclusive production of charged pions at the cern isr with transverse momenta less than 1.0 gev/c. Phys. Lett. B, 47:75–79, 1973.

[100] B. Alper, H. Boggild, P. Booth, F. Bulos, L.J. Carroll, G. Von Dardel, G. Damgaard, B. Duff, F. Heymann, J.N. Jackson, G. Jarlskog, L. Jonsson, A. Klovning, L. Leistam, E. Lillethun, G. Lynch, S. Olgaard-Nielsen, M. Prentice, D. Quarrie, and J.M. Weiss. Large-angle inclusive production of charged pions at the cern isr with transverse moment a less than 1.0 gev/c. Physics Letters B, 47(1):75–79, 1973.

[101] B. Abelev et al. Neutral pion and η meson production in proton-proton collisions at $\sqrt{s} = 0.9$ TeV and $\sqrt{s} = 7$ TeV. Phys. Lett. B, 717:162–172, 2012.

[102] Jaroslav Adam et al. Multiplicity dependence of charged pion, kaon, and (anti)proton production at large transverse momentum in p-Pb collisions at $\sqrt{s_{\rm NN}} =$ 5.02 TeV. Phys. Lett. B, 760:720–735, 2016.

[103] Jaroslav Adam et al. Measurement of pion, kaon and proton production in proton-proton collisions at $\sqrt{s} = 7$ TeV. Eur. Phys. J. C, 75(5):226, 2015.

[104] Shreyasi Acharya et al. Production of ω mesons in pp collisions at $\sqrt{s} = 7\,$TeV. Eur. Phys. J. C, 80(12):1130, 2020.

[105] Shreyasi Acharya et al. Production of light-flavor hadrons in pp collisions at $\sqrt{s} = 7$ and $\sqrt{s} = 13\,$TeV. Eur. Phys. J. C, 81(3):256, 2021.

[106] Shreyasi Acharya et al. $\mathrm{K}^*(892)^0$ and $\phi(1020)$ production at midrapidity in pp collisions at $\sqrt{s} = 8$ TeV. Phys. Rev. C, 102(2):024912, 2020.

[107] Shreyasi Acharya et al. Measurement of D-meson production at mid-rapidity in pp collisions at $\sqrt{s} = 7$ TeV. Eur. Phys. J. C, 77(8):550, 2017.

[108] Betty Bezverkhny Abelev et al. Measurement of quarkonium production at forward rapidity in pp collisions at $\sqrt{s} = 7$ TeV. Eur. Phys. J. C, 74(8):2974, 2014.

[109] Shreyasi Acharya et al. π^0 and η meson production in proton-proton collisions at $\sqrt{s} = 8$ TeV. Eur. Phys. J. C, 78(3):263, 2018.

[110] Jaroslav Adam et al. Inclusive quarkonium production at forward rapidity in pp collisions at $\sqrt{s} = 8$ TeV. Eur. Phys. J. C, 76(4):184, 2016.

[111] Shreyasi Acharya et al. Inclusive J/Ψ production at midrapidity in pp collisions at $\sqrt{s} = 13$ TeV. Eur. Phys. J. C, 81(12):1121, 2021.

[112] Shreyasi Acharya et al. Energy dependence of forward-rapidity J/Ψ and $\Psi(2S)$ production in pp collisions at the LHC. Eur. Phys. J. C, 77(6):392, 2017.

[113] Shreyasi Acharya et al. Energy dependence of ϕ meson production at forward rapidity in pp collisions at the LHC. Eur. Phys. J. C, 81(8):772, 2021.

[114] Georges Aad et al. Measurement of $D^{*\pm}$, $D^{\pm}$ and $D_s^{\pm}$ meson production cross sections in pp collisions at $\sqrt{s} = 7$ TeV with the ATLAS detector. Nucl. Phys. B, 907:717–763, 2016.

[115] ATLAS Collaboration. Measurement of the differential cross-sections of inclusive, prompt and non-prompt J/ψ production in proton-proton collisions at $\sqrt{s} = 7$ TeV. Nucl. Phys. B, 850:387–444, 2011.

[116] Georges Aad et al. Measurement of χ_{c1} and χ_{c2} production with $\sqrt{s} = 7$ TeV pp collisions at ATLAS. JHEP, 07:154, 2014.

[117] ATLAS Collaboration. Measurement of the differential cross-sections of prompt and non-prompt production of J/ψ and $\psi(2S)$ in pp collisions at $\sqrt{s} = 7$ and 8 TeV with the ATLAS detector. Eur. Phys. J. C, 76(5):283, 2016.

[118] Georges Aad et al. Measurement of the differential cross-section of B^+ meson production in pp collisions at $\sqrt{s} = 7$ TeV at ATLAS. JHEP, 10:042, 2013.

[119] Georges Aad et al. K-short and Λ production in pp interactions at $\sqrt{s} = 0.9$ and 7 TeV measured with the ATLAS detector at the LHC. Phys. Rev. D, 85:012001, 2012.

[120] Morad Aaboud et al. Measurements of $\Psi(2S)$ and $X(3872) \to J/\psi\pi^+\pi^-$ production in pp collisions at $\sqrt{s} = 8$ TeV with the ATLAS detector. JHEP, 01:117, 2017.

[121] Vardan Khachatryan et al. Prompt and Non-Prompt J/Ψ Production in pp Collisions at $\sqrt{s} = 7$ TeV. Eur. Phys. J. C, 71:1575, 2011.

[122] Vardan Khachatryan et al. Measurement of J/Ψ and $\Psi(2S)$ Prompt Double-Differential Cross Sections in pp Collisions at $\sqrt{s} = 7$ TeV. Phys. Rev. Lett., 114(19):191802, 2015.

[123] Serguei Chatrchyan et al. Measurement of the B^0 production cross section in pp Collisions at $\sqrt{s} = 7$ TeV. Phys. Rev. Lett., 106:252001, 2011.

[124] Vardan Khachatryan et al. Measurement of the B^+ Production Cross Section in pp Collisions at $\sqrt{s} = 7$ TeV. Phys. Rev. Lett., 106:112001, 2011.

[125] Serguei Chatrchyan et al. Measurement of the Strange B Meson Production Cross Section with $J/\Psi\ \phi$ Decays in pp Collisions at $\sqrt{s} = 7$ TeV. Phys. Rev. D, 84:052008, 2011.

[126] Serguei Chatrchyan et al. J/Ψ and $\Psi(2S)$ production in pp collisions at $\sqrt{s} = 7$ TeV. JHEP, 02:011, 2012.

[127] Albert M Sirunyan et al. Measurement of charged pion, kaon, and proton production in proton-proton collisions at $\sqrt{s} = 13$ TeV. Phys. Rev. D, 96(11):112003, 2017.

[128] Vardan Khachatryan et al. Measurement of the total and differential inclusive B^+ hadron cross sections in pp collisions at $\sqrt{s} = 13$ TeV. Phys. Lett. B, 771:435–456, 2017.

[129] R Aaij et al. Prompt charm production in pp collisions at $\sqrt{s} = 7$ TeV. Nucl. Phys. B, 871:1–20, 2013.

[130] R. Aaij et al. Measurement of J/Ψ production in pp collisions at $\sqrt{s} = 7$ TeV. Eur. Phys. J. C, 71:1645, 2011.

[131] R Aaij et al. Measurement of $\Psi(2S)$ meson production in pp collisions at $\sqrt{s} = 7$ TeV. Eur. Phys. J. C, 72:2100, 2012. [Erratum: Eur.Phys.J.C 80, 49 (2020)].

[132] R Aaij et al. Measurement of B meson production cross-sections in proton-proton collisions at $\sqrt{s} = 7$ TeV. JHEP, 08:117, 2013.

[133] R. Aaij et al. Measurement of the inclusive ϕ cross-section in pp collisions at $\sqrt{s} = 7$ TeV. Phys. Lett. B, 703:267–273, 2011.

[134] Roel Aaij et al. Measurement of Ψ(2S) production cross-sections in proton-proton collisions at $\sqrt{s} = 7$ and 13 TeV. Eur. Phys. J. C, 80(3):185, 2020.

[135] Roel Aaij et al. Measurements of prompt charm production cross-sections in pp collisions at $\sqrt{s} = 13$ TeV. JHEP, 03:159, 2016. [Erratum: JHEP 09, 013 (2016), Erratum: JHEP 05, 074 (2017)].

[136] Roel Aaij et al. Measurement of the $\eta_c(1S)$ production cross-section in pp collisions at $\sqrt{s} = 13$ TeV. Eur. Phys. J. C, 80(3):191, 2020.

[137] Roel Aaij et al. Measurement of forward J/Ψ production cross-sections in pp collisions at $\sqrt{s} = 13$ TeV. JHEP, 10:172, 2015. [Erratum: JHEP 05, 063 (2017)].

[138] A. Adare et al. Measurement of neutral mesons in p+p collisions at $\sqrt{s} = 200$ GeV and scaling properties of hadron production. Phys. Rev. D, 83:052004, 2011.

[139] Roel Aaij et al. Study of χ_b meson production in pp collisions at $\sqrt{s} = 7$ and 8 TeV and observation of the decay $\chi_b(3P) \to \Upsilon(3S)\gamma$. Eur. Phys. J. C, 74(10):3092, 2014.

[140] Smbat Grigoryan. Using the Tsallis distribution for hadron spectra in pp collisions: Pions and quarkonia at $\sqrt{s} = 5$–13000 GeV. Phys. Rev. D, 95(5):056021, 2017.

[141] Iakov Aizenberg, Zvi Citron, and Alexander Milov. Can transverse mass scaling shed light on the event-activity dependence of Υ-meson production at the LHC? Phys. Rev. D, 107(1):014012, 2023.

[142] Torbjörn Sjöstrand, Stefan Ask, Jesper R. Christiansen, Richard Corke, Nishita Desai, Philip Ilten, Stephen Mrenna, Stefan Prestel, Christine O. Rasmussen, and Peter Z. Skands. An introduction to PYTHIA 8.2. Comput. Phys. Commun., 191:159–177, 2015.

[143] E. G. Ferreiro. Excited charmonium suppression in proton–nucleus collisions as a consequence of comovers. Phys. Lett. B, 749:98–103, 2015.

[144] Elena G. Ferreiro and Jean-Philippe Lansberg. Is bottomonium suppression in proton-nucleus and nucleus-nucleus collisions at LHC energies due to the same effects? JHEP, 10:094, 2018. [Erratum: JHEP 03, 063 (2019)].

[145] A. Capella, E. G. Ferreiro, and A. B. Kaidalov. Nonsaturation of the J / psi suppression at large transverse energy in the comovers approach. Phys. Rev. Lett., 85:2080–2083, 2000.

[146] A. Capella, L. Bravina, E. G. Ferreiro, A. B. Kaidalov, K. Tywoniuk, and E. Zabrodin. Charmonium dissociation and recombination at RHIC and LHC. Eur. Phys. J. C, 58:437–444, 2008.

[147] E. G. Ferreiro. Charmonium dissociation and recombination at LHC: Revisiting comovers. Phys. Lett. B, 731:57–63, 2014.

[148] N. Armesto, A. Capella, and E. G. Ferreiro. Charmonium suppression in lead-lead collisions: Is there a break in the J / psi cross-section? Phys. Rev. C, 59:395–404, 1999.

[149] Angelo Esposito, Elena G. Ferreiro, Alessandro Pilloni, Antonio D. Polosa, and Carlos A. Salgado. The nature of X(3872) from high-multiplicity pp collisions. Eur. Phys. J. C, 81(7):669, 2021.

[150] Shreyasi Acharya et al. Multiplicity dependence of K*(892)^0 and $\phi(1020)$ production in pp collisions at $\sqrt{s}$ =13 TeV. Phys. Lett. B, 807:135501, 2020.

[151] Shreyasi Acharya et al. Production of K*(892)^0 and $\phi(1020)$ in pp and Pb-Pb collisions at $\sqrt{s_{\rm NN}} = 5.02$ TeV. Phys. Rev. C, 106(3):034907, 2022.

[152] K^{*0} production in Au+Au collisions at $\sqrt{s_{\rm NN}} = 7.7$, 11.5, 14.5, 19.6, 27 and 39 GeV from RHIC beam energy scan. 10 2022.